3

Climate, the Hydrologic Cycle, Soils, and Vegetation: A Global Overview

3.1 BASIC ASPECTS OF GLOBAL CLIMATE

3.1.1 The Energy Budget of the Earth

The sun radiates energy approximately as a blackbody with a temperature of 6000 K (Figure 3-1, curve *a*); its radiation spectrum extends from the ultraviolet to the infrared, with a maximum in the visible range. (See Section D.1 for a review of the physics of radiation.) However, gases in the earth's atmosphere are strong absorbers of energy at specific wavelengths in this range, so that the radiation striking the earth's surface is depleted in portions of the spectrum (Figure 3-1, curve *b*). In particular, normal oxygen (O_2) and ozone (O_3) in the lower stratosphere shield terrestrial biota from much of the energy in the ultraviolet range, which is damaging to most forms of life. Water vapor also absorbs some of the sun's energy in the "near infrared" range. Thus virtually all the sun's energy arriving at the surface is at wavelengths less than 4 μm; this energy is referred to as **solar radiation** or **shortwave radiation.**

The sun's energy arrives at the outer edge of the atmosphere at an average rate, S, of 1.74×10^{17} W (4.16×10^{16} cal s^{-1}). This quantity, divided by the area of the planar projection of the earth, 1.28×10^{14} m^2, is called the **solar constant,** I_{sc}.[1] Thus $I_{sc} = 1367$ W m^{-2} (2821 cal cm^{-2} day^{-1}). To simplify our discussion, we take $S = 100$ units of radiant energy input and trace out the fate of this energy in the earth–atmosphere system prior to its ultimate reflection or reradiation back to space (Figure 3-2). All these energy values are estimates of globally and seasonally integrated averages of values that are highly variable in time and space.[2]

Of the 100 units of incident energy, 26 are reflected from the atmosphere (20 by clouds) back to space. Clouds absorb 4, and atmospheric gases about 16, of the remaining units, so 54 units are incident upon the earth's surface. The surface reflects 4 of these, so 50 units are absorbed at the surface to cause warming, evaporation of water, and melting of snow and ice.[3]

To a high degree of approximation, the rate of energy output from the earth–atmosphere system equals the rate of input; thus the 70 units of solar energy absorbed by the earth and atmosphere are eventually reradiated to outer space.[4] The overall temperature of the earth–atmosphere system (the **planetary temperature**) is about 253 K (−20 °C) (Miller et al. 1983), so this radiation is at a much

[1]Recent measurements and analyses suggest that the energy output of the sun varies about 1 percent over an 80- to 90-year cycle (Reid 1987).

[2]A detailed model for estimating the daily clear-sky solar radiation incident on a sloping portion of the earth's surface is developed in Appendix E.

[3]Recent research (Cess et al. 1995) strongly suggests that clouds absorb 15 units of radiant energy, rather than 4. This would reduce the amount absorbed at the surface to 39 units and commensurately reduce the transfer from the surface to the atmosphere.

[4]There is reason to believe that the earth–atmosphere system is warming. Although this warming could be climatologically and hydrologically significant (see Section 3.2.9), it represents only a negligibly small fraction of the total energy budget and thus can be ignored for purposes of energy-budget analysis.

FIGURE 3-1
Spectra of energy (a) emitted by a blackbody at 6000 K, (b) received at the earth's surface (global average), (c) emitted by a blackbody at 290 K, (d) emitted to space by the earth–atmosphere system (global average). Upper graph shows absorption spectrum for principal absorbing gases in the atmosphere. Modified from Barry and Chorley (1982) and Miller *et al.* (1983).

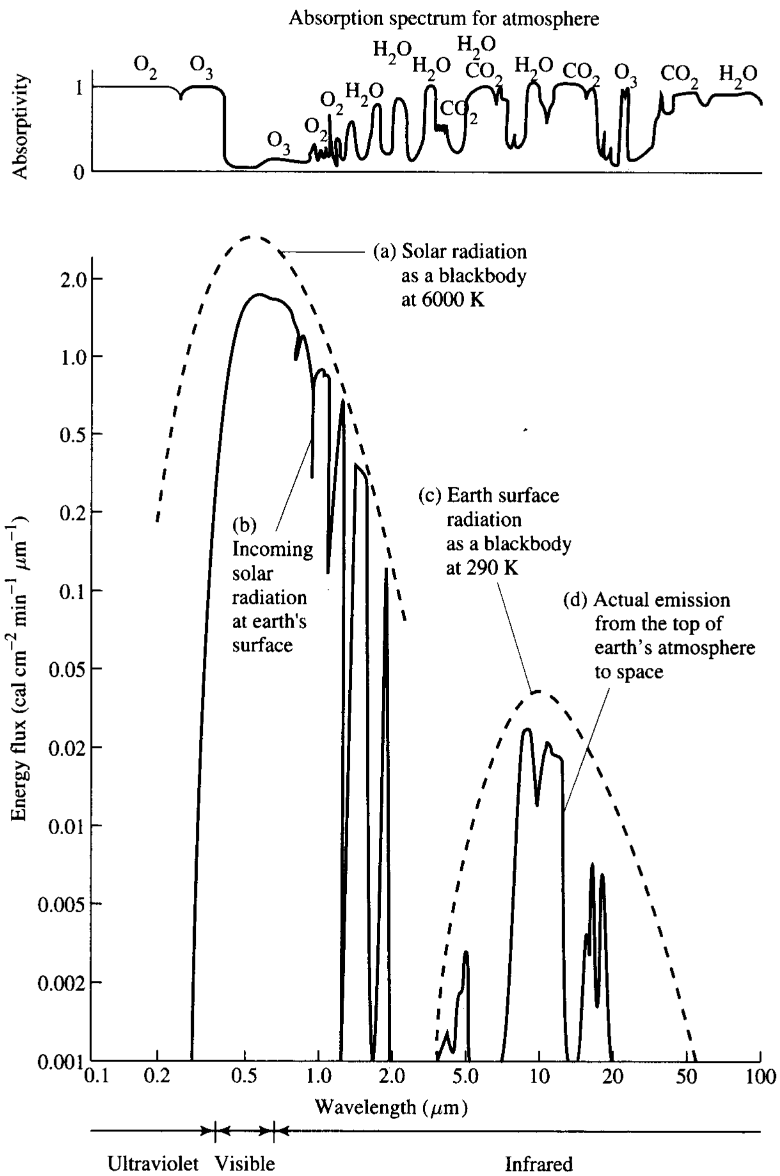

smaller rate and at much longer wavelengths than is the solar radiation [Equations (D-1) and (D-3)]. The equality of the total incoming solar energy and outgoing terrestrial radiation is reflected in the equality of the areas under the two spectral curves when plotted on arithmetic scales as in Figure 3-3.

The steps by which solar radiation is transformed into earth radiation are the critical determinants of the earth's climate. As noted above, 50 units of energy are absorbed to heat the surface and provide latent heat for evaporation and melting. Because the earth's surface, like the system as a whole, is in essential balance, this energy must be transferred away. This transfer is accomplished via three modes: (1) radiation (20 units); (2) latent-heat transfer (24 units); and (3) conduction/convection (6 units). The basic physics of these energy-transfer modes is described in Appendix D.

The average temperature of the earth's surface is about 290 K (17 °C), so the surface radiates approximately as a blackbody at this temperature and emits 20 units of energy in the infrared range between wavelengths of 4 and 50 μm (Figure 3-1, curve *c*). Energy in this wavelength band is referred

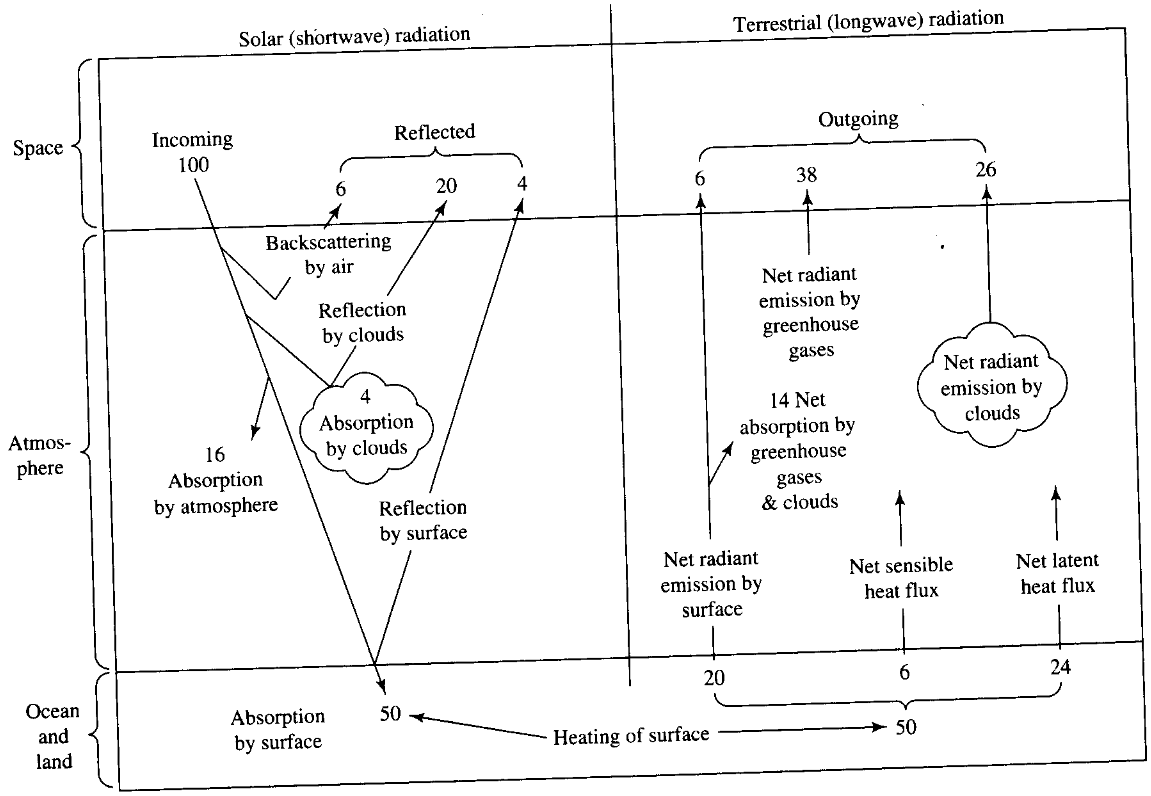

FIGURE 3-2
Average global energy balance of the earth–atmosphere system. Numbers indicate relative energy fluxes; 100 units equals the solar constant, 1367 W m^{-2}. Modified from Shuttleworth (1991); data from Peixoto and Oort (1992).

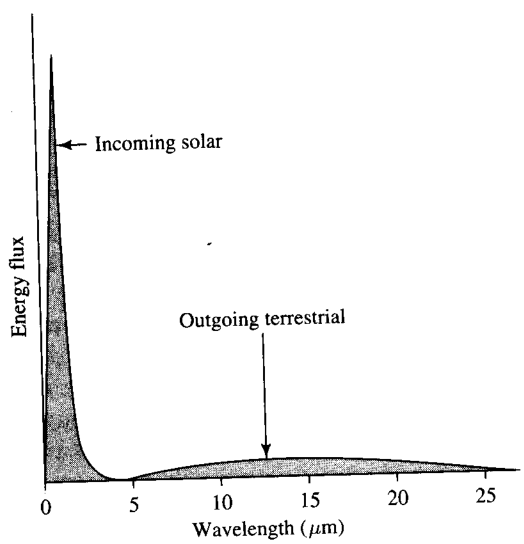

FIGURE 3-3
Spectra of incoming solar and outgoing terrestrial radiation plotted on arithmetic scales. Compare Figure 3-1. After Barry and Chorley (1982).

to as **terrestrial** or **longwave radiation**. As shown in the upper portion of Figure 3-1, many naturally occurring and human-introduced gases strongly absorb longwave radiation, so that 14 of the 20 units radiated by the surface are absorbed to heat the atmosphere. The absorption of this energy is called the **greenhouse effect**; the most important "greenhouse gases" are water vapor (which accounts for 65% of the absorption), carbon dioxide (33%), and methane, nitrous oxide, ozone, and chlorinated fluorocarbons (2% combined).

The components of the atmosphere also radiate energy in all directions. The net effect of the exchange of radiant energy between the surface and the atmosphere is the upward transfer of the 20 units of energy, of which 6 are radiated directly to outer space.

The transfer of latent heat via evaporation (mostly from the oceans) adds another 24 units of energy to the atmosphere; this is the largest source of atmospheric energy. Sensible heat transfer (con-

BOX 3-1

Energy-Balance Model of Global Radiational Temperature

We can apply some of the basic physics of energy transfer discussed in Section D.1 to develop a simple "zero-dimensional" energy-balance model of the temperature of the earth–atmosphere system. The long-term average rate of energy input to this system, i [E T^{-1}], equals the solar flux, S [E T^{-1}], minus the fraction, a_p, of this arriving energy that is reflected by the system:

$$i = S \cdot (1 - a_p). \tag{3B1-1}$$

To maintain equilibrium, the average rate at which the system radiates energy to outer space, q, must equal i. From the Stefan-Boltzmann Law (Equation D-1) this rate is

$$q = \sigma \cdot T_p^4 \cdot A, \tag{3B1-2}$$

where σ is the Stefan-Boltzmann constant, T_p is the effective radiating temperature of the system (assuming an emissivity of 1), and A is the surface area of the system.

Equating i and q and solving for T_p yields

$$T_p = \left[\frac{S \cdot (1 - a_p)}{\sigma \cdot A}\right]^{1/4}. \tag{3B1-3}$$

Equation (3B1-3) shows how the radiating temperature of the earth–atmosphere system (called the **planetary temperature**) depends on the solar constant and the reflectivity of the system (called the **planetary albedo**).

$S = 1.74\times10^{17}$ W, $\sigma = 5.78\times10^{-8}$ W m^{-2} K^{-4}, and A is 5.10×10^{14} m^2. From Figure 3-2, we see that the value of a_p is 0.3. Inserting these values in Equation (3B1-3) gives $T_p = 253.6$ K, which is quite close to the value of 253 K quoted in the text. (The difference is due to rounding errors in the numbers in Figure 3-2 and to uncertainty in the true value of a_p.)

Exercise 3-1 gives you an opportunity to explore this question by using this simple model. A simple model for calculating the earth's surface temperature is described in Box 3-2.

---

duction/convection) contributes another 6 units because the surface is, on average, warmer than the overlying air.

If we focus on the energy balance of the atmosphere (including clouds) in Figure 3-2, we see that 69% of the input, 44 units, comes from the earth's surface, while only 31% (20 units) is absorbed directly from solar radiation. The 22% due to absorption of longwave radiation via the greenhouse gases is a critical determinant of the earth's climate: As noted by Ramanathan (1988), without the greenhouse effect the earth's surface would have a temperature of −18 °C and be covered with ice. The potential climatic and hydrologic effects of the increases in concentrations of greenhouse gases due to industrial activity and the clearing of forests are reviewed in Section 3.2.9.

The emission spectrum of the earth–atmosphere system as viewed from space is shown in Figure 3-1 (curve d); this curve represents the emission spectrum of the surface depleted by absorption by greenhouse gases, and it is this radiation to outer space that completes the overall energy balance of the earth–atmosphere system.

Box 3-1 develops a simple energy-balance model that shows how the planetary temperature of the earth is related to the solar constant and the reflectivity of the system, and Box 3-2 describes a model for estimating the earth's surface temperature based on the energy balance for a two-layer atmosphere. These models can be used to explore the sensitivity of these temperatures to changes in the solar constant, the albedo, and other factors (Exercises 3-1 and 3-3).

3.1.2 Latitudinal Energy Transfer

Figures 3-4 and 3-5 summarize the geometrical relations of the earth's orbit that cause seasonal and latitudinal variations in the receipt of solar energy. Figure 3-4 shows how a given energy flux is spread out over larger areas at high latitudes because the earth is a sphere. This strictly latitudinal effect is modified seasonally because the earth's axis of ro-

BOX 3-2

Energy-Balance Model of Earth-Surface Temperature

This model is a modification of the one described by Harte (1985). Harte (1985) shows that it is appropriate, given the physics of radiation, to divide the earth's atmosphere into a lower layer (extending to an altitude of 1.8 km and containing 20% of the air and 50% of the water vapor), which is the major absorber of the terrestrial radiation and an upper layer (containing 80% of the air and 50% of the water). The model is developed by formulating three energy-balance equations: (1) one for the earth–atmosphere system as a whole; (2) one for the upper layer of the atmosphere; and (3) one for the lower layer of the atmosphere. All the energy terms are expressed as long-term average fluxes [$E\,T^{-1}$], all temperatures are absolute, all emissivities are equal to 1, and it is assumed that each of these systems is in equilibrium.

Energy enters the earth–atmosphere system from above at the rate S and from below at the rate W (which represents the heat generated from nuclear and fossil fuels). Energy leaves the system by three routes: (1) reflected solar radiation; (2) thermal radiation from the top of the atmosphere; and (3) the portion of thermal radiation from the surface that is not absorbed in the atmosphere, $(1-f)\cdot\sigma\cdot T_s^4\cdot A$, where f is the fraction of surface radiation absorbed in the atmosphere, σ is the Stefan-Boltzmann constant, A is the area of the earth, and T_s is the surface temperature (absolute). Thus the energy balance for the system is

$$S + W = a_p\cdot S + \sigma\cdot T_u^4\cdot A + (1-f)\cdot\sigma\cdot T_s^4\cdot A, \qquad \textbf{(3B2-1)}$$

where a_p is the planetary albedo and T_u is the absolute temperature of the upper atmospheric layer.

The upper atmospheric layer absorbs a fraction k_u of the solar radiation that strikes it, and it also receives (1) energy radiated upward from the lower layer and (2) one-half the latent heat that accompanies evaporation from the surface (because this layer holds one-half the atmospheric water vapor). The upper layer loses energy by thermal radiation upward to outer space and downward to the lower layer. Thus the energy balance for the upper layer is

$$k_u\cdot S + \sigma\cdot T_l^4\cdot A + 0.5\cdot Q_e = 2\cdot\sigma\cdot T_u^4\cdot A, \qquad \textbf{(3B2-2)}$$

where T_l is the absolute temperature of the lower layer and Q_e is the latent-heat flux from the surface.

Energy enters the lower atmospheric layer from above by the absorption of a fraction k_l of the solar radiation that enters it and by thermal radiation from the

---

tation is tilted at an angle of 23.5° to the orbital plane (Figure 3-5); the seasons are in fact caused by the contrasts in solar radiation receipt as the northern and southern hemispheres are alternately tilted toward (summer) and away from (winter) the sun.[5] Figure 3-6 quantifies the seasonal and latitudinal variations of solar radiation incident at the top of the atmosphere.

The top curve of Figure 3-7 shows the difference between solar radiation received and the terrestrial radiation emitted at each latitude. The net radiation balance is positive for latitudes below about 35° and negative poleward of that. Because total energy inputs and outputs must be in balance at all latitudes, there is a net poleward transfer of energy from the regions of surplus to those of deficit; the magnitude of this transfer is indicated by the total flux curve in the lower part of Figure 3-7.

This poleward, or meridional, energy transfer is accomplished by air and ocean currents. Roughly two-thirds of the total transfer occurs as sensible- and latent-heat transfer in the atmosphere and one-third as sensible-heat transfer in the oceans; the latitudinal importance of these modes is also indicated in the lower part of Figure 3-7.

[5]The orbital tilt is known to vary between 22.1° and 24.3°, with a periodicity of about 40,000 yr. This variability and other periodic fluctuations in the geometry of the earth's orbit affect the amount of solar radiation received seasonally in the two hemispheres over time. It is now widely accepted that these orbital variations controlled the timing of the glacial and interglacial periods of at least the last ice age (Hays et al. 1976; Lamb 1982).

upper layer. From below, energy enters from (1) the absorbed portion of thermal radiation from the surface, $f \cdot \sigma \cdot T_s^4 \cdot A$, (2) one-half the latent-heat flux from the surface, Q_e, (3) the sensible-heat flux from the surface, Q_h, and (4) the anthropogenic heat flux. Energy is lost from this layer by upward and downward radiation. Thus the energy balance for the lower layer is

$$k_l \cdot S + \sigma \cdot T_u^4 \cdot A + f \cdot \sigma \cdot T_s^4 \cdot A + 0.5 \cdot Q_e + Q_h + W = 2 \cdot \sigma \cdot T_l^4 \cdot A. \quad \textbf{(3B2-3)}$$

Equations (3B2-1) to (3B2-3) are a system of three equations in three unknowns, the temperatures T_u, T_l, and T_s; the other quantities are parameters whose values must be given. The values of the temperatures can be found via the following steps:

1. Solve Equation (3B2-1) for T_u in terms of T_s and parameters.
2. Solve Equation (3B2-2) for T_l in terms of T_u and parameters.
3. Substitute the results of Step 1 into the results of Step 2 to give an equation for T_l in terms of T_s and parameters.
4. Solve Equation (3B2-3) for T_s in terms of T_u, T_l, and parameters.
5. Put the results of Step 1 and the results of Step 3 into the results of Step 4 and simplify to give the equation for T_s as a function of parameters.

The resulting expression is

$$T_s = \left[\frac{(3 - 3 \cdot a_p - 2 \cdot k_u - k_l) \cdot S - 1.5 \cdot Q_e - Q_h + 2 \cdot W}{(3 - 2 \cdot f) \cdot \sigma \cdot A} \right]^{1/4}. \quad \textbf{(3B2-4)}$$

The values given by Harte (1985), which are generally consistent with those in Figure 3-2, are:

$S = 1.74 \times 10^{17}$ W	$a_p = 0.3$
$Q_e = 4.08 \times 10^{16}$ W	$k_u = 0.18$
$Q_h = 8.67 \times 10^{15}$ W	$k_l = 0.075$
$W = 1.07 \times 10^{13}$ W	$f = 0.950.$

With these values, Equation (3B2-4) gives $T_s = 290.4$ K, close to the actual value of 290 K.

Exercise 3-2 asks you to derive Equation (3B2-4) by following the above steps. Exercise 3-3 gives you an opportunity to use the model to explore the greenhouse effect.

3.1.3 The General Circulation and the Distribution of Pressure and Temperature[6]

The unequal latitudinal distribution of radiation and the requirement for the conservation of angular momentum on the rotating earth give rise to a system of three circulation cells in the latitude bands 0°–30°, 30°–60°, and 60°–90° in each hemisphere, along with the jet streams and characteristic prevailing surface-wind directions (Figure 3-8). This system is called the **general circulation** of the atmosphere. The cell nearest the equator is responsible for most of the poleward energy transfer between latitudes 0° and 30°, but mechanisms other than the general circulation dominate the atmospheric transfer at higher latitudes. As indicated in Figure 3-9, winds circulating in large-scale horizontal eddies—both the quasi-stationary zones of high and low pressure discussed later and the moving cyclonic storms that dominate weather systems in the mid-latitudes—are the major agents of transport above latitude 30° (Barry and Chorley 1982).

Figure 3-8 shows that the general circulation results in regions of rising air near the equator and near latitude 60°, and descending air near latitude 30° and the poles. We would expect the zones of ascent to be characterized by relatively low atmos-

[6] Much of the discussion in this section is based on Miller et al. (1983).

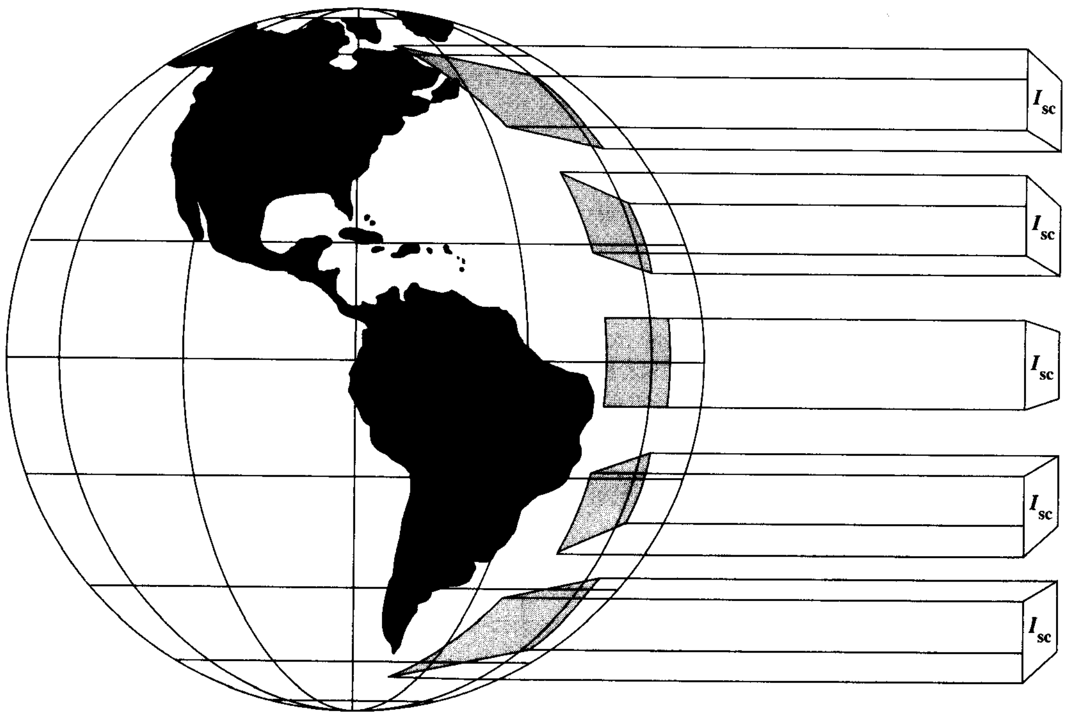

FIGURE 3-4
Variation of solar radiation intensity ([E L^{-2} T^{-1}]) with angle of incidence. At higher angles (higher latitudes), a given energy flux is spread over a larger area. From Day and Sternes (1970), used with permission.

pheric pressures at the surface, and those of descent by high pressures. Maps of average sea-level pressures (Figure 3-10) generally confirm these expectations, though the zones of high and low pressure actually occur as cells rather than continuous belts.

Horizontal pressure gradients are the basic driving force for winds, and the resultant of these pressure forces with forces produced by the motion itself (centrifugal forces, the Coriolis effect due to the earth's rotation, and friction) produces surface winds that move approximately parallel to the isobars, but with a tendency to spiral inward toward low-pressure centers and outward from high-pressure centers. In the northern hemisphere, the sense of circulation is clockwise around highs (**anticyclonic circulation**) and counterclockwise around lows (**cyclonic circulation**) (Figure 3-11); the circulations are in the opposite senses in the southern hemisphere.

The subtropical high-pressure zone exists as cells over the Pacific and Atlantic Oceans; these cells are especially well defined in the summer, and occur farther to the north in the summer than in the winter. Winds are moving clockwise around these highs, so the coastal areas of southwestern North America and Europe are subject to dry, cool northerly winds in the summer. Conversely, the southeastern United States, Hawaii, the Philippines, and southeast Asia are subject to warm, moist winds from the tropics and have warm, humid summers with frequent rain.

The subpolar low-pressure zone occurs as cells over the northern Pacific and Atlantic, which are especially evident in winter. These cells, called the Aleutian low (Pacific) and Icelandic low (Atlantic), are "centers of action", where major mid-latitude cyclonic storms develop their greatest intensities.

Figure 3-12 shows the global distribution of mean temperature in January and July. Clearly, this distribution is strongly related to latitude and hence to the average receipt of solar radiation, but it is modified by the distribution of the continents and oceans. Because of water's very high heat capacity (Section B.2.4), the annual temperature range of

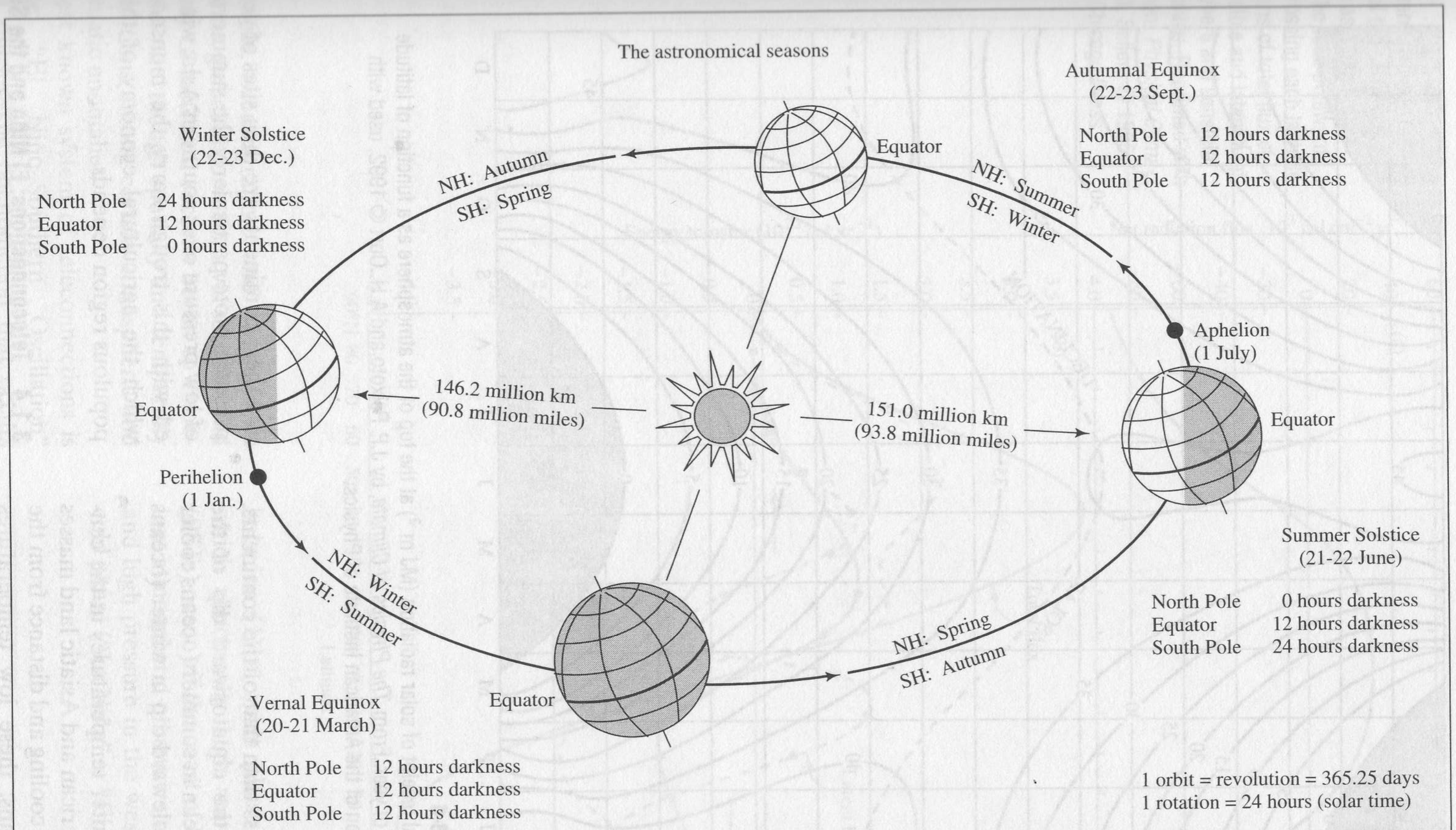

FIGURE 3-5
Revolution of the earth around the sun, showing that the occurrence of summer and winter in the northern and southern hemispheres is determined by the 23.5° tilt of the rotational axis toward or away from the sun. Reprinted with permission of Macmillan Publishing Co. from *Climatology* by Oliver and Hidore, © 1984 by Bell & Howell Co.

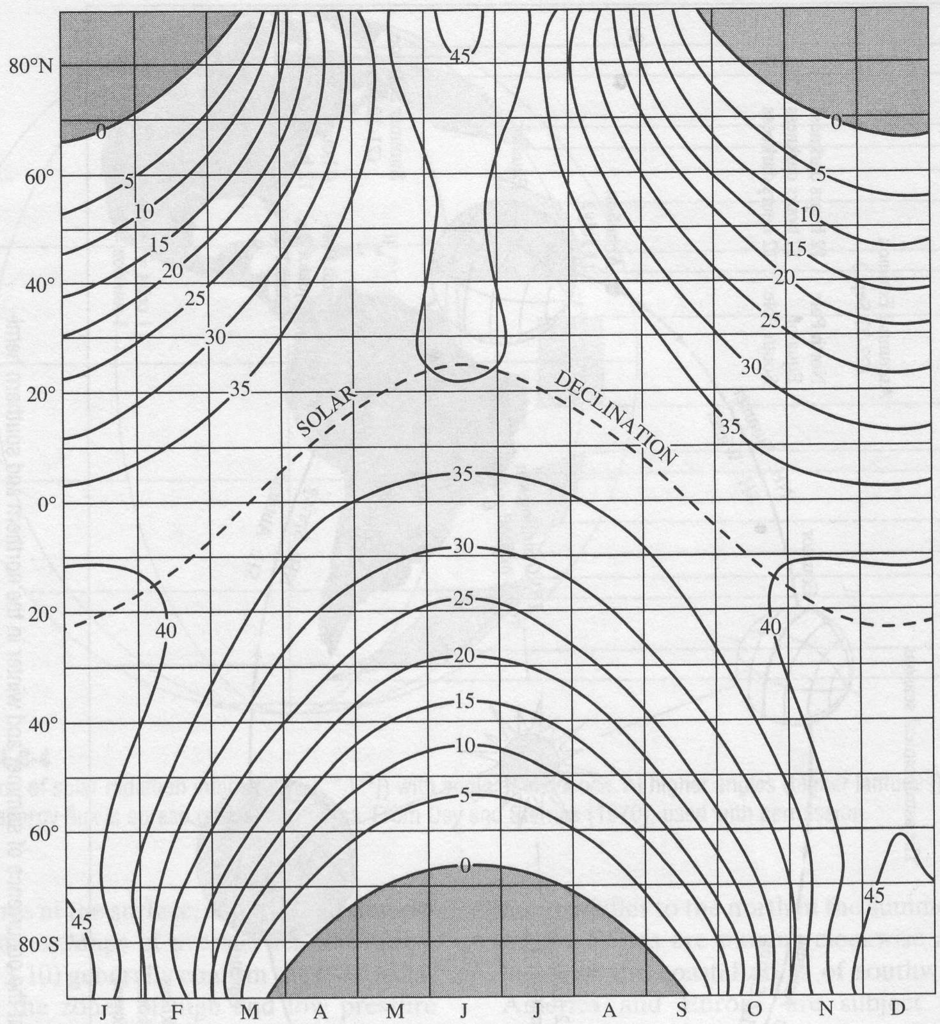

FIGURE 3-6
Daily total receipt of solar radiation (MJ m^{-2}) at the top of the atmosphere as a function of latitude and time of year. From *The Physics of Climate,* by J.P. Peixoto and A.H. Oort © 1992, used with permission of the American Institute of Physics.

the oceans is much less than that of the continents. This is reflected in the equatorward dip of the isotherms over the ocean in summer (oceans cooler than land), and the poleward dip in winter (oceans warmer than land).

The very cold winter temperatures in the centers of the North American and Asiatic land masses are due to radiational cooling and distance from the relatively warm oceans; these low temperatures produce cells of high density and high pressure. [See Equation (D-5).] The situation is reversed in summer, when extensive radiational heating occurs, and these continents are then sites of generally low pressure. Note particularly the summertime trough of low pressure over southern Asia; winds associated with this trough carry the monsoon rains on which the agricultural economy of this vast and populous region depends.

3.1.4 Teleconnections: El Niño and the Southern Oscillation

A **teleconnection** is a climatic anomaly that is a distant consequence of another climatic anomaly. In

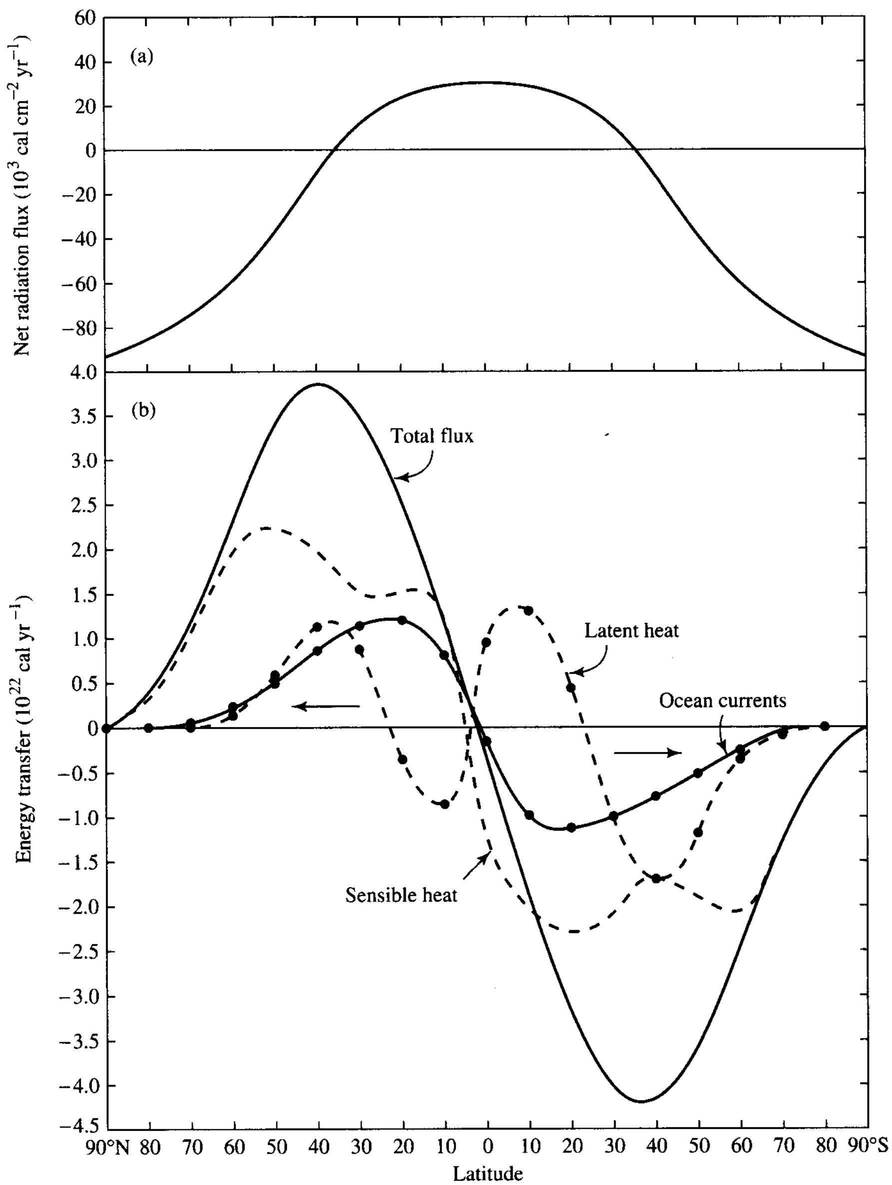

FIGURE 3-7
(a) The long-term average radiation balance of the earth–atmosphere system as a function of latitude. (b) The total poleward energy flux crossing each latitude and the portions of total flux effected by sensible and latent heat in the atmosphere and sensible heat in the oceans. Reprinted with permission from *Physical Climatology* by W.D. Sellers © 1965, University of Chicago Press.

the late 1960s, oceanographic and atmospheric measurements, global observations via satellite, and careful study of historical records began to establish some definite, though spatially and temporally variable, relations among certain atmospheric and oceanic climatic anomalies.

The best known system of teleconnections is called the "El Niño–Southern Oscillation" (ENSO), a quasi-cyclic phenomenon that occurs every three to seven years and has persisted for at least the last 450 years (Rasmussen 1985; Enfield 1989). This phenomenon consists of an oscillation between (1) a warm phase ("El Niño"), during which abnormally high sea-surface temperatures (SSTs) occur off the coast of Peru[7] accompanied by low atmospheric pressure over the eastern Pacific and high pressure in the western Pacific and (2) a cold phase ("La Niña" or "El Viejo") with low SSTs

[7]The term "El Nino" refers to the Christ Child and was given by Peruvian fishermen (whose catches were adversely affected by the phenomenon) because the abnormal warming usually becomes pronounced around Christmas.

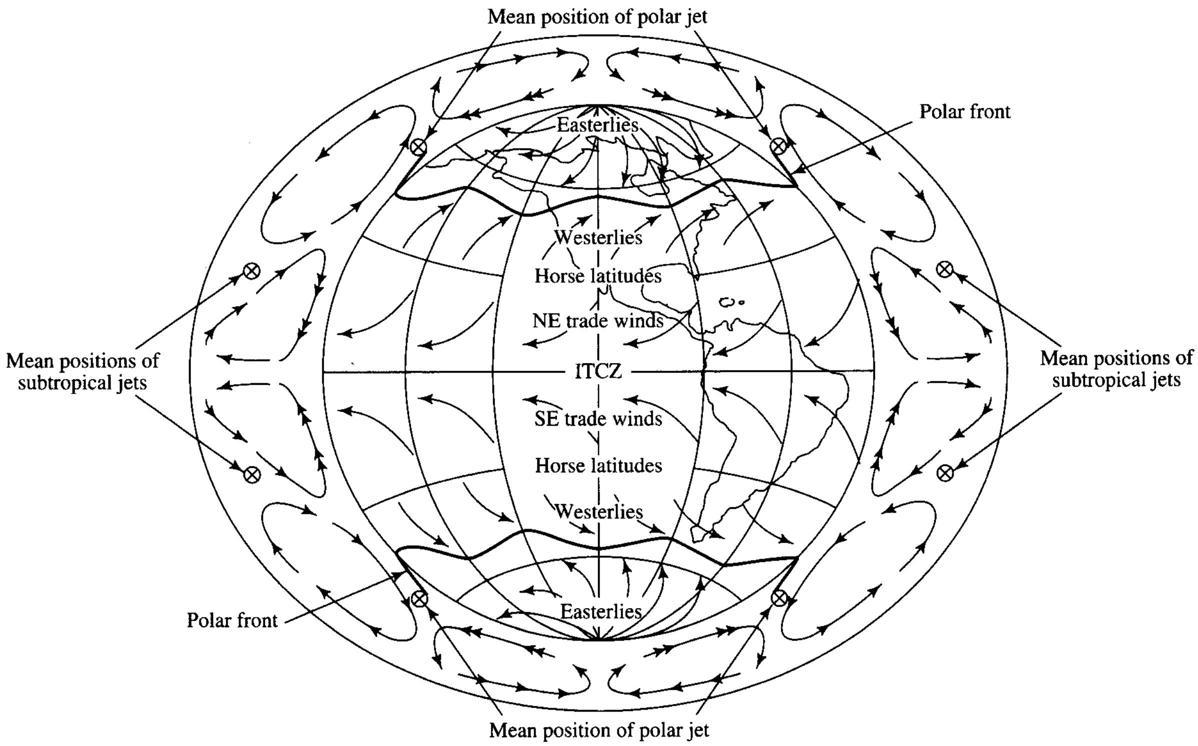

FIGURE 3-8
The general circulation of the atmosphere. Double-headed arrows in cross section indicate that the wind has a component from the east. Reprinted with permission of Prentice-Hall from *Elements of Meteorology*, 4th ed., by Miller et al. © 1984 by Bell & Howell Co.

in the eastern Pacific and the opposite pressure anomalies.

The typical ENSO warm episode evolves and declines over an approximately two-year period (Harrison and Larkin 1998). It begins in the late spring to fall of year 1 with abnormally strong westerly winds in the equatorial Indian Ocean, low pressures in eastern Australia, and warming SSTs in the South Pacific. As winter progresses, a tongue of abnormally warm water forms off the coast of Peru; this intensifies and builds westward along the equator during the spring and summer of year 2. The peak of the cycle usually occurs between July and December of year 2, with abnormally high SSTs extending westward to the International Date Line. These are accompanied by abnormal westerly winds and strong convergence along the equator, high pressures and lowered sea levels in the western Pacific and Indonesia, and low pressures and elevated sea levels in the eastern Pacific. A pool of abnormally cold water and enhanced westerly winds also occurs near latitude 45° in the North Pacific. The declining phase typically begins in January to April of year 3, when the equatorial pool of high SSTs begins to shrink, and most of the SST, wind, and pressure anomalies dissipate by the end of the summer of year 3.

There is considerable evidence that ENSO is an inherently oscillatory phenomenon that requires no outside forcing. The end of an ENSO episode begins when the eastward waves of warm water are reflected off South America and, in a complicated process that involves poleward circulation of the reflected westward-moving surface water and atmospheric processes, the SST returns to its original levels and the easterly trade-wind flow is re-established (Enfield 1989). Continued cooling of SSTs

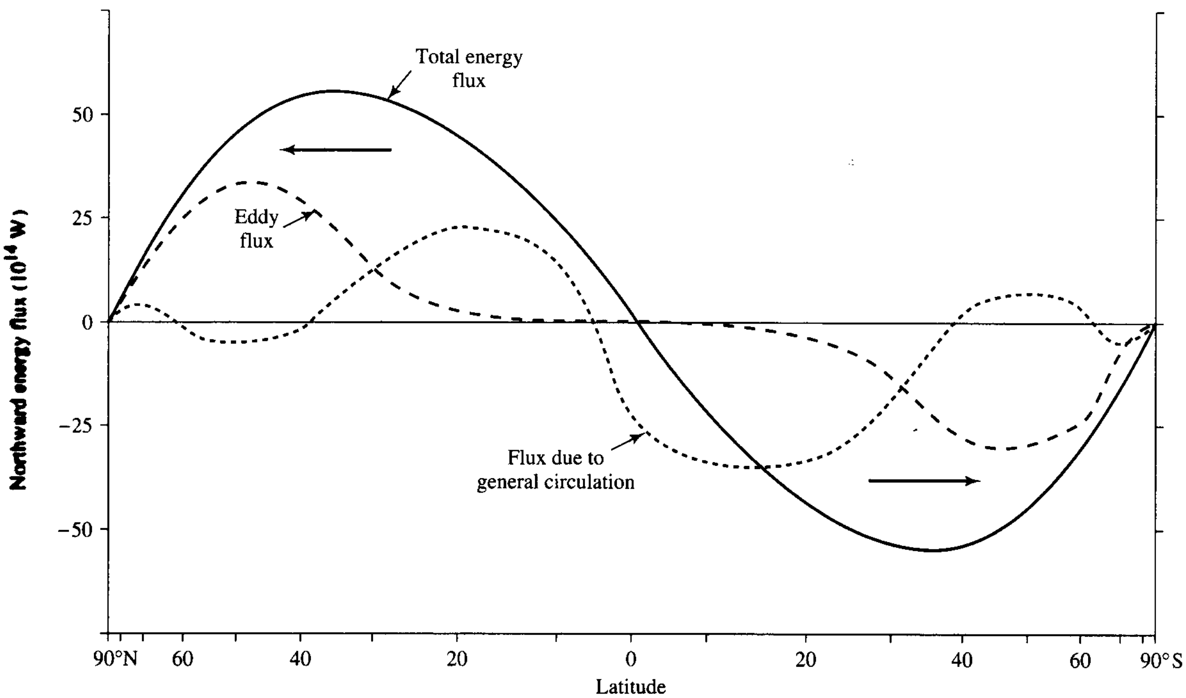

FIGURE 3-9
Total poleward energy flux and components of total flux carried as latent and sensible heat in the general circulation of the atmosphere and in winds associated with horizontal eddies. After Barry and Chorley (1982).

the eastern Pacific leads to the cold phase of ENSO.

Although ENSO is essentially the product of large-scale, long-period waves in the surface of the tropical Pacific Ocean, it shifts the jet stream in the eastern North Pacific and North America to the south (warm phase) or north (cold phase). These shifts can steer unusual weather systems into low- and mid-latitude regions around the world. The result is unusually warm or cold winters in particular regions, drought in normally productive agricultural areas, and torrential rains in normally arid regions (Rasmussen 1985). Some of the teleconnections associated with ENSO episodes are indicated in Figures 3-13 and 3-14; the most consistent are the severe droughts in Australia and northern South America and heavy rainfall in Ecuador and northern Peru. In other places the effects can vary from episode to episode depending on the state of the atmosphere. For example, the 1976–1977 event was associated with drought along the west coast of the United States; that of 1982–1983 produced increased storminess (Enfield 1989). The severe drought in the north-central United States in the summer of 1988 (Figure 10-34c) was a consequence of the 1986–1987 ENSO event (Trenberth et al. 1988). The strong 1997–1998 event produced warm and dry conditions from India to northern Australia (leading to extensive forest fires in Indonesia); dry conditions in the eastern Amazon region; a wet winter with considerable flooding along the West Coast, Gulf Coast, and south Atlantic Coast of the United States; and a warm winter in the northeastern United States. A source for current information on ENSO is given in Appendix G.

A number of studies have found relationships between streamflows and ENSO cycles (e.g., Dracup and Kahya 1994; Eltahir 1996; Piechota et al. 1997; Amarasekera et al. 1997). ENSO anomaly patterns persist for several months, so useful long-range hydrological forecasts can be made for the regions shown in Figures 3-13 and 3-14 (Halpert and Ropelewski 1992).

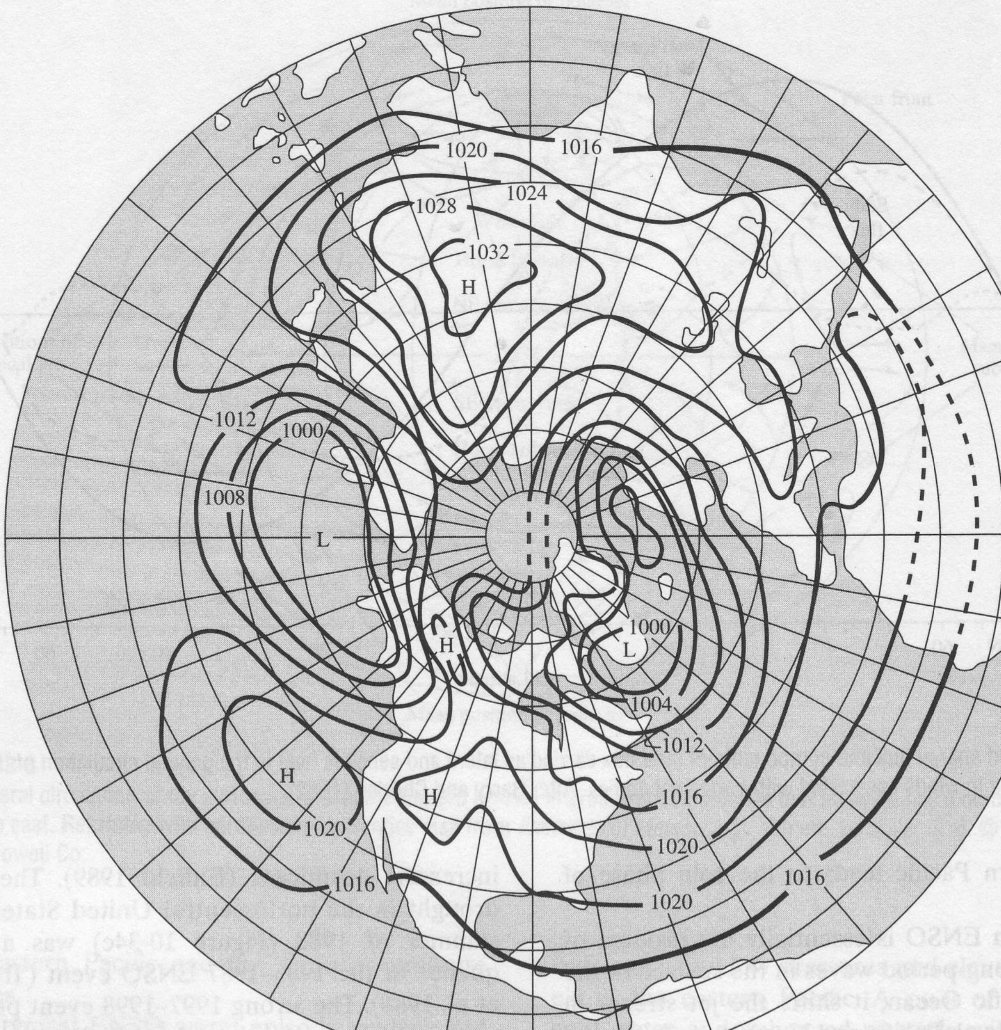

FIGURE 3-10
Normal sea-level pressures (mb) in the northern hemisphere in (a) January and (b) July. Reprinted with permission of Prentice-Hall from *Elements of Meteorology*, 4th ed., by Miller *et al.* © 1984 by Bell & Howell Co.

3.2 THE GLOBAL HYDROLOGIC CYCLE

3.2.1 Stocks and Fluxes in the Global Cycle

Figure 3-15 is a snapshot of the global hydrologic cycle in action. This "cycle" is actually a complex web of continual flows, or **fluxes**, of water among the major "reservoirs", or **stocks** of water (Figure 3-16). The sun provides the energy that causes evaporation and mixes water vapor in the atmosphere and thereby drives the cycle against the pull of gravity.

As is shown in Tables 3-1 and 3-2 and Figure 3-17, 96.5% of the water on earth is in the oceans. Of the fresh water, 69% is in solid form in glaciers[8]

[8]The proportion of the earth's water in glaciers was, of course, considerably larger as recently as 18,000 years ago, when the last glaciation was at its peak and the total volume of glacier ice was about three times its present value; at other periods of earth history there were no glaciers.

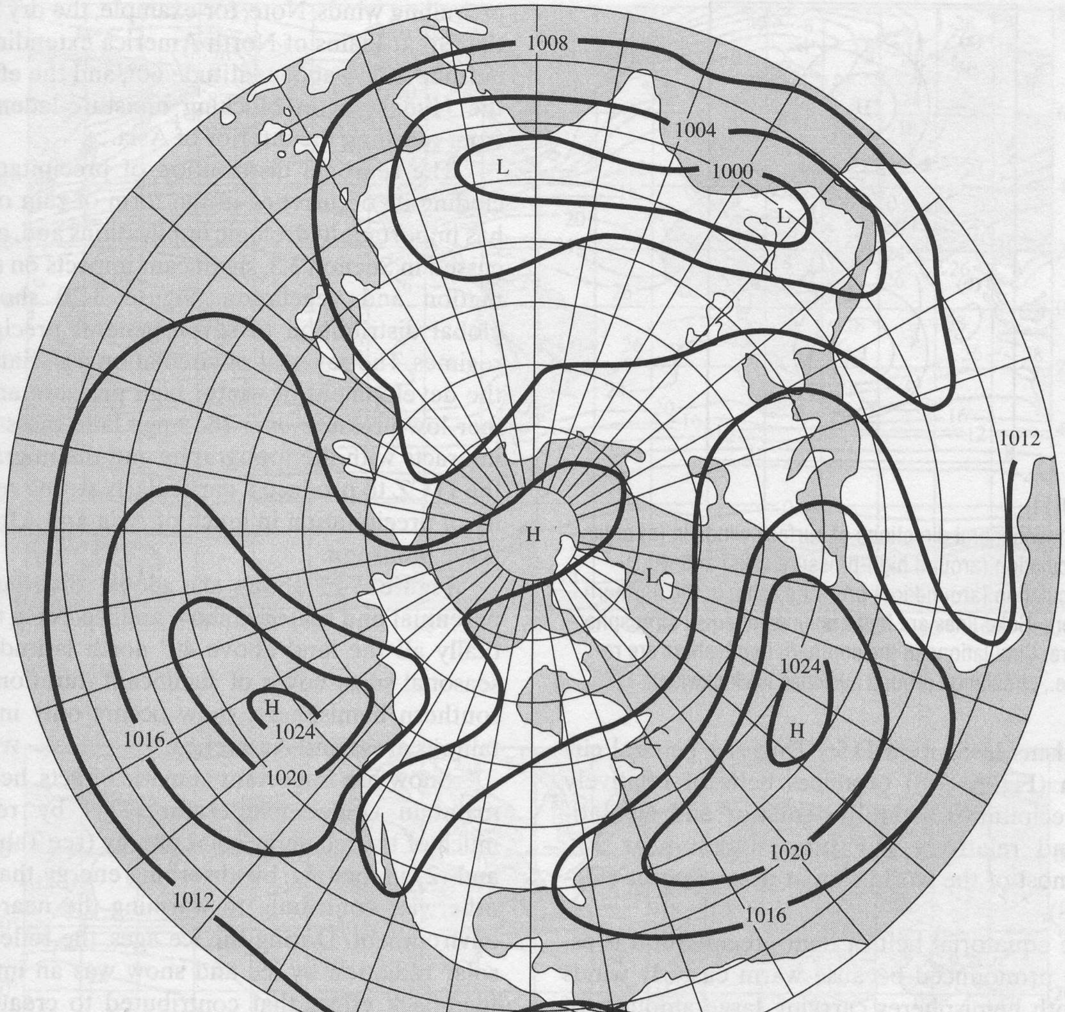

FIGURE 3-10 (Continued)

and 30% is ground water; only 1% is in surface-water bodies.

The major features of the global cycle are: (1) the oceans lose more water by evaporation than they gain by precipitation; (2) the land surfaces receive more water as precipitation than they lose by evapotranspiration; and (3) the excess of water on the land returns to the oceans as runoff, balancing the deficit in the ocean–atmosphere exchange. The oceanic fluxes dominate the cycle: oceans receive 79% of the global precipitation and contribute 88% of the global evapotranspiration.

As was noted in Section 2.8.1, the flow of water from one reservoir to another implies that the water *within* each of the reservoirs is also continually in motion. The average residence time (average length of time a molecule of water is in a given reservoir) can be calculated from Equation (2-27); Exercise 3-8 asks you to calculate the residence times for the various stocks in Figure 3-16.

3.2.2 Distribution of Precipitation

Regions characterized by rising air tend to have relatively high average precipitation, and those characterized by descending air tend to have low precipitation. (See the discussion of precipitation

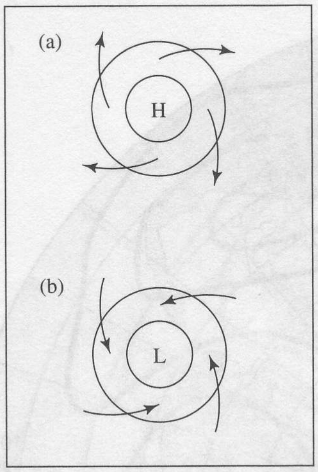

FIGURE 3-11
Arrows show general directions of surface winds in (a) anticyclonic circulation (around high-pressure cells) and (b) cyclonic circulation (around low-pressure cells) in the northern hemisphere. Solid lines are **isobars:** lines of equal atmospheric pressure. Circulations in the southern hemisphere are reversed (i.e., circulation around cyclones is clockwise).

mechanisms in Section D.5.) Thus the general circulation (Figure 3-8) produces belts of relatively high precipitation near the equator and 60° latitude, and relatively low precipitation near 30°, where most of the world's great deserts occur (Figure 3-18).

The equatorial belt of high precipitation is especially pronounced because warm easterly winds from both hemispheres carrying large amounts of moisture evaporated from tropical oceans converge in this zone; this phenomenon is called the **intertropical convergence zone** (ITCZ). The peaks of precipitation coincident with the mid-latitude zone of rising air are produced mainly by extratropical cyclonic storms that tend to develop along the polar front.

Because precipitation rates are influenced by topography, air temperatures, frontal activity, and wind directions in relation to moisture sources, global precipitation patterns (Figure 3-19) show significant deviations from the general latitudinal distribution depicted in Figure 3-18. The major causes of these deviations are mountain ranges, such as the Rocky Mountain–Andean chain, the Alps, and the Himalayas. These ranges induce high rates of precipitation in their immediate vicinity and, typically, produce "rain-shadow" zones of reduced precipitation over large areas leeward of the prevailing winds. Note, for example, the dry zone in the Great Plains of North America extending from latitude 20° to above latitude 60°, and the effects of the Himalayas in blocking moisture-laden winds from reaching the interior of Asia.

The seasonal distribution of precipitation, including its occurrence in the form of rain or snow, has important hydrologic implications and, as is discussed in Section 3.3, significant impacts on soil formation and vegetation. Figure 3-20 shows the global distribution of seven general precipitation regimes. The reversal of circulation associated with the development of winter high pressure and summer low pressure over the huge land mass of Asia interacts with the topography and the migration of the ITCZ to produce a particularly strong seasonality of precipitation in much of Asia and Africa; this is the **monsoon.**

Figure 3-21 shows the global distribution of perennial and seasonal snow and ice. Note that virtually all the land above 40° north latitude has a seasonal snow cover of significant duration; in the southern hemisphere, snow occurs only in mountainous areas and Antarctica.

Snow has important climatic effects, helping to maintain colder temperatures (1) by reflecting much of the incoming solar energy (see Table D-2), and (2) in melting, by absorbing energy that would otherwise contribute to warming the near-surface environment. During the ice ages, the reflection of solar radiation by ice and snow was an important feed-back effect that contributed to creating and maintaining a colder climate. Under present conditions, the surface cooling induced by snow has profound effects on surface and air temperatures, global circulation patterns and storm tracks, and precipitation (Berry 1981; Walsh 1984; Barnett et al. 1988; Leathers and Robinson 1993; Groisman et al. 1994). A number of studies (Dey and Kumar 1983; Dickson 1984) have shown an inverse relation between the extent of winter snow cover in Eurasia and the amount of rainfall in India during the ensuing summer monsoon (Figure 3-22).

Snow also acts as an insulating blanket that helps to retain heat in the soil, which is important hydrologically as well as biologically: if soil is prevented from freezing, its ability to accept infiltrating water is generally enhanced (Dingman 1975). However, the principal hydrologic effect of snow is to delay the input of precipitated water into the land phase of the hydrologic cycle and thus to af-

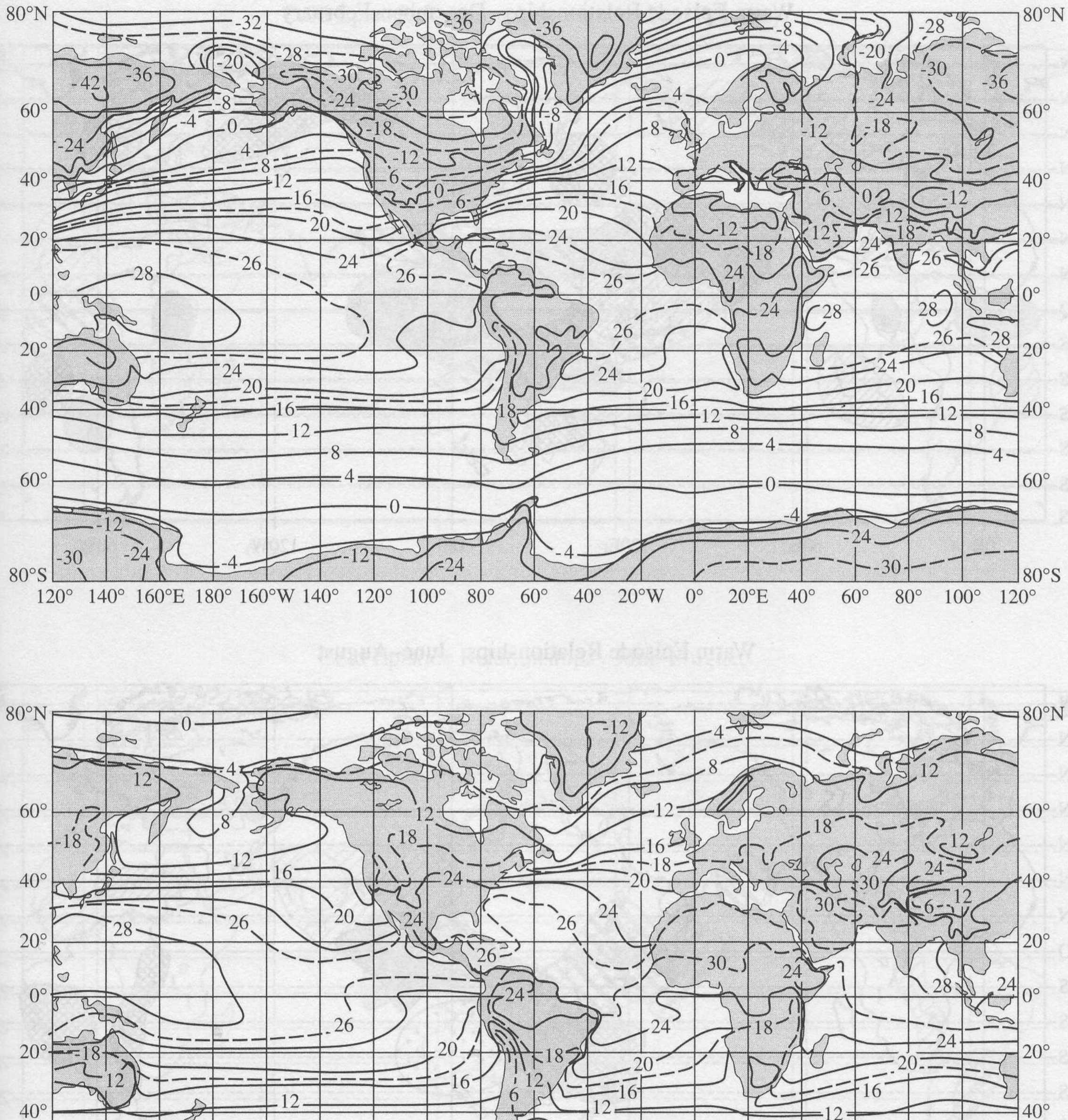

FIGURE 3-12
Distribution of mean temperature (°C) in (a) January; and (b) July. From *The Physics of Climate,* by J.P. Peixoto and by A.H. Oort © 1992, used with permission of American Institute of Physics.

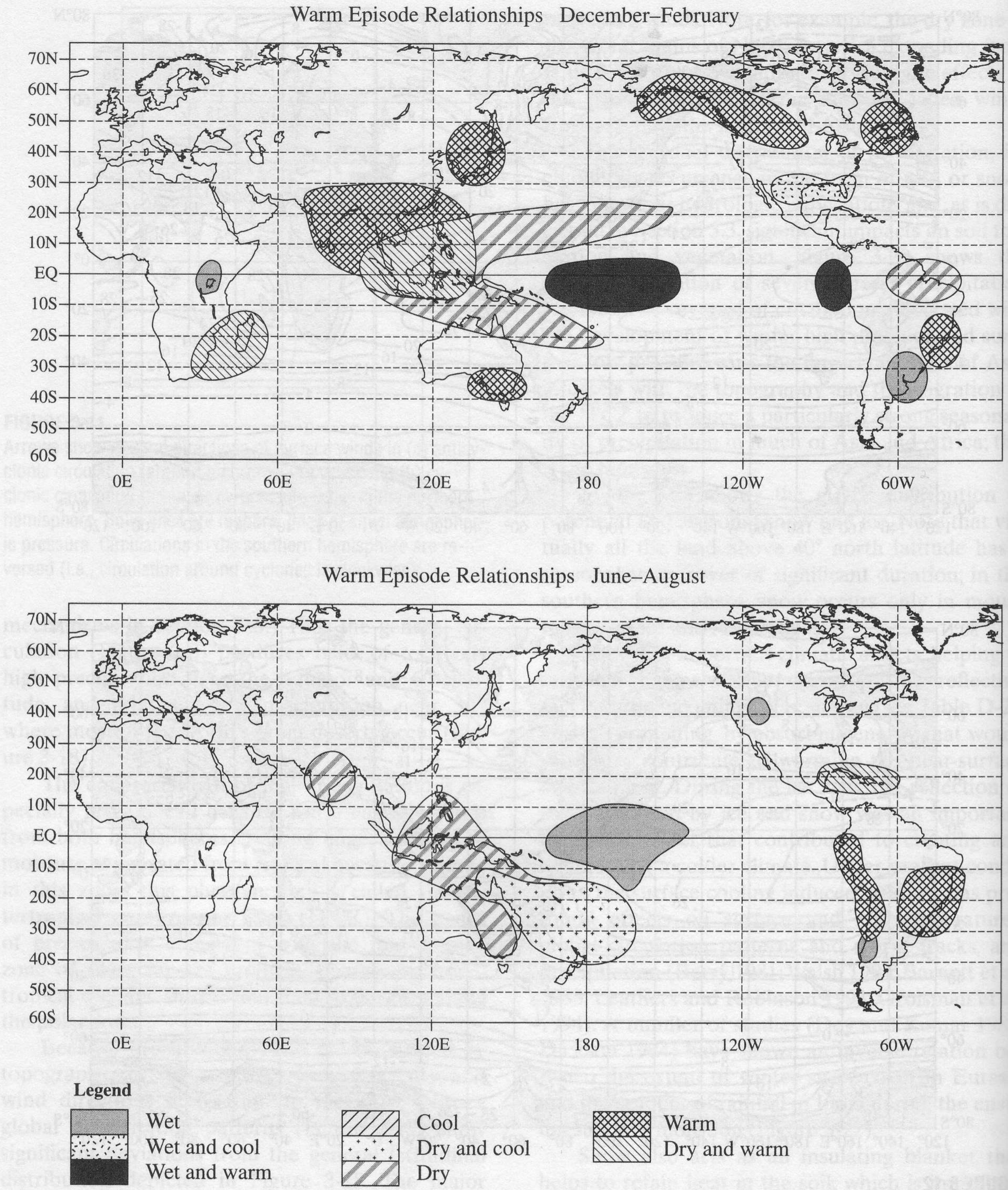

FIGURE 3-13
Typical climatic anomalies associated with the warm (El Niño) phase of ENSO. (a) winter (December–February); (b) summer (June–August). From U.S. National Atmospheric and Oceanographic Administration Climate Prediction Center website http://nic.fb4.noaa.gov/products/analysis_mon (1998).

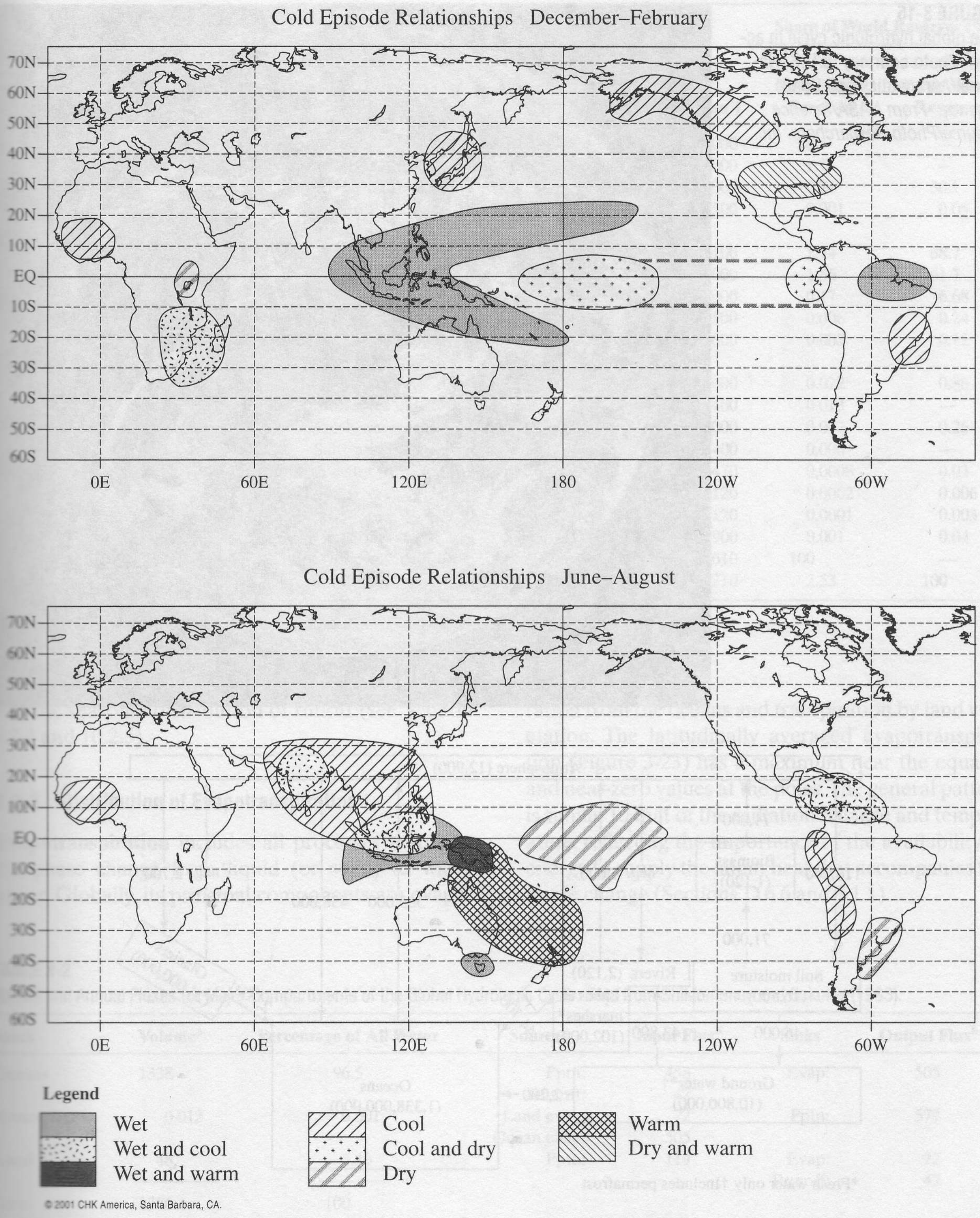

FIGURE 3-14
Typical climatic anomalies associated with the cold (La Niña) phase of ENSO. (a) winter (December–February); (b) summer (June–August). From U.S. National Atmospheric and Oceanographic Administration Climate Prediction Center website http://nic.fb4.noaa.gov/products/analysis_mon (1998).

FIGURE 3-15
The global hydrologic cycle in action. Photo courtesy of U.S. National Aeronautics and Space Agency. *From NASA/Science Source/Photo Researchers. Inc.*

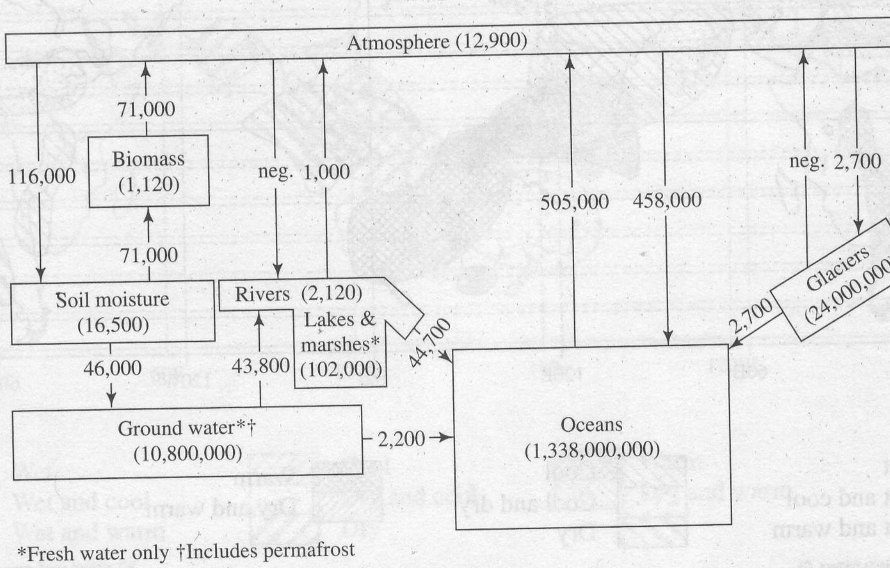

FIGURE 3-16
Schematic diagram of stocks and annual fluxes in the global hydrologic cycle. Based on data of Shiklomanov and Sokolov (1983) (Table 3-1). Inflows and outflows may not balance for all compartments due to rounding.

TABLE 3-1
Stocks in the Global Hydrologic Cycle.[a]

Form of Water	Area Covered (km²)	Volume (km³)	Share of World Reserves (%): Of Total Water Reserves	Share of World Reserves (%): Of Fresh-Water Reserves
World oceans	361,300,000	1,338,000,000	96.5	—
Ground waters	134,800,000	23,400,000	1.7	—
Fresh ground water		10,530,000	0.76	30.1
Soil moisture	82,000,000	16,500	0.001	0.05
Glaciers and permanent snowpack:	16,227,500	24,064,100	1.74	68.7
Antarctica	13,980,000	21,600,000	1.56	61.7
Greenland	1,802,400	2,340,000	0.17	6.68
Arctic islands	226,100	83,500	0.006	0.24
Mountain areas	224,000	40,600	0.003	0.12
Ground ice in zone of permafrost strata	21,000,000	300,000	0.022	0.86
Water reserves in lakes:	2,058,700	176,400	0.013	—
Fresh-water lakes	1,236,400	91,000	0.007	0.26
Saltwater lakes	822,300	85,400	0.006	—
Marsh water	2,682,600	11,470	0.0008	0.03
Water in rivers	148,800,000	2,120	0.0002	0.006
Biologic water	510,000,000	1,120	0.0001	0.003
Atmospheric water	510,000,000	12,900	0.001	0.04
Total water reserves	510,000,000	1,385,984,610	100	—
Fresh water	148,800,000	35,029,210	2.53	100

[a]Illustrated in Figure 3-16, page 54.
Data from Shiklomanov and Sokolov (1983).

affect the seasonal distribution of runoff (see Section 3.2.4 and 10.2.5).

3.2.3 Distribution of Evapotranspiration

Evapotranspiration includes all processes involving the phase change from liquid (or solid) to water vapor. Globally, its principal components are evaporation from the oceans and transpiration by land vegetation. The latitudinally averaged evapotranspiration (Figure 3-23) has a maximum near the equator and near-zero values at the poles. The general pattern is similar to that of the radiation balance and temperature, reflecting the importance of the availability of energy to supply the latent heat that accompanies the phase change (Sections D.6.6 and 7.1.1).

TABLE 3-2
Stocks and Annual Fluxes for Major Compartments of the Global Hydrologic Cycle. Data from Shiklomanov and Sokolov (1983).

Stock	Volume[a]	Percentage of All Water	Sources	Input Flux[b]	Sinks	Output Flux[b]
Oceans	1338	96.5	Pptn:	458	Evap:	505
			Runoff:	47		
Atmosphere	0.013	0.001	Land evap:	72	Pptn:	577
			Ocean evap:	505		
Land	48	3.46	Pptn:	119	Evap:	72
					Runoff:	47
Total	1386	100				

[a]Stocks in 10^6 km³.
[b]Fluxes in 10^3 km³ yr^{-1}.
Data from Shiklomanov and Sokolov (1983).

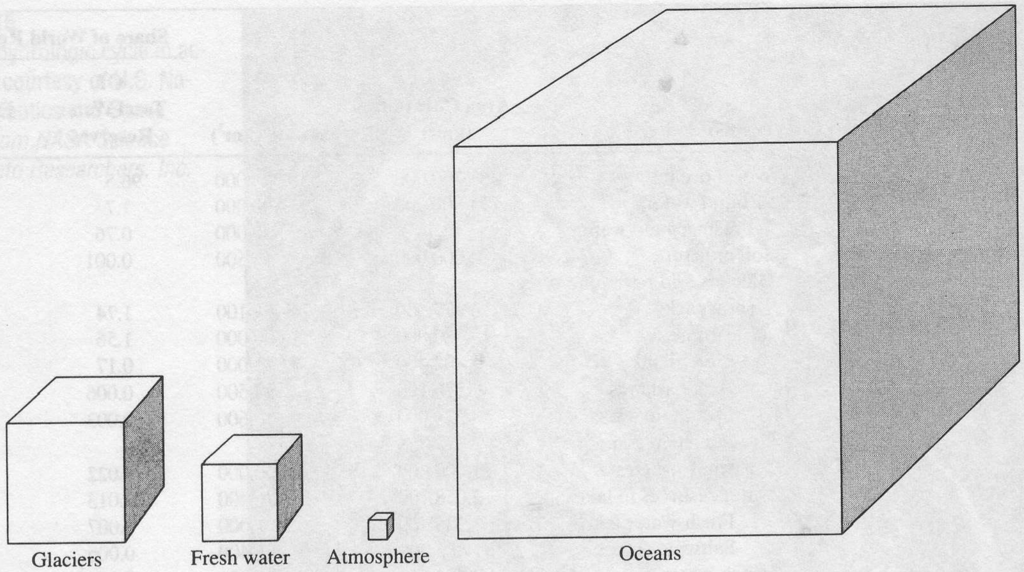

FIGURE 3-17
Relative volumes of water in oceans, glaciers, fresh water, and atmosphere.

FIGURE 3-18
Latitudinal distribution of average precipitation rate. From Barry and Chorley (1982).

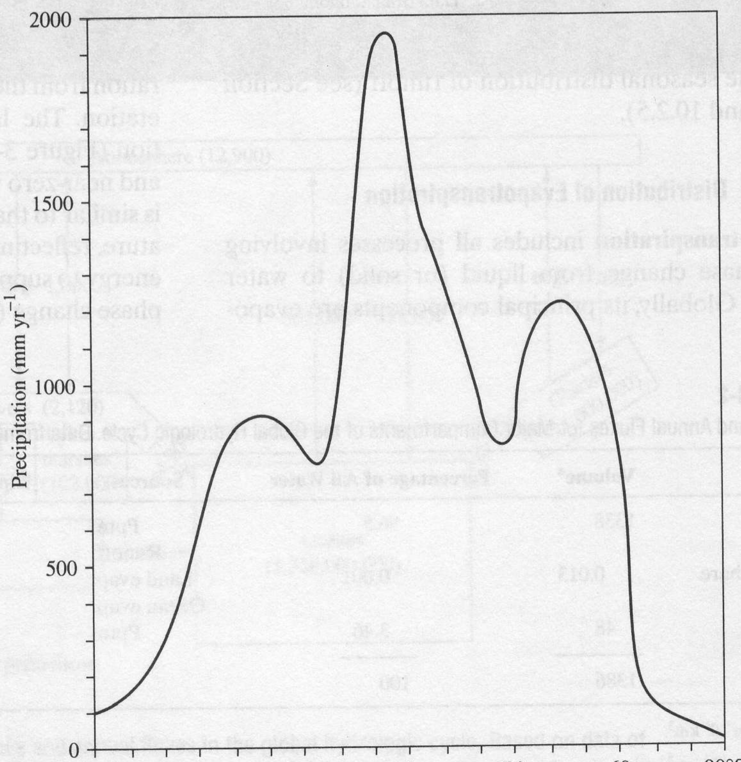

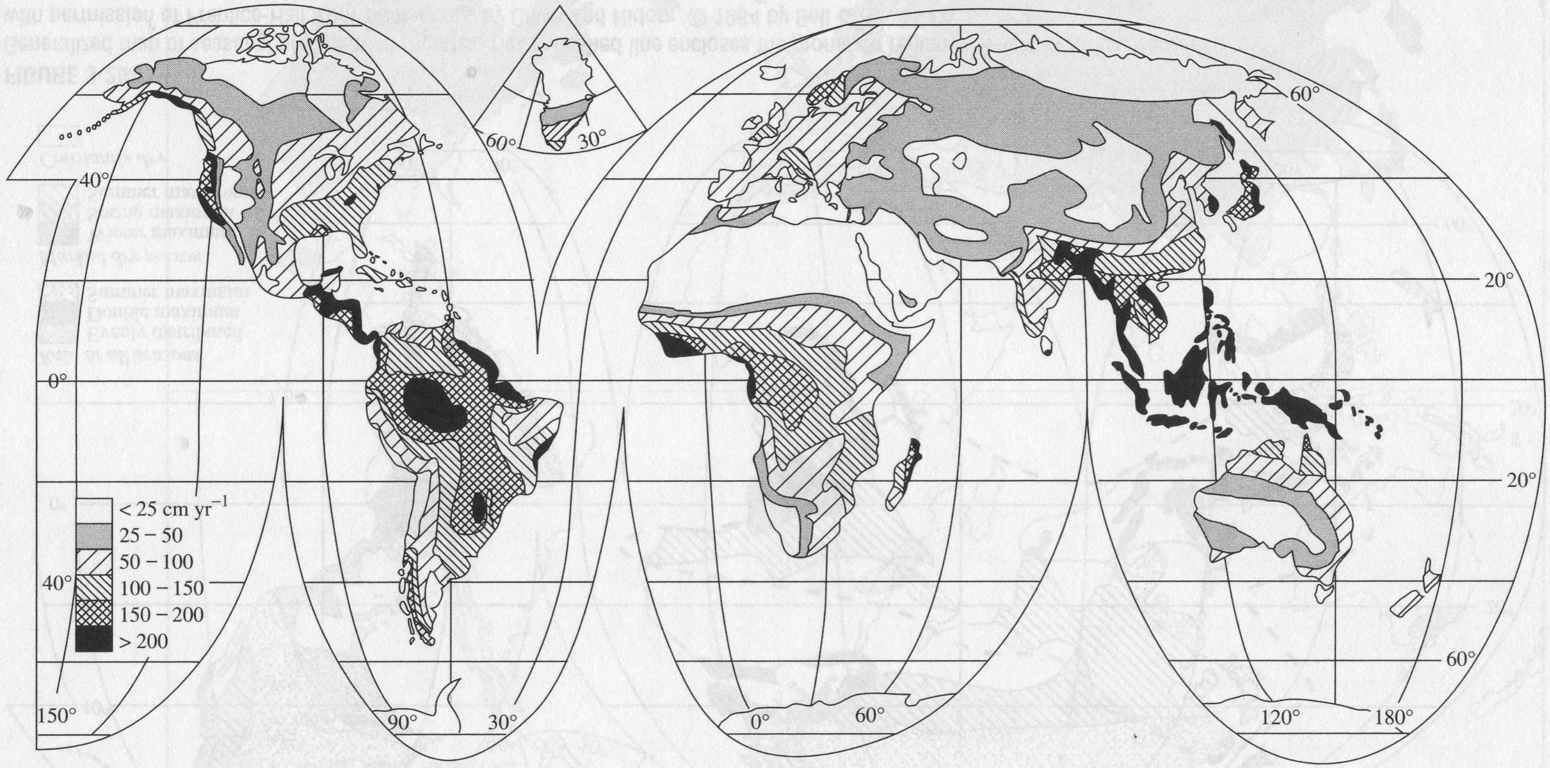

FIGURE 3-19
Average precipitation rate over the globe. Reprinted with permission of Prentice-Hall from *Climatology* by Oliver and Hidore, © 1984 by Bell & Howell Co.

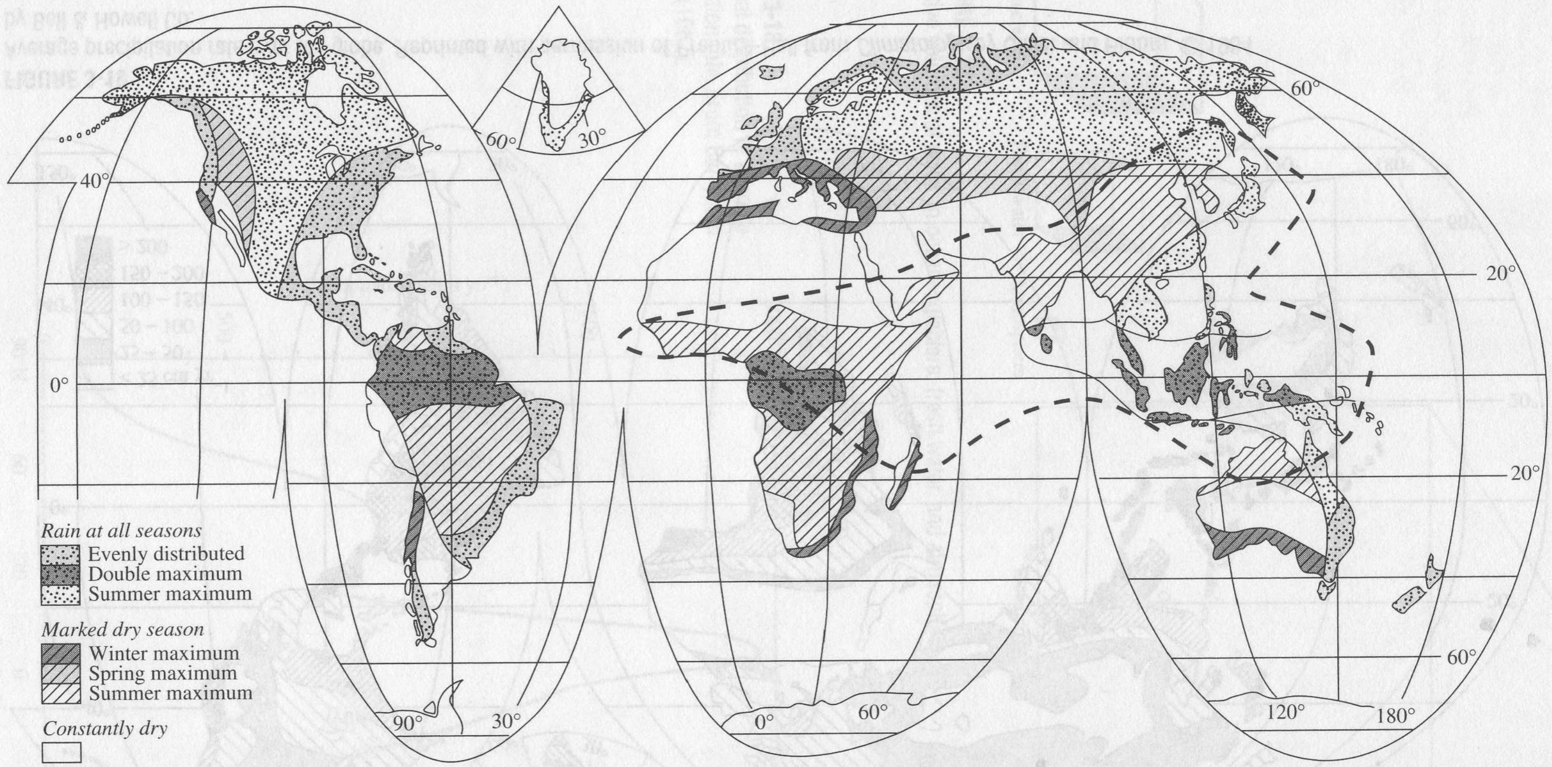

FIGURE 3-20
Generalized map of seasonal precipitation regimes. Heavy dashed line encloses the monsoon region of Asia and Africa. Reprinted with permission of Prentice-Hall from *Climatology* by Oliver and Hidore, © 1984 by Bell & Howell Co.

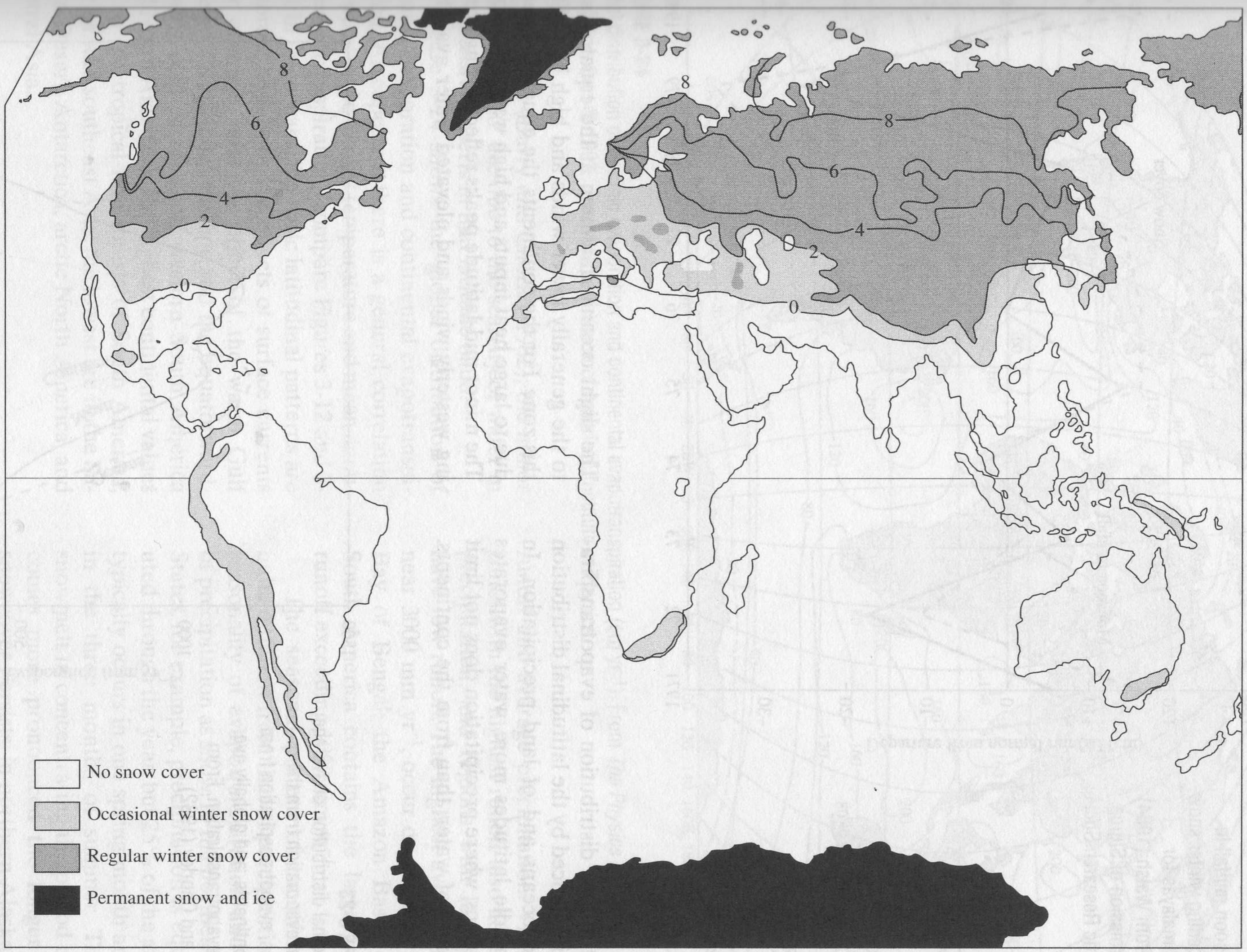

FIGURE 3-21
Global distribution of snow cover. Numbered lines indicate normal duration of seasonal snow cover in months. From Walsh (1984), used with permission of Sigma Xi, the Scientific Research Society.

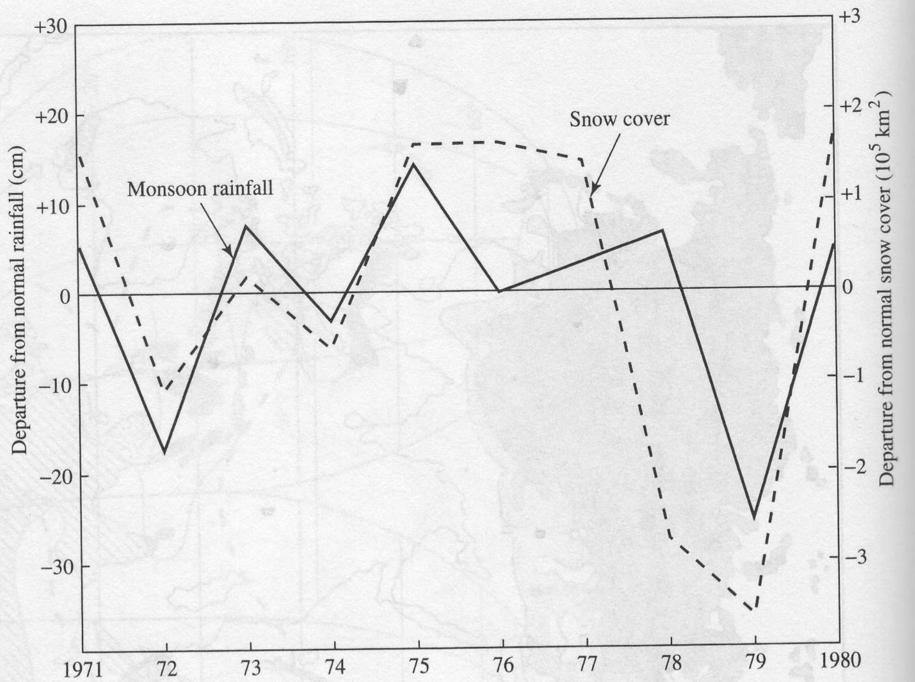

FIGURE 3-22
Summer monsoon rainfall in India and preceding winter snow-cover in the Himalayas for 1971–1980. From Walsh (1984) used with permission of Sigma Xi, the Scientific Research Society.

The latitudinal distribution of evapotranspiration is also influenced by the latitudinal distribution of land and oceans and of land precipitation. In lower to middle latitudes more water evaporates from the oceans, where precipitation does not limit the availability of water, than from the continents. The slight oceanic minimum at the equator is due to the generally lower winds and high humidity in this zone. For the continents, the equatorial peak is due to large heat inputs and high water availability. The minor mid-latitude peaks reflect strong prevailing westerly winds and elevated water availability

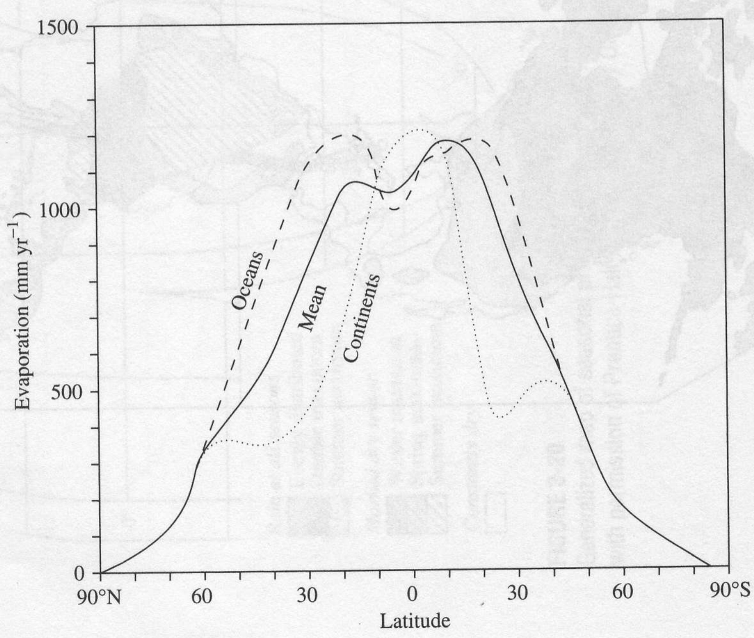

FIGURE 3-23
Latitudinal distribution of average annual evaporation from the oceans, evapotranspiration from the continents, and globally averaged evapotranspiration. From Barry and Chorley (1982).

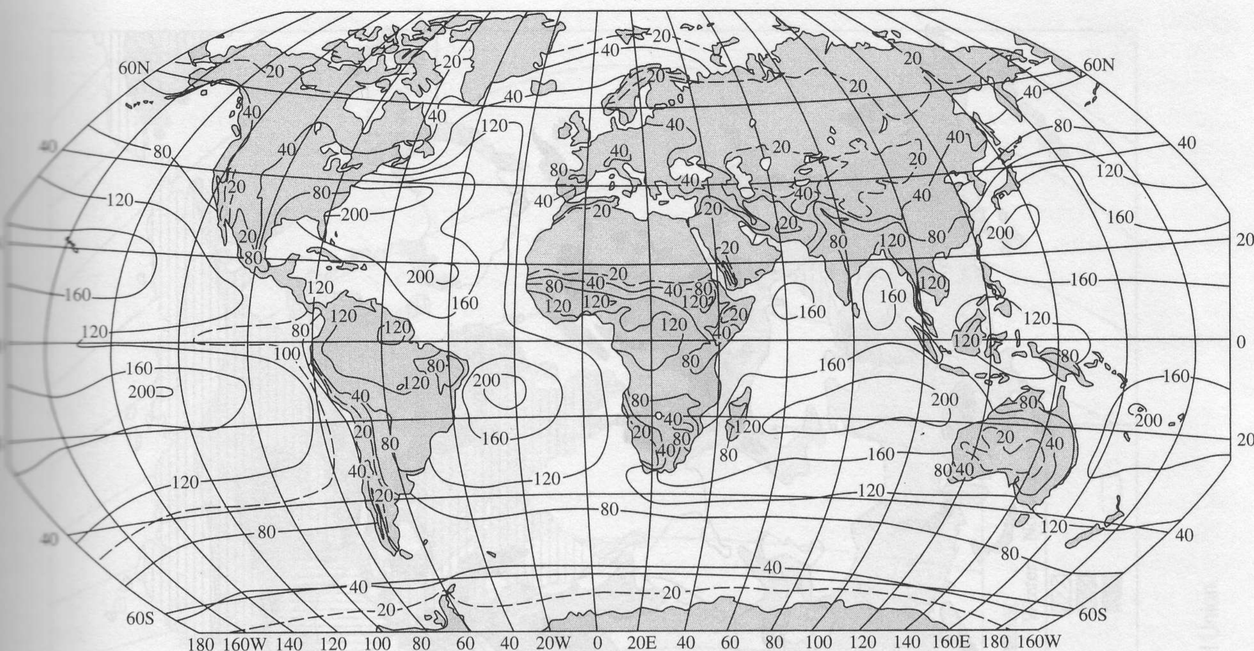

FIGURE 3-24
Global distribution of oceanic evaporation and continental evapotranspiration (cm yr^{-1}). From *The Physics of Climate*, by J.P. Peixoto and A.H. Oort © 1992, used with permission of American Institute of Physics.

(Figure 3-18) (Barry and Chorley 1982); the minor minima near 30° are due to the scarcity of water in the extensive deserts in that latitude band.

Figure 3-24 shows the global distribution of oceanic evaporation and continental evapotranspiration. As expected, there is a general correlation between mean annual temperature and mean annual evapotranspiration (compare Figures 3-12 and 3-24.) In the oceans, the basic latitudinal patterns are distorted largely by the effects of surface currents (for example, note the effect of the warm Gulf Stream off northern Europe and the equatorward-flowing cold currents off western South America and North America). The highest continental values are in the tropical rain forests of South America, Africa, and southeast Asia; the lowest are in the Sahara Desert, Antarctica, arctic North America, and central Asia.

3.2.4 Distribution of Runoff

Figure 3-25 shows the global distribution of annual runoff (i.e., the difference between precipitation and evapotranspiration) for the continents. Not surprisingly, comparison of Figures 3-19 and 3-25 shows a close correspondence between average runoff and average precipitation: Virtually all the zones with the highest runoff also have the highest precipitation, and regions with low precipitation have low runoff. The highest average runoff rates, near 3000 mm yr^{-1}, occur on the east coast of the Bay of Bengal; the Amazon Basin of northern South America contains the largest region with runoff exceeding 1000 mm yr^{-1}.

The seasonal pattern of runoff is commonly quite different from that of precipitation due to the seasonality of evapotranspiration and the storage of precipitation as snow. In the northeastern United States, for example, precipitation is equally distributed through the year, but 25% of the annual runoff typically occurs in one spring month and only 10% in the three months of summer. The effect of snowmelt in concentrating the period of runoff becomes more pronounced the longer the annual snowcover persists; in northern Alaska, one-half of the annual runoff occurs in a three- to ten-day period (Dingman et al. 1980).

Figure 3-26 shows the types of runoff regimes classified by L'vovich (1974). In this classification, regimes are identified by (1) the season in which the most runoff occurs (spring, summer, winter, fall) and (2) the degree to which runoff is concentrated

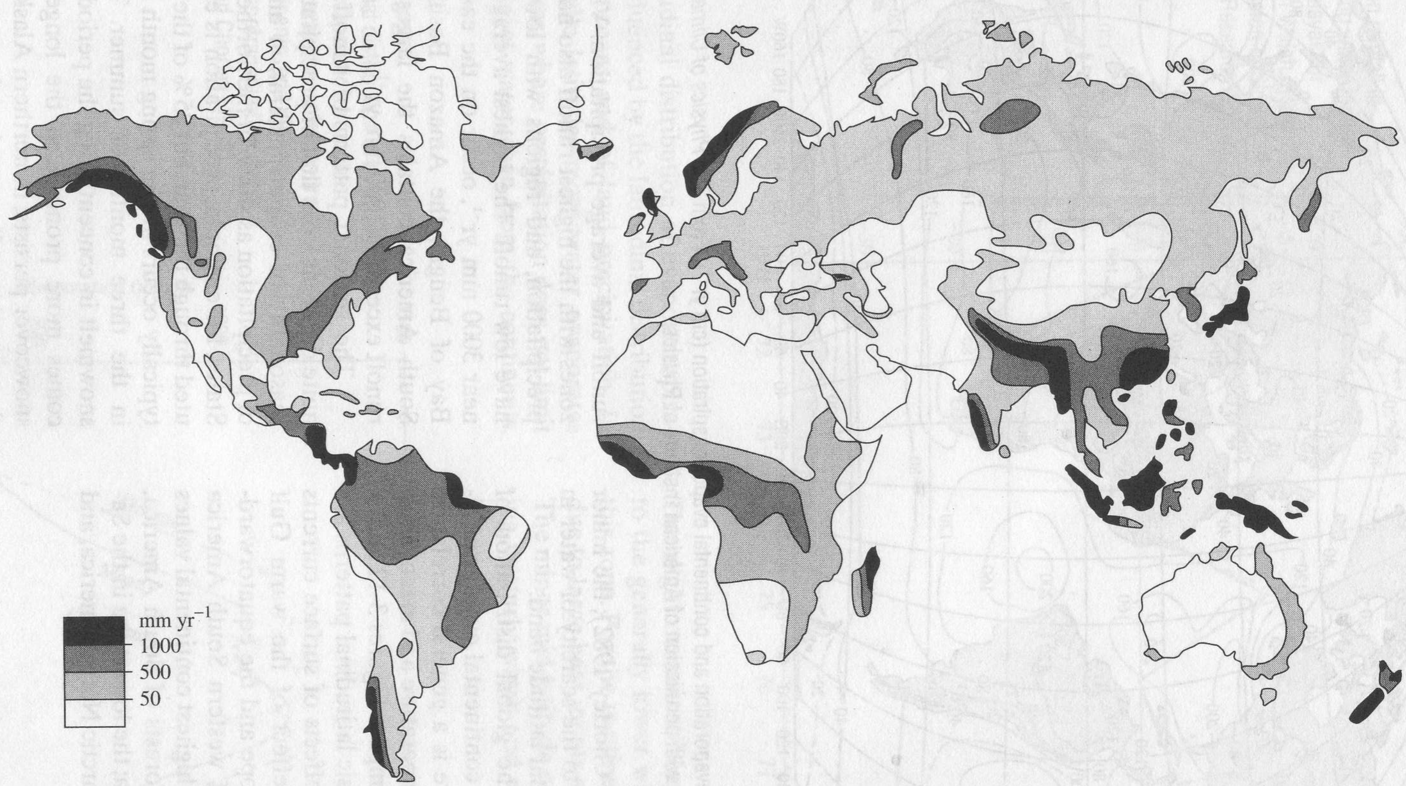

FIGURE 3-25
Global distribution of average runoff rate. From Gregory and Walling (1973).

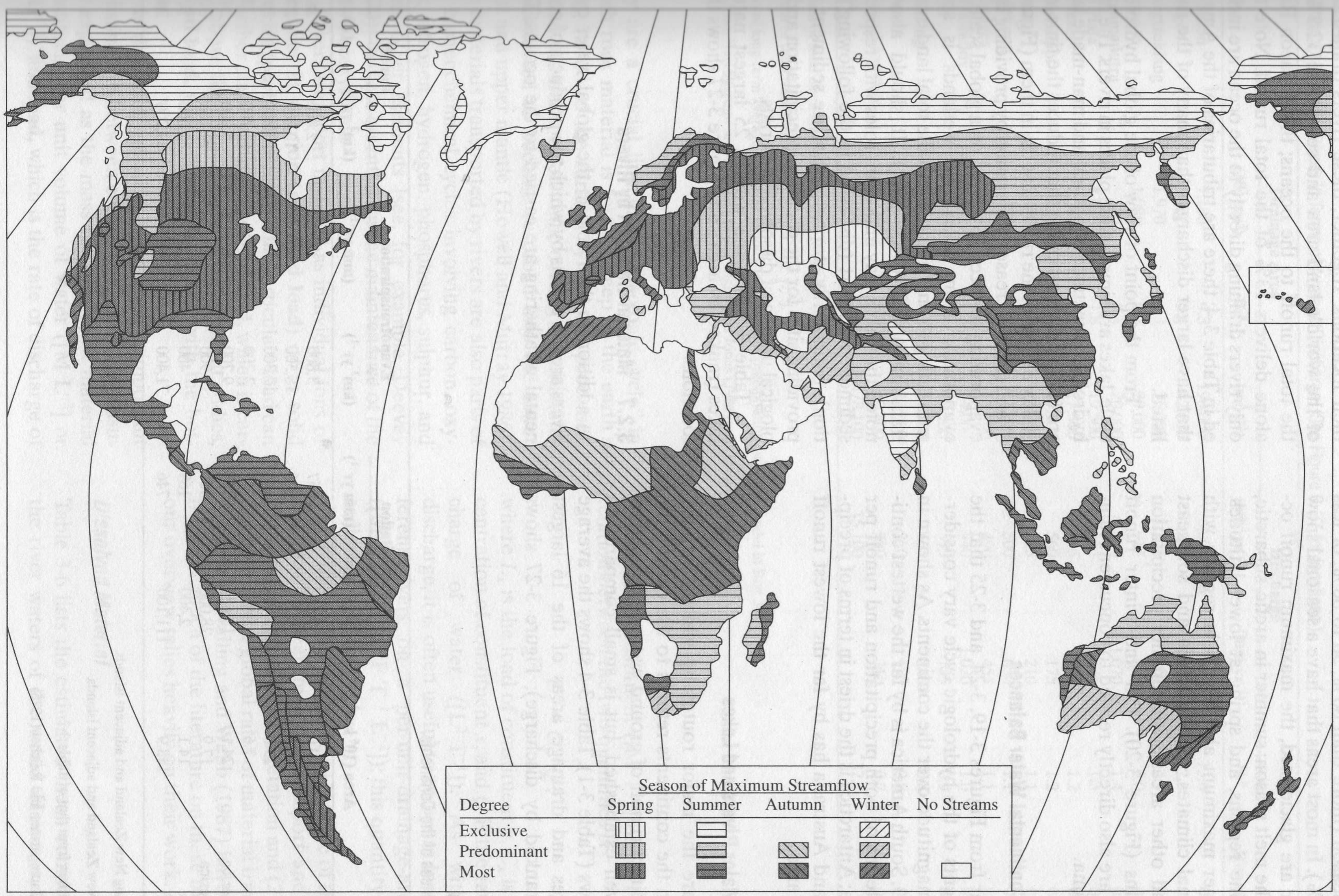

FIGURE 3-26
Seasonal runoff regimes. Modified from L'vovich (1974); used with permission of the American Geophysical Union.

in that season (more than 80%, 50 to 80%, or less than 50%). In most areas that have a seasonal snow cover or are glacierized, the maximum runoff occurs in the melt season: summer in arctic, subarctic, and alpine regions, and spring at lower latitudes. A summer maximum also occurs in regions with monsoonal climates, such as India and southeast Asia, and other areas with summer precipitation maximums (Figure 3-20). Fall and winter runoff maxima are also directly related to concurrent rainfall maxima.

3.2.5 Continental Water Balances

It is clear from Figures 3-19, 3-24, and 3-25 that the components of the hydrologic cycle vary considerably in magnitude over the continents. As shown in Table 3-3, South America is by far the wettest continent in terms of both precipitation and runoff per unit area; Antarctica is the driest in terms of precipitation, and Australia has by far the lowest runoff per unit area.

3.2.6 Major Rivers and Lakes

Rivers are the major routes by which "surplus" water on the continents returns to the oceans; the rate of direct runoff of ground water to the oceans is not well established, but is small compared to river flows (Table 3-1). Table 3-4 shows the average discharges and drainage areas of the 16 largest rivers (ranked by discharge); Figure 3-27 shows their locations. Together, these rivers drain 22.9% of the world's land area and contribute 32.8% of the total runoff to the oceans; the Amazon River alone delivers 13% of the total runoff. Note that only rivers draining directly to the ocean are included in Table 3-4; there are tributaries of the Amazon that have larger discharges than many of the rivers listed.

From the point of view of the global hydrologic cycle, lakes are simply wide places in rivers. The main hydrologic functions of natural and man-made lakes are (1) to provide storage that reduces the time variability of flow in the rivers that drain them (Figure 2-8) and (2) to increase evaporation by providing large evaporating surfaces. However, on a global scale, the evaporation from lakes and wetlands is small, amounting to only about 3% of the total land evapotranspiration (L'vovich 1974). It should also be noted that lakes play important roles with respect to sediment transport (discussed in the following section), temporarily storing particulate sediment and providing sites for the chemical precipitation and biological uptake of dissolved materials.

Table 3-5 lists the world's 25 largest natural lakes (ranked by area), and Figure 3-27 shows their locations.

3.2.7 Material Transport by Rivers

In addition to their role in the global water cycle, rivers are the means by which the products of continental weathering are carried to the oceans. Thus

TABLE 3-3
Water Balances of the Continents.

Continent	Area (10^6 km^2)	Precipitation ($km^3\ yr^{-1}$)	Precipitation ($mm\ yr^{-1}$)	Evapotranspiration ($km^3\ yr^{-1}$)	Evapotranspiration ($mm\ yr^{-1}$)	Runoff ($km^3\ yr^{-1}$)	Runoff ($mm\ yr^{-1}$)
Europe	10.0	6,600	657	3,800	375	2,800	282
Asia	44.1	30,700	696	18,500	420	12,200	276
Africa	29.8	20,700	695	17,300	582	3,400	114
Australia[a]	7.6	3,400	447	3,200	420	200	27
North America	24.1	15,600	645	9,700	403	5,900	242
South America	17.9	28,000	1,564	16,900	946	11,100	618
Antarctica	14.1	2,400	169	400	28	2,000	141
Total land[b]	148.9	111,100[c]	746	71,400	480	39,700[c]	266

[a]Not including New Zealand and adjacent islands.

[b]Including New Zealand and adjacent islands.

[c]Estimate differs from that of Table 3-2.

Data from Baumgartner and Reichel (1975)

TABLE 3-4
The World's 16 Largest Rivers in Terms of Average Discharge. (See Figure 3-27 for locations.)

River	Drainage Area (10^3 km^2)	%[a]	Discharge ($m^3 s^{-1}$)	($km^3 yr^{-1}$)	($mm yr^{-1}$)	%[b]	Runoff Ratio[c]
1. Amazon	7,180	4.8	190,000	6,000	835	13.0	0.47
2. Congo	3,822	2.6	42,000	1,330	340	2.9	0.25
3. Yangtzekiang	1,970	1.3	35,000	1,100	560	2.4	0.50
4. Orinoco	1,086	0.7	29,000	915	845	2.0	0.46
5. Brahmaputra	589	0.4	20,000	630	1,070	1.4	0.65
6. La Plata	2,650	1.8	19,500	615	235	1.3	0.20
7. Yenesei	2,599	1.7	17,800	565	215	1.2	0.42
8. Mississippi	3,224	2.2	17,700	560	175	1.2	0.21
9. Lena	2,430	1.6	16,300	515	210	1.1	0.46
10. Mekong	795	0.8	15,900	500	630	1.1	0.43
11. Ganges	1,073	0.7	15,500	490	455	1.1	0.42
12. Irrawaddy	431	0.3	14,000	440	1,020	1.0	0.60
13. Ob	2,950	2.0	12,500	395	135	0.9	0.24
14. Sikiang	435	0.3	11,500	365	840	0.8	—
15. Amur	1,843	1.2	11,000	350	190	0.8	0.32
16. Saint Lawrence	1,030	0.7	10,400	330	310	0.7	0.33
Totals	34,107	22.9	478,100	15,100		32.8	

[a]Percent of total earth land area (148.9×10^6 km^2).

[b]Percent of total runoff to oceans (46×10^3 km^3 yr^{-1}).

[c]Ratio of long-term average discharge to long-term average precipitation (w in the model in Box 3-4).

Data from Baumgartner and Reichel (1975), Wigley and Jones (1985), and L'vovich (1974).

they are a crucial link in the "tectonic cycle" in which rock material is formed deep in the earth's crust, raised to the surface by tectonic processes, eroded and transported to the oceans, and ultimately subducted to become resorbed into the lower crust and upper mantle (Howell and Murray 1986). The materials transported by rivers are also parts of the biogeochemical cycles involving carbon, oxygen, nitrogen, hydrogen, phosphorus, sulphur, and many other elements [see, for example, Deevey (1970)] that are essential for the maintenance of the earth's ecosystems.

Rivers transport material as individual ions or molecules in solution (**dissolved load**) or as solid particles (**particulate load**). The particulate load can be further classified as **suspended load,** which is carried above the channel bottom by turbulent eddies, or **bed load,** which moves in contact with the bottom.

In discussing material transport, it is important to distinguish between **concentration,** which is usually expressed as the mass (or weight) of material constituent per unit volume of water ([M L^{-3}] or [F L^{-3}]), and **load,** which is the rate of discharge of the material constituent ([M T^{-1}] or [F T^{-1}]). The relation between the two quantities is

$$L_x = C_x \cdot Q, \qquad (3\text{-}1)$$

where L_x is the load of constituent x, C_x is the concentration of constituent x, and Q is the rate of discharge of water ([L^3 T^{-1}]). As with water discharge, it is often useful to compare loads in different rivers on a per-unit-drainage-area basis ([M T^{-1} L^{-2}] or [F T^{-1} L^{-2}]); this quantity is called **sediment yield.**

In this section, we review (1) some of the global relations between material transport and climate, geology, topography, and vegetation and (2) current estimates of the global rates of material transport to the oceans. Walling and Webb (1987) have recently reviewed much of the literature on these topics, and our overview relies heavily on their work.

Dissolved Material

Table 3-6 lists the estimated mean composition of the river waters of the world. However, composi-

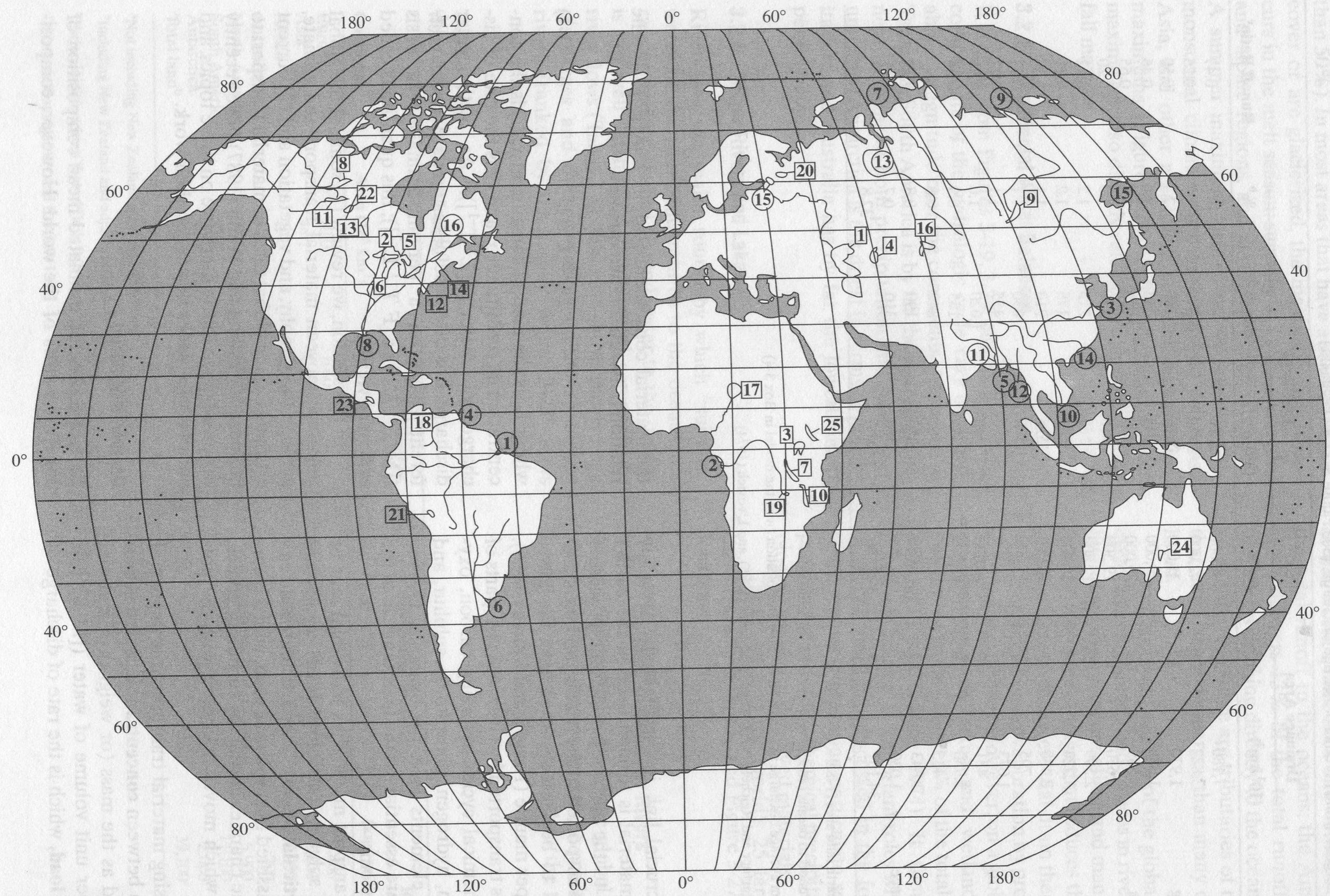

FIGURE 3-27
Locations of the world's 16 largest rivers shown by numbers in circles; refer to Table 3-4. Locations of the world's 25 largest lakes shown by numbers in squares; refer to Table 3-5.

TABLE 3-5
The World's 25 Largest Natural Lakes in Terms of Surface Area. (See Figure 3-27 for locations.)

Lake	Area (km^2)	Maximum Depth (m)	Elevation (m)
1. Caspian Sea	371,800	995	–28
2. Superior	82,400	406	183
3. Victoria	69,500	81	1,134
4. Aral Sea[a]	65,500	68	53
5. Huron	59,600	229	177
6. Michigan	58,000	281	177
7. Tanganyika	32,900	1,436	773
8. Great Bear	31,800	413	156
9. Baikal	30,500	1,620	455
10. Nyasa	29,600	679	473
11. Great Slave	28,400	614	156
12. Erie	25,700	64	174
13. Winnipeg	24,500	18	217
14. Ontario	19,700	245	75
15. Ladoga	17,700	225	4
16. Balkhash[b]	17,400	26	340
17. Chad[b]	16,300	7	240
18. Maracaibo	13,300	35	0
19. Bangwelu	9,800	?	1,150
20. Onega	9,600	110	33
21. Titicaca	8,300	281	3,813
22. Athabasca	8,100	124	213
23. Nicaragua	8,000	70	32
24. Eyre[b]	7,700	1	–16
25. Rudolf	6,400	61	375

[a] The Aral Sea has been much reduced in size by disastrous water-resource developments (Micklin 1988).

[b] Area varies significantly in response to seasonal and longer-term precipitation fluctuations. Data mostly from Todd (1970).

tion varies widely in different regions of the world, largely because of variations in rock type and climate. Gibbs (1970) showed that rivers draining areas with high annual precipitation and runoff tend to have low total dissolved concentrations and compositions similar to that of the precipitation (i.e., they are relatively rich in sodium [Na] and chlorine [Cl]) and largely independent of rock type (Figure 3-28). In climates with moderate precipitation and runoff, concentrations are at moderate levels and composition is dominated by rock type and tends to be high in calcium (Ca) and bicarbonate (HCO_3). As one moves toward drier climates, water chemistry becomes increasingly controlled by fractional crystallization due to evaporation: Concentrations increase, and the composition shifts from Ca–HCO_3 toward Na–Cl. The ultimate end-member in this progression is sea water.

Walling and Webb (1987) examined data for some 500 rivers worldwide and found average dissolved-sediment yields ranging from less than 1 T km^{-2} yr^{-1} to 750 T km^{-2} yr^{-1}; the average was about 40 T km^{-2} yr^{-1}. Figure 3-29 shows the global variation of total dissolved load for major river basins. (Data are sparse for other areas.) The high loads in southern Asia reflect the high discharges in those regions (Figure 3-26); those in central Europe are

TABLE 3-6
Mean Composition of River Water of the World.

Constituent	Concentration (mg/L)
Silica (SiO_2)	10.4
Calcium (Ca)	13.4
Magnesium (Mg)	3.35
Sodium (Na)	5.15
Potassium (K)	1.3
Bicarbonate (HCO_3)	52
Sulfate (SO_4)	8.25
Chloride (Cl)	5.75
Total dissolved solids	73.2

Data from Hem (1985).

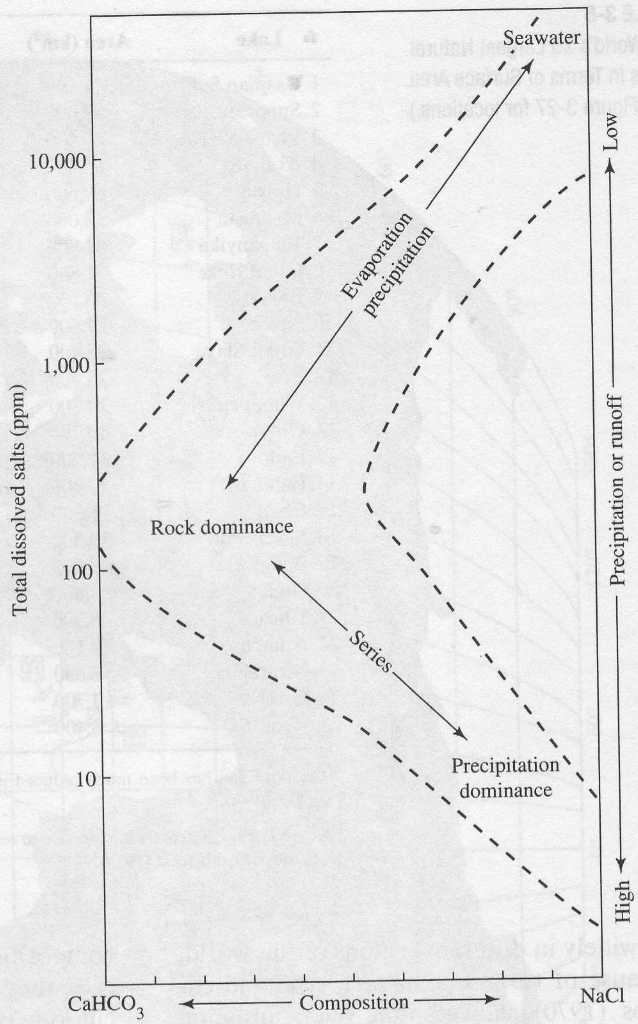

FIGURE 3-28
Processes controlling the chemistry of world rivers, according to Gibbs (1970).

due to widespread soluble rocks, especially limestones. The very high loads of the Irrawaddy River in Southeast Asia and those on New Guinea are produced by a combination of readily weathered rocks, high rates of weathering due to high temperatures and precipitation, and high discharges. The presence of crystalline rocks with low solubilities in much of Africa and Australia gives rise to generally low dissolved loads on those continents.

Particulate Material

The natural rate of erosion of particulate material is determined by climate, rock type, topography, tectonic activity, and vegetation. However, it appears that human activity has doubled global sediment transport in historic times (Milliman and Syvitski 1992). Thus all these factors, plus the effects of lakes and reservoirs acting as sediment traps (also greatly increased by humans; see Vörösmarty et al. 1993), affect the global patterns of particulate-sediment yield and make it difficult to generalize about these patterns. However, Dedkov and Mozzherin (1984) have related sediment yields to vegetation, after first classifying rivers with respect to topography and size (Figure 3-30). These vegetative zones can be generally related to climatic factors, as discussed in Section 3.3.2. Note that, outside of glacierized regions, the highest yields tend to occur in "Mediterranean" climates, where vegetation is sparse because annual rainfall is low, but the rain is concentrated in a few months of the year. In another global survey that included smaller streams, Milliman and Syvitski (1992)

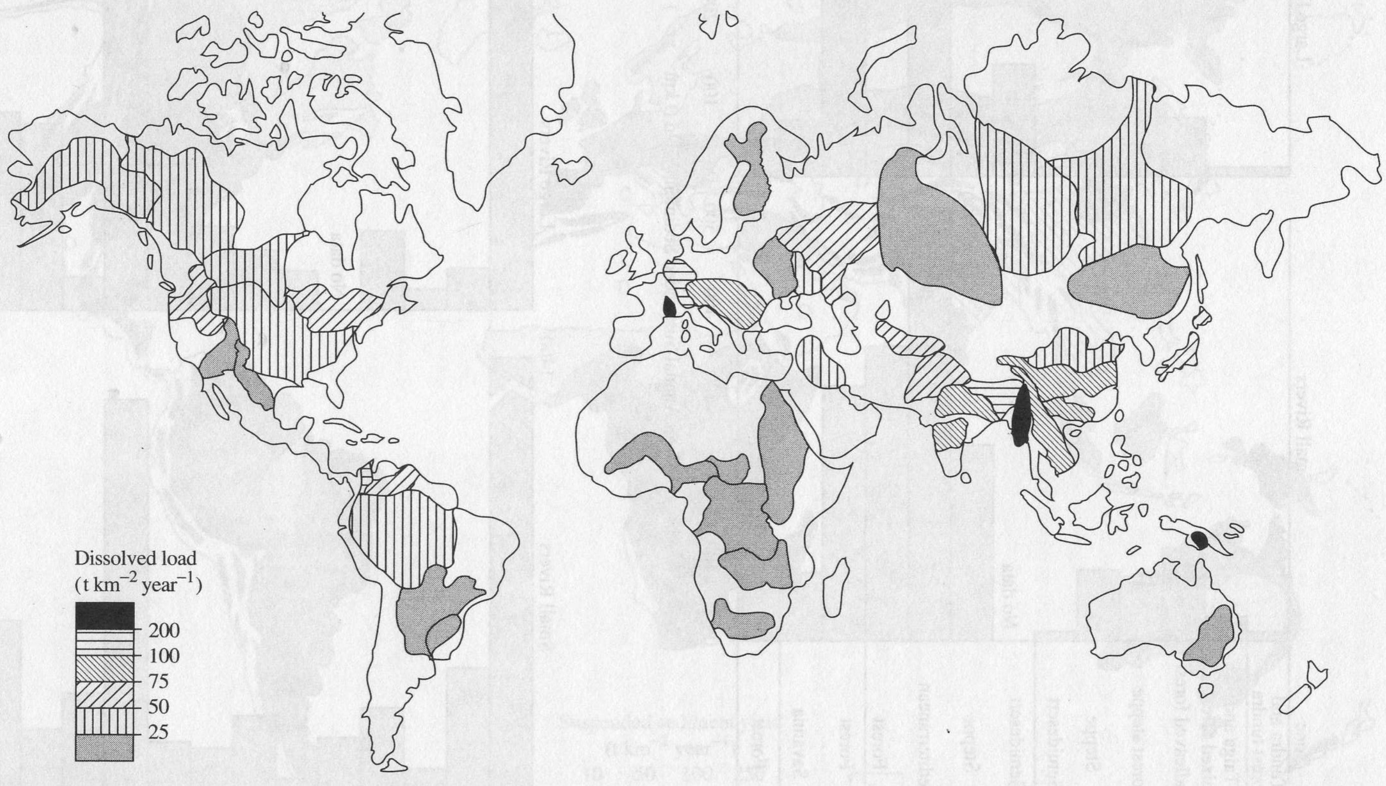

FIGURE 3-29
Dissolved-sediment yields in major river basins of the world. From Walling and Webb (1987).

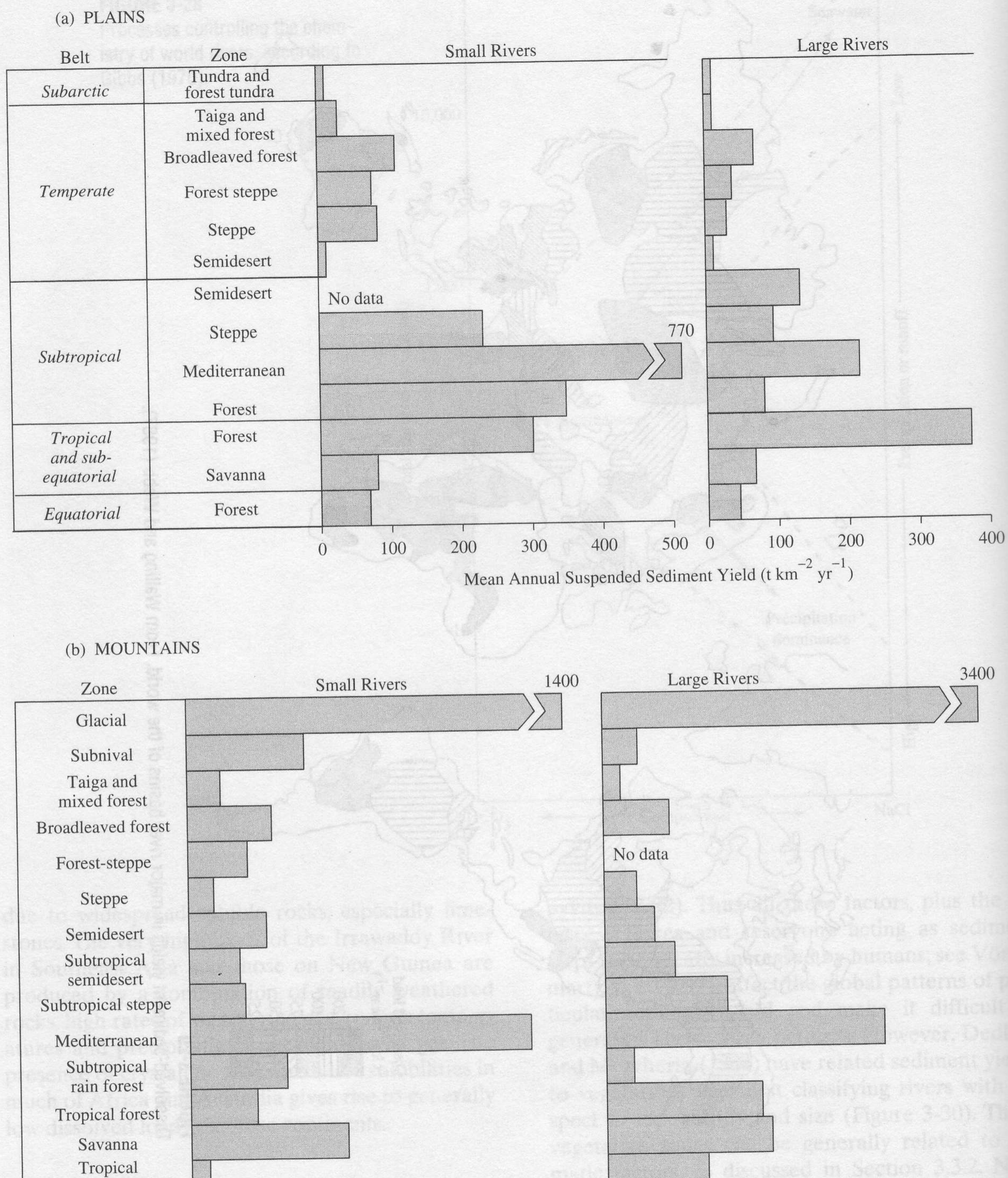

FIGURE 3-30
Relation between particulate-sediment yields and vegetation, as proposed by Dedkov and Mozzherin (1984). The boundary between "small" and "large" rivers is at a drainage area of 5000 km^2. From Walling and Webb (1987).

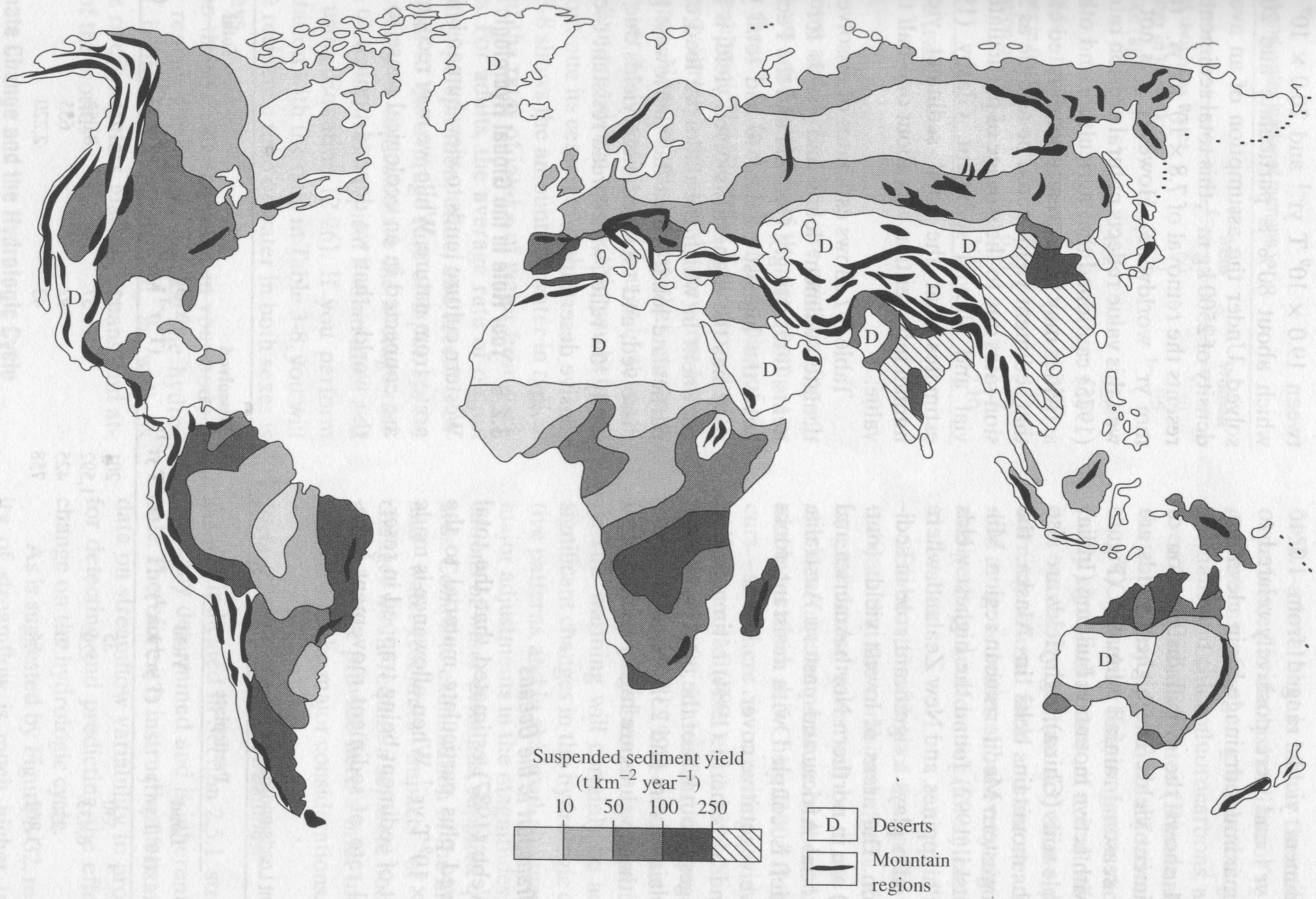

FIGURE 3-31
Global distribution of particulate-sediment yields, as mapped by Dedkov and Mozzherin (1984). From Walling and Webb (1987).

found that sediment yields ranged from 1.2 to 36,000 T km^{-2} yr^{-1} and were positively related to drainage area, maximum drainage-basin elevation, and runoff.

Figure 3-31 shows the global distribution of particulate-sediment yields. The highest yields are in areas with seasonal-rainfall climates (Figure 3-20) coupled with active mountain building (India) or highly erodible soils (China); high yields are also associated with mountain belts in Alaska, the Andes, and the western Mediterranean region. Milliman and Syvitski (1992) found the highest yields in Taiwan, the Philippines, and New Zealand, where human activity also plays a significant role in sediment production. The areas of lowest yields (outside of deserts) are in northern North America and Eurasia, equatorial Africa, and eastern Australia, where low relief is coupled with resistant rocks and/or extensive vegetative cover.

Dedkov and Mozzherin (1984) estimated that bed load averages about 8% of the total particulate load in large plains rivers and 23% in large mountain rivers, but these values are highly variable and uncertain.

Total Material Transport to the Oceans

Walling and Webb (1987) estimated that the total load of dissolved plus particulate material to the oceans is 17.2×10^9 T yr^{-1}. When allowance is made for the amount of sediment being trapped in reservoirs, the total rate of sediment movement is between 19.0×10^9 T yr^{-1} and 20.0×10^9 T yr^{-1}, of which about 80% is particulate and 20% is dissolved. Under the assumption of an average rock density of 2500 kg m^{-3}, this total sediment yield represents the removal of 7.8×10^9 m^3 yr^{-1} (about 0.05 mm yr^{-1} worldwide). However, it is not clear how well this value reflects natural erosion rates. Trimble (1975) cautioned that agriculture and other human activities may have greatly accelerated erosion, and that sediment yields could be as little as 5% of erosion rates due to the storage of particulates as colluvial and alluvial sediment. Glasby (1988) cited estimates that the total sediment yield before human intervention was about one-half the present value.

Table 3-7 shows estimates of dissolved and particulate sediment loads and yields for the continents. Interestingly, Oceania and the Pacific Islands have the highest particulate and total yields. Europe has the highest dissolved yield; it is the only continent in which the dissolved load exceeds the particulate load. Africa has the lowest particulate, dissolved, and total sediment yields due to its generally low relief, widespread resistant rocks, and extensive desert areas.

3.2.8 Your Role in the Global Hydrologic Cycle

Western culture tends to view human beings as separate from nature. While we may recognize that we are connected in an ecological sense to the rest of the world—that we depend upon it to supply the

TABLE 3-7
Estimated Sediment Loads and Yields by Continent.

	Particulate		Dissolved		Total	
Continent	Load (10^6 T yr^{-1})	Yield (T yr^{-1} km^{-2})	Load (10^6 T yr^{-1})	Yield (T yr^{-1} km^{-2})	Load (10^6 T yr^{-1})	Yield (T yr^{-1} km^{-2})
Africa	530	35	201	13	731	48
Asia	6,433	229	1,592	57	8,052	286
Europe	230	50	425	92	655	142
North and Central America	1,462	84	758	43	2,220	127
Oceania and Pacific Islands[a]	3,062	589	293	56	3,355	645
South America	1,788	100	603	34	2,391	134

[a] Includes Australia and the large Pacific Islands.

Data from Walling and Webb (1987).

TABLE 3-8
Water content and water intake of humans.

	Man	Woman
Percentage of weight as water	60	50
Weight of water in body (kg)	42	25
Average intake (kg day^{-1})		
in milk	0.30	0.20
in tap water	0.15	0.10
in other fluids	1.50	1.10
as free water in food	0.70	0.45
from oxidation of food	0.35	0.25
	3.00	2.10

Data from Harte (1985).

food, clothing, and shelter that are essential for our existence—we tend to think of the environment as being "out there." In fact, each of us is part of the great biogeochemical cycles that have moved matter and energy through the global ecosystem for billions of years. None of the atoms that currently constitute your body was part of you at birth; each atom has a finite residence time within you before it leaves to continue its ceaseless cycling.

Table 3-8 shows the amounts of water in typical humans and the rates of intake of water from various sources. For adults, the average rate of output (via breathing, perspiration, urine, and feces) is essentially equal to the average rate of input. As for other reservoirs, we can calculate the average residence time of water in the typical human male and female by using Equation (2-26). If you perform this computation with the data in Table 3-8, you will see that the residence time of water in both sexes is about 14 days.

Thus, on the average, the water in your body is completely replaced every two weeks. The hydrologic cycle is flowing through you, as well as through the rivers, aquifers, glaciers, oceans, and atmosphere of the world.

3.2.9 Climate Change and the Hydrologic Cycle

As is discussed in Section D.2.1, measurements show that atmospheric concentrations of carbon dioxide and other greenhouse gases have been increasing throughout this century. The concentration of carbon dioxide (CO_2) has increased from 280 parts per million (ppm) in 1850 to 353 ppm in 1990 and is projected to reach 500 ppm or higher by 2050—a level that is higher than any the earth has experienced in the last million or so years. The concentrations of other greenhouse gases, especially methane and chlorofluorocarbons, are increasing at even faster relative rates (Ramanathan 1988), and they are many times more effective (per molecule) than CO_2 at absorbing longwave radiation. It is virtually certain that most, if not all, of these increases are caused by human activities—particularly the burning of fossil fuels and the clearing of forests—and these activities show every sign of continuing, and perhaps accelerating, for at least the next several decades.

Elaborate models of the earth's climate system indicate that the combined effects of these increases in greenhouse gases will be a rise in the average earth-surface temperature of about 1 to 2 C° by 2050 and by as much as 5 C° by 2100.[9] If this warming occurs—and there is mounting evidence that it is under way (Mitchell et al. 1995; Santer et al. 1996; Tett et al. 1996; Harris and Chapman 1997; Kaufmann and Stern 1997)—the earth will become warmer than it has been at any time in human history. This warming will certainly be accompanied by significant changes in the hydrologic cycle, in vegetative patterns, and in sea level, changes that will force major adjustments in the magnitudes, timing, and locations of water demands, supplies, quality, and hazards. Complete examination of the likely hydrologic and water-resources impacts of these climate changes would require a separate book-length treatment, but we provide here a brief introduction and overview of the major considerations.

Historical Variability of Streamflow

As was indicated in Section 2.5.1, streamflow is climatically determined and is inherently highly variable. Therefore it is instructive to examine historical data on streamflow variability to provide a context for detecting and predicting the effects of climate change on the hydrologic cycle.

As is suggested by Figure 3-32, relative variability of streamflow is much higher in arid regions (Upper and Lower Plains, Southwest) than in humid regions (Northeast, Northwest). Interestingly, time

[9]These increases can be simulated via the model described in Box 3-2 by increasing *f*, the fraction of longwave energy emitted by the surface that is absorbed in the atmosphere. (See Exercise 3-3.)

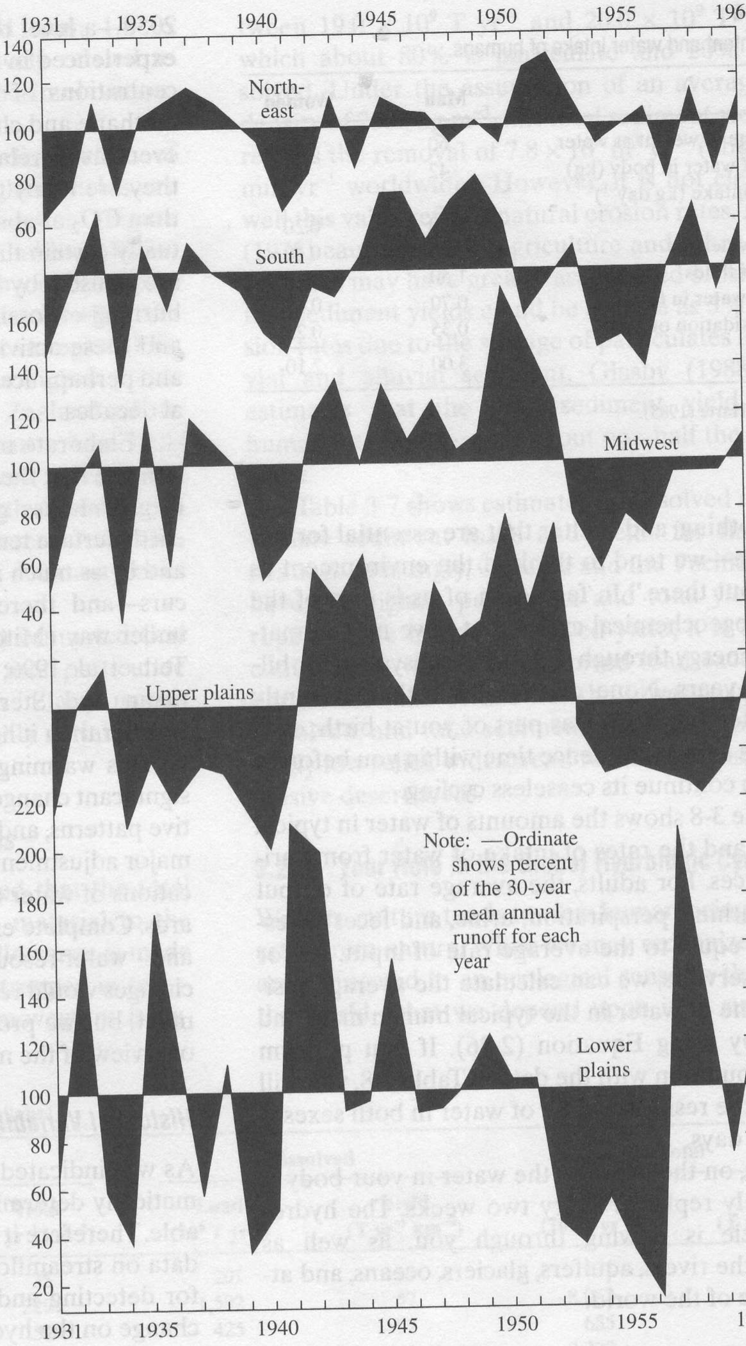

FIGURE 3-32 Standardized regional variations in streamflow for the United States for 1931–1960. From Busby (1963).

series of river discharge show considerable synchronism over the United States (Figure 3-32) and at larger scales (Figures 3-33 and 3-34), reflecting large-scale and fairly persistent climatic patterns.

Climate-related persistence is evident in the records of large rivers with long records. The longest streamflow record in the world is that of the Nile River, for which information is available from 622 to 1520 and from 1700 to the present. Riehl and Meitin (1979) found three contrasting patterns of variability in this record: (1) from 622 to about 950, periods of high flow alternated with

FIGURE 3-32
(Continued)

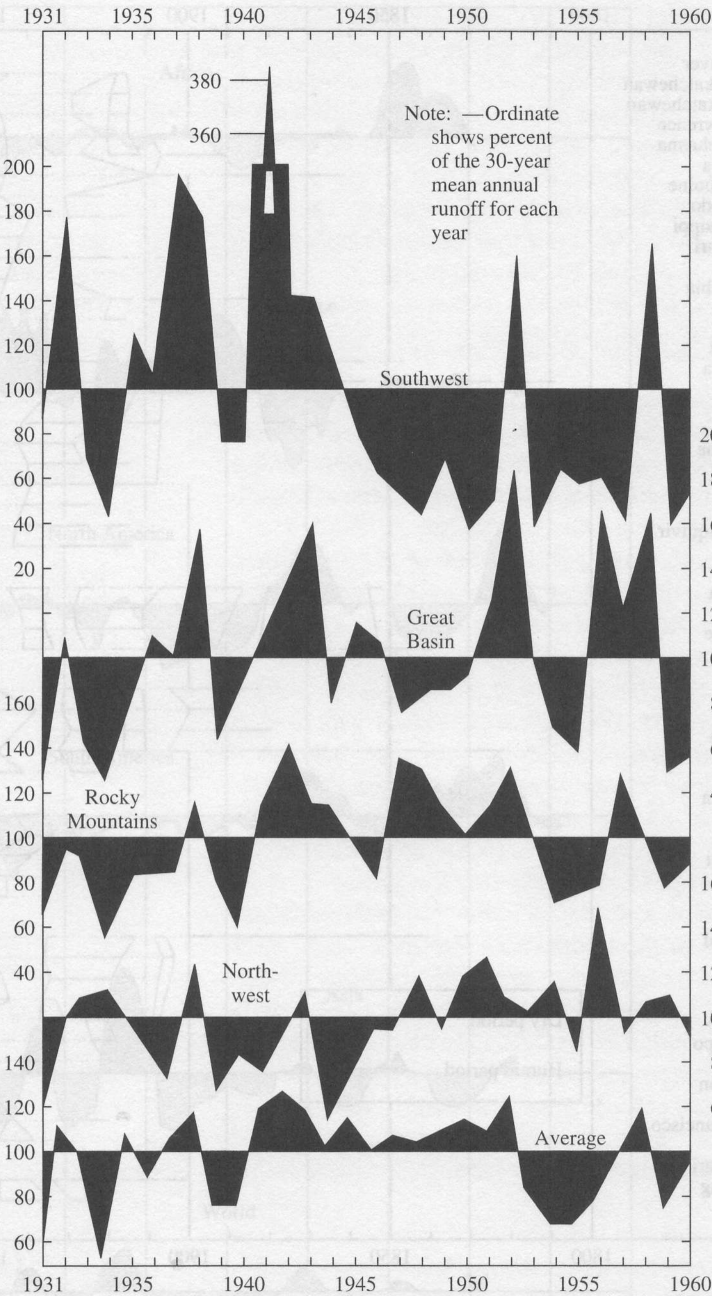

periods of low flow, with each cycle lasting 50 to 90 yr and having a moderate amplitude; (2) from 950 to 1225 there were no major trends or cycles; (3) for the remainder of the record, there were again alternating periods of high and low flow, but having cycles of from 100 to 180 yr and of much higher amplitude than in the first pattern. These very pronounced changes in the pattern of variability appear to be related to global climatic fluctuations; for example, 950–1225 corresponds to the "little climatic optimum," a period of reduced storminess. Subsequent studies have found that Nile flows are influenced by the ENSO cycle (Eltahir 1996).

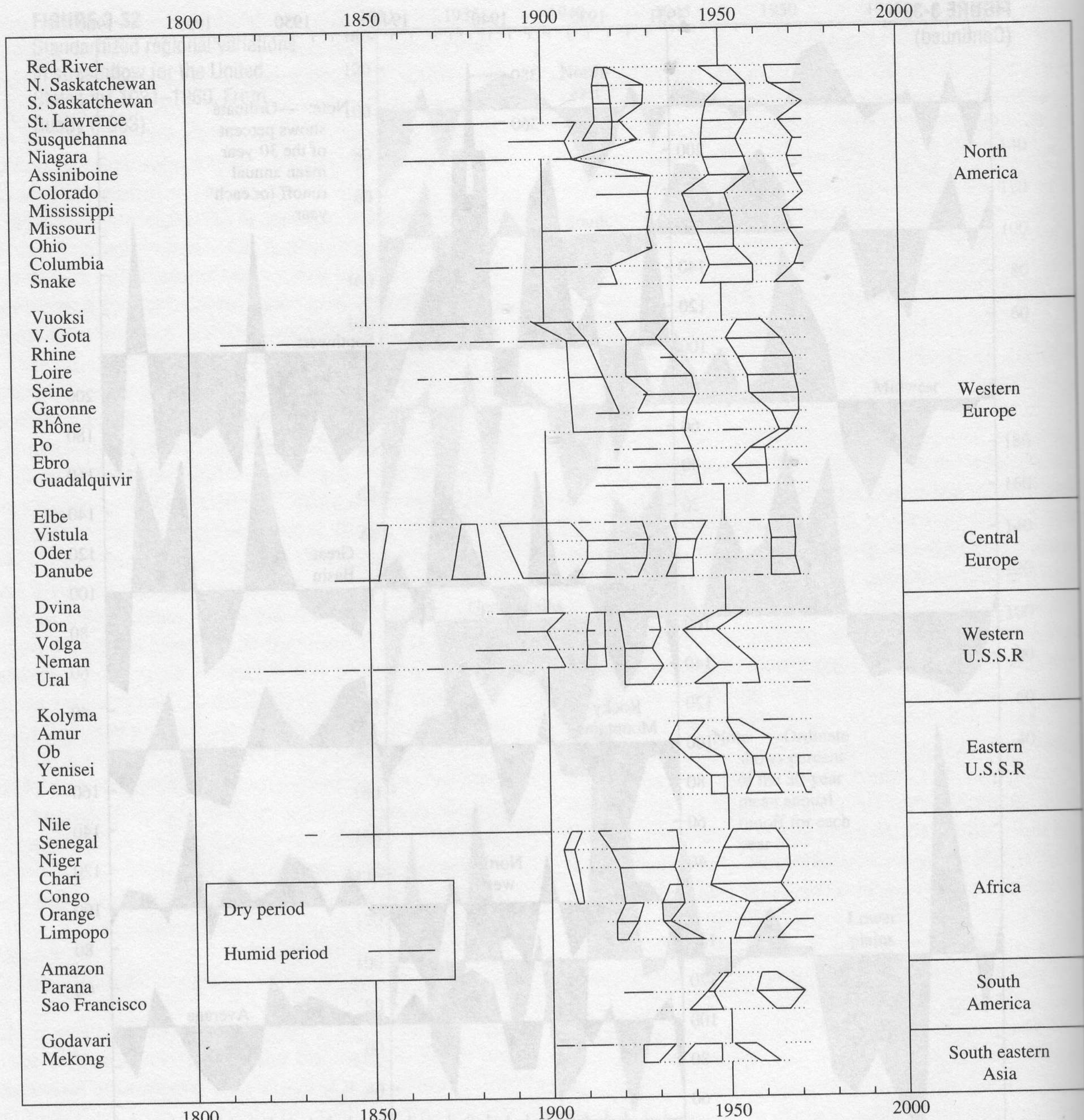

FIGURE 3-33
Wet and dry periods in historical streamflow records for 50 major rivers of the world. From Probst and Tardy (1987), used with permission.

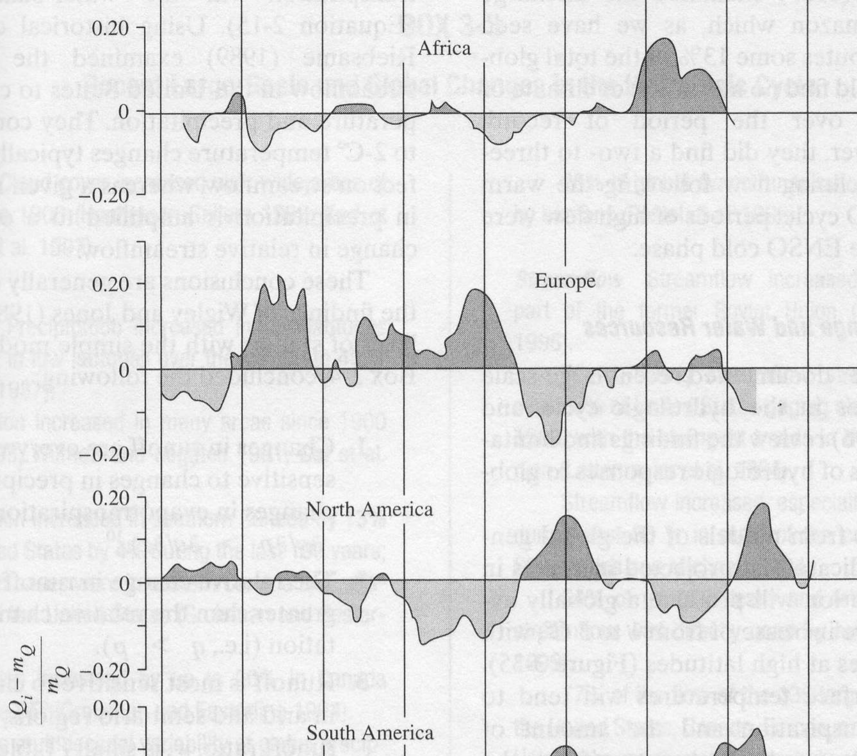

FIGURE 3-34
Standardized fluctuations in total runoff for the continents and the world. From Probst and Tardy (1987), used with permission.

Richey et al. (1989) examined the discharge record of the Amazon which, as we have seen (Table 3-4), contributes some 13% of the total global runoff. They could find no indication of climate or land-use change over the period of record, 1903–1985. However, they did find a two- to three-year period of declining flow following the warm phase of the ENSO cycle; periods of high flow were coincident with the ENSO cold phase.

Future Climate Change and Water Resources

Box 3-3 summarizes documented recent large-scale and global changes in the hydrologic cycle, and Loaiciga et al. (1996) review the findings and limitations of predictions of hydrologic responses to global warming.

Recent results from models of the global general circulation indicate that projected increases in the CO_2 concentration will produce a globally averaged temperature increase of from 1 to 5 C°, with the largest increases at high latitudes (Figure 3-35). These warmer surface temperatures will tend to increase evapotranspiration and the amount of water vapor in the atmosphere, intensifying the hydrologic cycle and increasing global precipitation by from 3% to 15% (Mitchell 1989; Loaiciga et al. 1996). The models predict generally lower precipitation at latitudes below 30° and higher precipitation in the mid-latitudes (Figure 3-36); interestingly, the patterns reported in Box 3-3 are generally consistent with those predicted by the general-circulation models. One can also infer that the higher temperatures will reduce the extent of snow cover, affecting the seasonality of streamflow at latitudes above 40° N. As is noted in Box 3-3, studies have documented recent snowpack reductions.

Experiments indicate that higher CO_2 concentrations tend to reduce water use by plants (Lemon 1983), and this could offset increases in evapotranspiration from land surfaces that are due to the temperature effect. Thus one plausible scenario is that evaporation from the oceans will increase, while land evapotranspiration will change little or perhaps even decrease. Interestingly, evaporation from measurement pans in the United States and former Soviet Union has been declining since about 1950 (Box 3-3).

Changes in long-term average runoff can be estimated from changes in precipitation and evapotranspiration via the water-balance equation (Equation 2-15). Using historical data, Karl and Riebsame (1989) examined the sensitivity of streamflow in the United States to changes in temperature and precipitation. They concluded that 1- to 2-C° temperature changes typically have little effect on streamflow, whereas a given relative change in precipitation is amplified to a one- to six-fold change in relative streamflow.

These conclusions are generally consistent with the findings of Wigley and Jones (1985), who, on the basis of studies with the simple model described in Box 3-4, concluded the following:

1. Changes in runoff are everywhere more sensitive to changes in precipitation than to changes in evapotranspiration (i.e., $\partial q/\partial p > \partial q/\partial e$).[10]
2. The relative change in runoff is always greater than the relative change in precipitation (i.e., $q > p$).
3. Runoff is most sensitive to climatic changes in arid and semi-arid regions, where the runoff ratio, w, is small (Table 3-5).
4. The relative change in runoff exceeds the relative change in evapotranspiration (i.e., $q > e$) only in regions where $w < 0.5$.

One set of results from Wigley and Jones (1985) is shown in Figure 3-37; other results can be generated by using the model in Box 3-4 (Exercise 3-13). Wigley and Jones (1985) concluded that, overall, one might expect "very large" increases in average runoff in response to the predicted warming, unless there is a compensatingly large increase in land evapotranspiration.

Box 3-5 describes another simple water-balance approach for estimating the effects of climate changes or land-use changes on the global hydrologic cycle. This model can be used to explore the effects of an increase in ocean evaporation that accompanies no change (or a decrease) in land evapotranspiration. Completion of Exercise 3-12 suggests that a given percentage increase in ocean evaporation (e.g., 6%) gives rise to a smaller relative increase in land precipitation (3.4%) and a larger relative increase in runoff (8%).

[10]Symbols are defined in Box 3-4.

BOX 3-3

Recent Large-Scale and Global Changes in the Hydrologic Cycle

Cloud cover Cloud cover increased over wide areas of the globe since 1900 (Henderson-Sellers 1992; Karl et al. 1993; Dai et al. 1997).

Precipitation Precipitation increased in mid-latitudes and decreased in low latitudes over the last 30 to 40 yr (Bradley et al. 1987).

Precipitation increased in many areas since 1900 (Karl et al. 1993; Wilmott and Legates 1991; Dai et al. 1997).

Precipitation increased in southern Canada by 13% and in the United States by 4% during the last 100 years; the greatest increases were in eastern Canada and adjacent regions of the United States (Groisman and Easterling 1994).

Precipitation increased by up to 20% in Canada north of latitude 55° (Groisman and Easterling 1994).

Decadal to multidecadal variability of global precipitation increased since 1900 (Tsonis 1996).

Proportion of precipitation occurring in extreme one-day events increased in the United States in the last 30 to 80 yr (Karl et al. 1995).

Fall precipitation increased in the central United States between 1948 and 1988 (Lettenmaier et al. 1994).

Snow Areal snow cover in the northern hemisphere declined 10% in the past 20 yr (Groisman et al. 1994).

Areal snow cover in North America declined 8% in the past 19 yr (Karl *et al.* 1993).

Glaciers Most arctic glaciers experienced a net loss of water since 1940, contributing 0.13 mm yr^{-1} to sea-level rise (Dowdeswell et al. 1998).

Evapotranspiration Pan evaporation in the United States and former Soviet Union declined since 1950 (Peterson et al. 1995).

Plant growth in northern high latitudes increased from 1981 to 1991 (Myneni et al. 1997).

26% of global evapotranspiration was directly used by humans (Postel et al. 1996).

Streamflow Streamflow increased in the European part of the former Soviet Union (Georgievsky et al. 1995).

Winter–spring streamflow strongly increased at over 50% of United States gaging stations from 1948 to 1988, with the strongest trends in the north-central region (Lettenmaier et al. 1994).

Streamflow increased, especially in fall and winter, during past 50 yr in most of the conterminous United States (Lins and Michaels 1994).

54% of geographically and temporally accessible streamflow was directly used by humans (Postel et al. 1996).

77% of the flow of the 139 largest river systems in the United States, Canada, Europe, and the former Soviet Union was moderately to strongly affected by reservoir regulation, diversion, and irrigation (Dynesius and Nilsson 1994).

Volume of water in global river systems was increased 700% due to dams (Vörösmarty et al. 1997a).

Average residence time of water in global river systems was tripled due to dams, which caused changes in flow regimes and water quality (Vörösmarty et al. 1997a).

Sediment Transport Global sediment transport to oceans doubled in the last 2500 yr (Milliman and Syvitski 1992); however, 16% of the current sediment being transported is trapped in reservoirs (Vörösmarty et al. 1997b).

Sea Level Sea level increased at a rate of 2.4 mm yr^{-1} throughout the 20th century (Peltier and Tushingham 1991).

At least 0.54 mm yr^{-1} of net sea-level rise (20 to 30% of total) was caused by human intervention in the hydrologic cycle (ground-water mining, reduction in volume of Aral and Caspian seas, desertification, deforestation, and wetland drainage, minus reservoir storage; Sahagian et al. 1994).

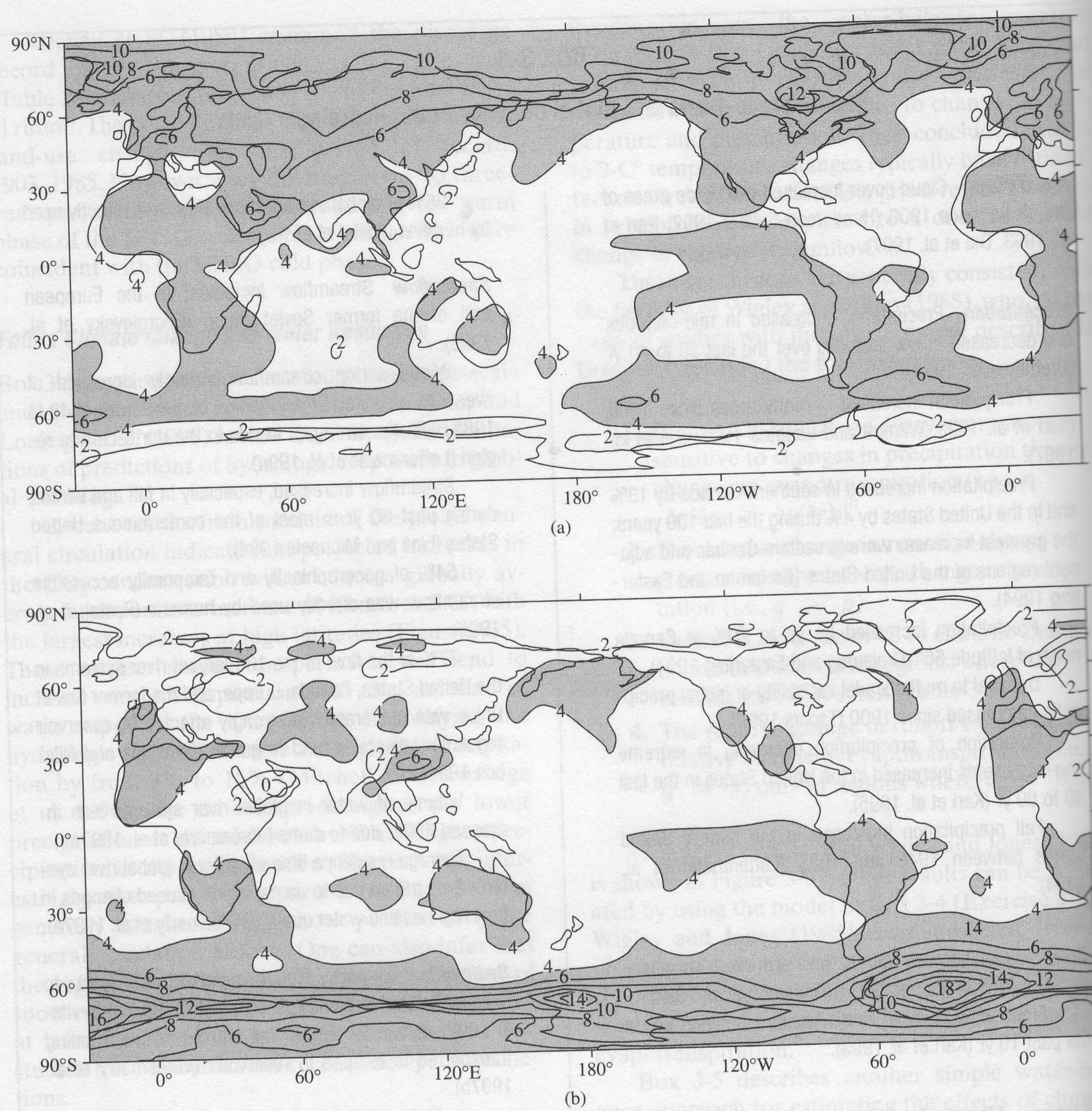

FIGURE 3-35
Global distribution of changes in surface temperature due to a doubling of CO_2 as projected by one model. (a) December–February average; (b) June–August average. Contours every 2 C°; increases > 4 C° are stippled. From Mitchell (1989), used with permission of the American Geophysical Union.

Even though the models in Boxes 3-4 and 3-5 are extremely simple, they give results that are in general agreement with those of very complex general-circulation models: the higher surface temperatures will increase global precipitation [in the range of from 3% to 11% (Wigley and Jones 1985)]; this increase will probably lead to even greater relative increases in runoff. More detailed studies in the mid-latitudes predicted that global warming will lead to shorter winters, reduced snowpacks and snowmelt runoff, larger winter floods, drier summers, and increased temporal variability. Interest-

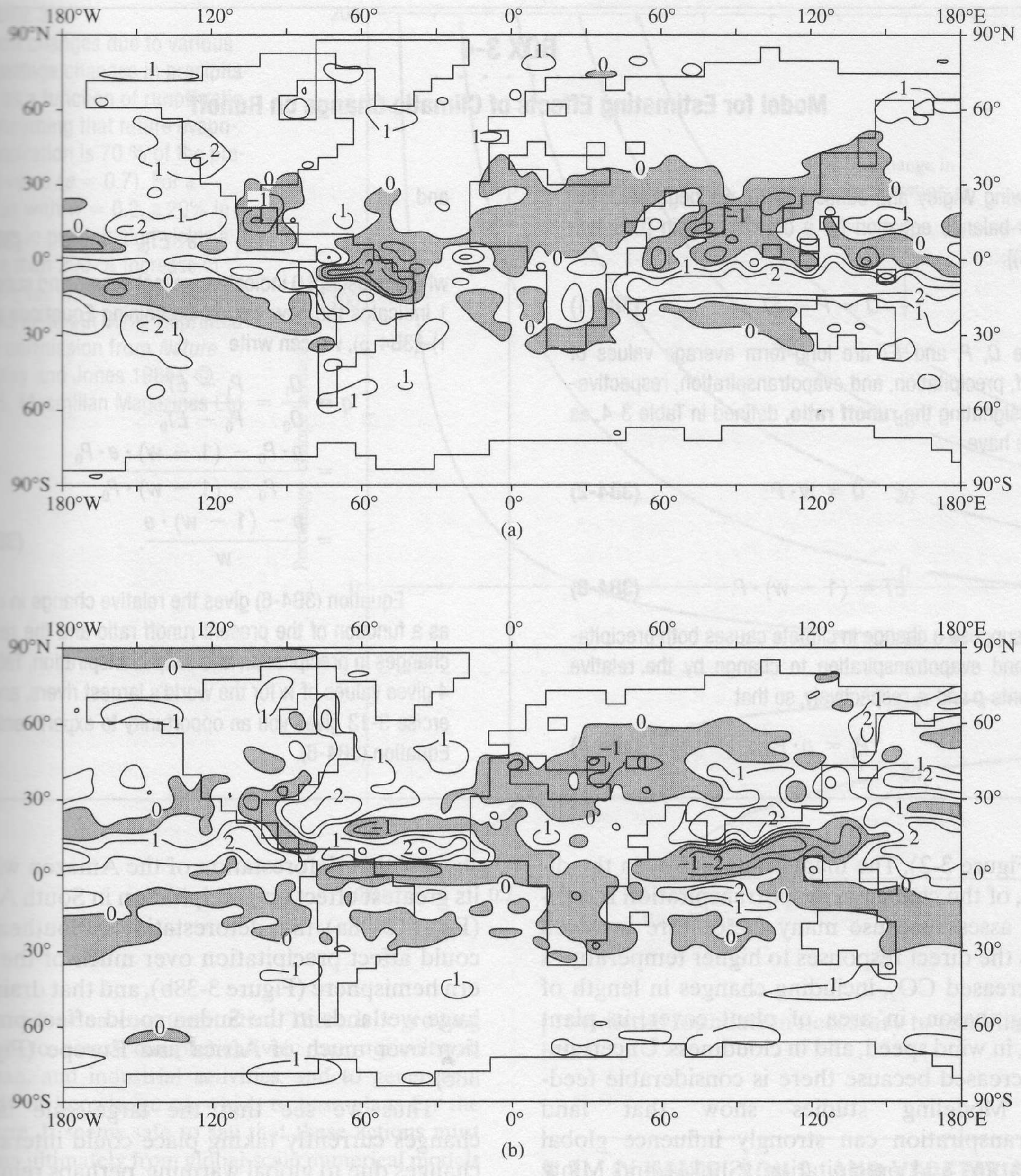

FIGURE 3-36
Global distribution of changes in precipitation due to a doubling of CO_2 as projected by one model. (a) December–February average; (b) June–August average. Contours are 0, ± 1, and ± 2 mm day^{-1}; areas of decrease are stippled. From Mitchell (1989), used with permission of the American Geophysical Union.

ingly, many observed changes, including increasing streamflow trends, are consistent, at least in direction, with model predictions (Box 3-3).

However, we must keep in mind that there is considerable uncertainty in the predictions of even the most elaborate general-circulation models, because they operate on very large grid scales (8° latitude by 10° longitude) and contain only crude representations of important hydrologic processes, especially cloud formation and evapotranspiration. The proportion of the increased atmospheric water vapor that becomes clouds, and the nature of those clouds, cannot be predicted with certainty, but they have pronounced effects on the earth's heat bal-

BOX 3-4

Model for Estimating Effects of Climatic Change on Runoff

Following Wigley and Jones (1985), we begin with the water-balance equation for a drainage basin [Equation (2-16)]:

$$Q = P - ET, \tag{3B4-1}$$

where Q, P, and ET are long-term average values of runoff, precipitation, and evapotranspiration, respectively. Designating the **runoff ratio,** defined in Table 3-4, as w, we have

$$Q = w \cdot P \tag{3B4-2}$$

and

$$ET = (1 - w) \cdot P. \tag{3B4-3}$$

Now suppose a change in climate causes both precipitation and evapotranspiration to change by the relative amounts p and e, respectively, so that

$$P_1 = p \cdot P_0 \tag{3B4-4}$$

and

$$ET_1 = e \cdot ET_0, \tag{3B4-5}$$

where subscript 0 indicates present values and subscript 1 indicates the new values. Combining Equations (3B4-1)–(3B4-5), we can write

$$\begin{aligned} q \equiv \frac{Q_1}{Q_0} &= \frac{P_1 - ET_1}{P_0 - ET_0} \\ &= \frac{p \cdot P_0 - (1 - w) \cdot e \cdot P_0}{P_0 - (1 - w) \cdot P_0} \\ &= \frac{p - (1 - w) \cdot e}{w}. \end{aligned} \tag{3B4-6}$$

Equation (3B4-6) gives the relative change in runoff as a function of the present runoff ratio and the relative changes in precipitation and evapotranspiration. Table 3-4 gives values of w for the world's largest rivers, and Exercise 3-13 gives you an opportunity to experiment with Equation (3B4-6).

ance (Figure 3-2). The magnitude, and even the direction, of the change in evapotranspiration is difficult to assess because many factors are involved besides the direct responses to higher temperatures and increased CO_2, including changes in length of growing season, in area of plant cover, in plant species, in wind speed, and in cloudiness. Uncertainty is increased because there is considerable feedback: Modeling studies show that land evapotranspiration can strongly influence global temperature and precipitation (Shukla and Mintz 1982; Loaiciga et al. 1996).

Some of the intricate complexities of the global hydrologic cycle that further confound predictions can be appreciated in the modeling studies described by Eagleson (1986). In these studies, a general-circulation model of the earth was used to "trace" the water vapor introduced into the atmosphere in a one-day pulse of evapotranspiration from selected regions (rectangles of 8° latitude by 10° longitude), to see where it fell as precipitation over the subsequent two months. The results for three cases are shown in Figure 3-38. These cases suggest that deforestation of the Amazon will have its greatest effect on precipitation in South America (Figure 3-38a), that deforestation in Southeast Asia could affect precipitation over much of the northern hemisphere (Figure 3-38b), and that drainage of huge wetlands in the Sudan could affect precipitation over much of Africa and Europe (Figure 3-38c).

Thus we see that the large-scale land-use changes currently taking place could interact with changes due to global warming, perhaps reinforcing them in some areas and weakening them in others. Clearly there is much to learn about the global hydrologic cycle and its complex feedbacks with human activities, and there are many potentially fruitful avenues of study. Eagleson's (1986) summary comments are an apt conclusion for this brief overview of our current understanding:

> Because of humanity's sheer numbers and its increasing capacity to affect large regions, the hydrologic cycle is being altered on a global scale with consequences for the human life support system

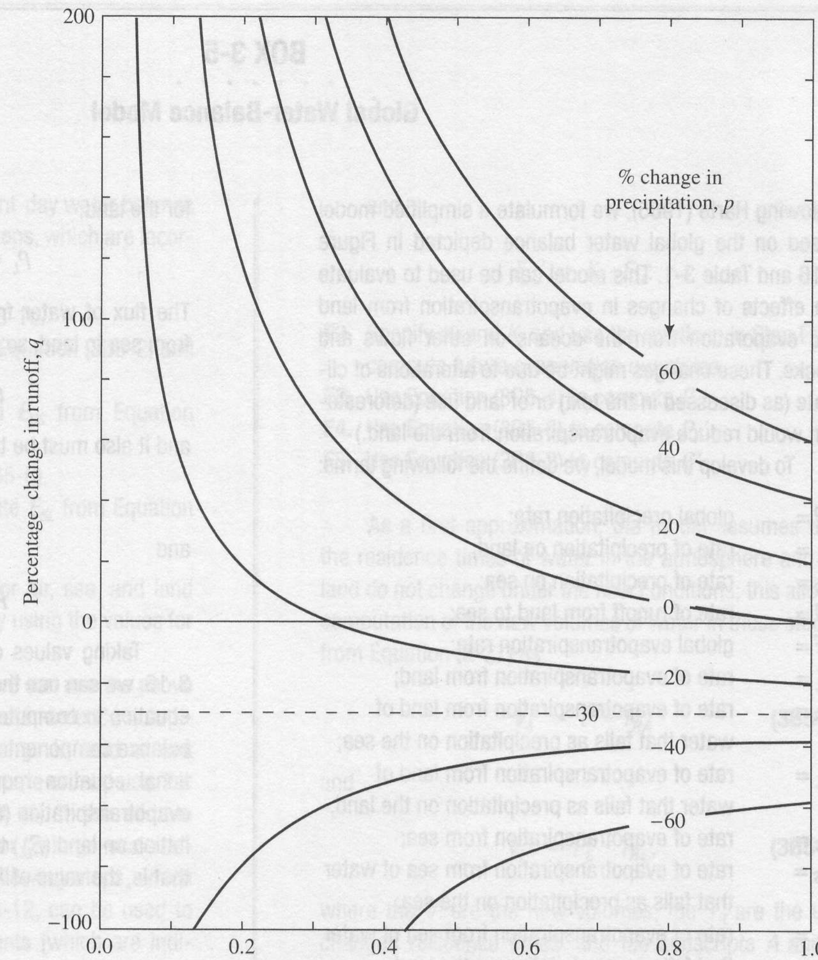

FIGURE 3-37
Runoff changes due to various percentage changes in precipitation as a function of runoff ratio, w, assuming that future evapotranspiration is 70 % of the present value ($e = 0.7$). For a region with $w = 0.2$, a 20% increase in precipitation yields a more than 200-% increase in runoff; for $w = 0.6$, the increase would be about 60%. Reprinted with permission from *Nature* (Wigley and Jones 1985), © 1985, Macmillan Magazines Ltd.

that are often counterintuitive. There is a growing need to assess comprehensively our agricultural, urban, and industrial activities, and to generate a body of knowledge on which to base plans for the future. It seems safe to say that these actions must come ultimately from global-scale numerical models of the interactive physical, chemical, and biological systems of the earth. Of central importance among these systems is the global hydrologic cycle, and its representation in these models presents many analytical and observational challenges for hydrologists.

As was noted in Section 1.3, a major challenge for hydrologists is to establish the linkage between local-scale and global-scale processes, and this relationship is the subject of much current research. The subsequent chapters of this book develop the basic aspects of the processes that control the land phase of the hydrologic cycle and provide the foundation necessary to establish those links.

3.3 CLIMATE, SOILS, AND VEGETATION

3.3.1 Climate and Soils[11]

Soils are formed by the physical and chemical breakdown of rock, and the types and rates of these processes depend largely on temperature and the availability of water. Thus climate, along with the type of geologic parent material, the actions of biota (which are largely determined by climate), the

[11]Much of the discussion in this section is based on Donahue et al. (1983).

BOX 3-5

Global Water-Balance Model

Following Harte (1985), we formulate a simplified model based on the global water balance depicted in Figure 3-16 and Table 3-1. This model can be used to evaluate the effects of changes in evapotranspiration from land and evaporation from the oceans on other flows and stocks. These changes might be due to alterations of climate (as discussed in the text) or of land use (deforestation would reduce evapotranspiration from the land.)

To develop this model, we define the following terms:

$P =$ global precipitation rate;
$P_L =$ rate of precipitation on land;
$P_S =$ rate of precipitation on sea;
$Q =$ rate of runoff from land to sea;
$E =$ global evapotranspiration rate;
$E_L =$ rate of evapotranspiration from land;
$E_{LS} =$ rate of evapotranspiration from land of water that falls as precipitation on the sea;
$E_{LL} =$ rate of evapotranspiration from land of water that falls as precipitation on the land;
$E_S =$ rate of evapotranspiration from sea;
$E_{SS} =$ rate of evapotranspiration from sea of water that falls as precipitation on the sea;
$E_{SL} =$ rate of evapotranspiration from sea of water that falls as precipitation on the land.

All the above quantities have dimensions [$L^3\ T^{-1}$] and represent long-term average flux rates.

We can write the following water-balance equations. For the sea,

$$P_S = E_{SS} + E_{SL} - Q; \qquad \textbf{(3B5-1)}$$

for the land,

$$P_L = E_{LS} + E_{LL} + Q. \qquad \textbf{(3B5-2)}$$

The flux of water from land to sea must balance that from sea to land, so

$$Q + E_{LS} = E_{SL}, \qquad \textbf{(3B5-3)}$$

and it also must be true from the above definitions that

$$P_L = E_{LL} + E_{SL} \qquad \textbf{(3B5-4)}$$

and

$$P_S = E_{LS} + E_{SS}. \qquad \textbf{(3B5-5)}$$

Taking values of P_S, P_L, and Q as given in Figure 3-16, we can use the above relations and one additional equation to compute the values of the remaining water-balance components under present conditions. The additional equation required expresses the ratio of land evapotranspiration (E_L) that subsequently falls as precipitation on land (E_{LL}) to that which falls on the sea (E_{LS})—that is, the value of k in

$$E_{LL} = k \cdot E_{LS}. \qquad \textbf{(3B5-6)}$$

The value of k is not known very precisely (but note the discussion in the text of climatic models that attempt to trace the destination of water evaporated from portions of the continents). Following Harte (1985), we will initially assume $k = 3$; Exercise 3-12 allows you to investigate the consequences of assuming other values.

effects of topography, and time, is one of the principal factors determining the nature of the soil at any location.

The classification of soils is a complex topic, one that we can explore only briefly in this text. A widely accepted taxonomic scheme defines 10 **soil orders** covering all the soils of the world; classification into these orders is based largely on the degree of development of characteristic **horizons** that result from the operation of soil-forming processes over time. A very general description of these typical horizons is given in Figure 3-39, and the major features characterizing the soils in each order are given in Table 3-9.

The influence of climate on soil type increases with the passage of time, reducing the influences of parent material and topography. Thus we would expect a reasonably strong relation between climate and soil type on a global scale. This is confirmed by Table 3-9 and by Figure 3-40, which shows the

The computations of the present-day water balance can now proceed by the following steps, which are incorporated in Exercise 3-12:

P1. Find P_L, P_S, and Q from Figure 3-16.
P2. Substitute Equation (3B5-6) in Equation (3B5-2) and solve for E_{LS}.
P3. Use this value of E_{LS} to find E_{SS} from Equation (3B5-5).
P4. Compute E_{LL} from Equation (3B5-6).
P5. Use this value of E_{LL} to compute E_{SL} from Equation (3B5-4).

The present-day residence times for air, sea, and land are computed via Equation (2-27) by using the values for the stocks given in Table 3-1.

Again following Harte (1985), we can use the above equations as a model to calculate water-balance quantities under conditions in which change in land or sea evaporation is due to changes in climate or land use. For example, we might postulate that (1) if the climate warms, both E_L and E_S will increase or (2) large-scale deforestation might reduce E_L. The following steps, which are also incorporated in Exercise 3-12, can be used to compute future values of components [which are indicated by primes (′)]:

F1. Assume future values of evaporation are related to present values as

$$E_{SS}' = K_S \cdot E_{SS},$$
$$E_{SL}' = K_S \cdot E_{SL},$$
$$E_{LS}' = K_L \cdot E_{LS},$$

and

$$E_{LL}' = K_L \cdot E_{LL}.$$

F2. Specify K_S and K_L and use the relations in Step F1 to compute future evaporation quantities.
F3. Use Equation (3B5-4) to compute P_L'.
F4. Use Equation (3B5-5) to compute P_S'.
F5. Use Equation (3B5-2) to compute Q'.

As a first approximation, the model assumes that the residence times of water in the atmosphere and on land do not change under the new conditions; this allows computation of the new volumes of water in those stocks from Equation (2-27) as

$$V_A' = P' \cdot T_{RA} \qquad \textbf{(3B5-7)}$$

and

$$V_L' = P_L' \cdot T_{RL}, \qquad \textbf{(3B5-8)}$$

where the V' are the new volumes, the T_R are the unchanged residence times, and the subscripts A and L refer to the atmosphere and land, respectively. The new volume of water in the oceans is computed under the assumption that the total volume of water on earth does not change. Note that these assumptions do not account for the melting of ice caps and glaciers or thermal expansion of water due to any temperature increase or for any other climatic feedback effects.

world-wide distribution of soil orders; this map can be compared with Figures 3-12 and 3-19.

The occurrence of Entisols and some Inceptisols is determined primarily by recent geologic history and topography rather than climate, so soils of these orders are found in many regions. Note, however, that Inceptisols are widespread in the Arctic and Subarctic, where soil-forming processes proceed only slowly. Inceptisols are also found on recent alluvial and colluvial deposits like those of the Mississippi and Amazon valleys and the Himalayas.

The development of soils of the remaining orders is determined mostly by climatic factors, particularly annual temperature, annual precipitation, and seasonal distribution of precipitation. Brief descriptions of the distributions of these soils and their relation to climate follow.

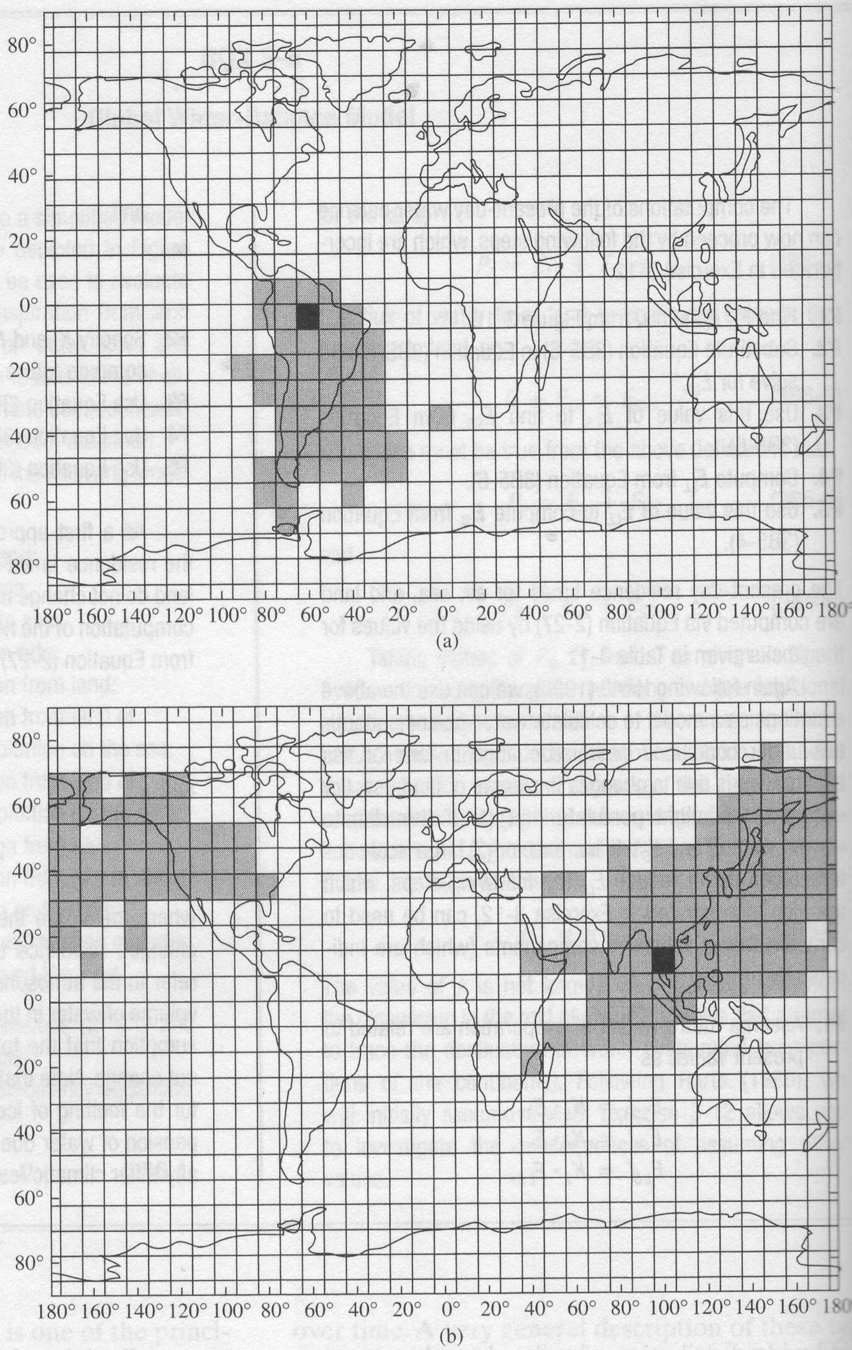

FIGURE 3-38
Shaded regions are places where water evaporated in the black rectangles during one day ultimately fell as precipitation over the following two-month period, according to a general-circulation model. (a) Amazon basin in March; (b) Southeast Asia in March; (c) Sudan in January. From Eagleson (1986), used with permission of the American Geophysical Union.

Histosols are concentrated where more than 80% of the growing season (defined as months with average temperature > 10° C) has > 40 mm of precipitation (Lottes and Ziegler 1994). The largest zones of Histosols are north of latitude 50° N (Canada, British Isles).

Aridisols occur in desert regions, which are concentrated near 30° latitude. In South America, however, the zone of Aridisols extends southward from 30° in the rain shadow of the Andes, and in Asia these soils are found near 40° in the shadow of the Himalayas.

FIGURE 3-38
(Continued)

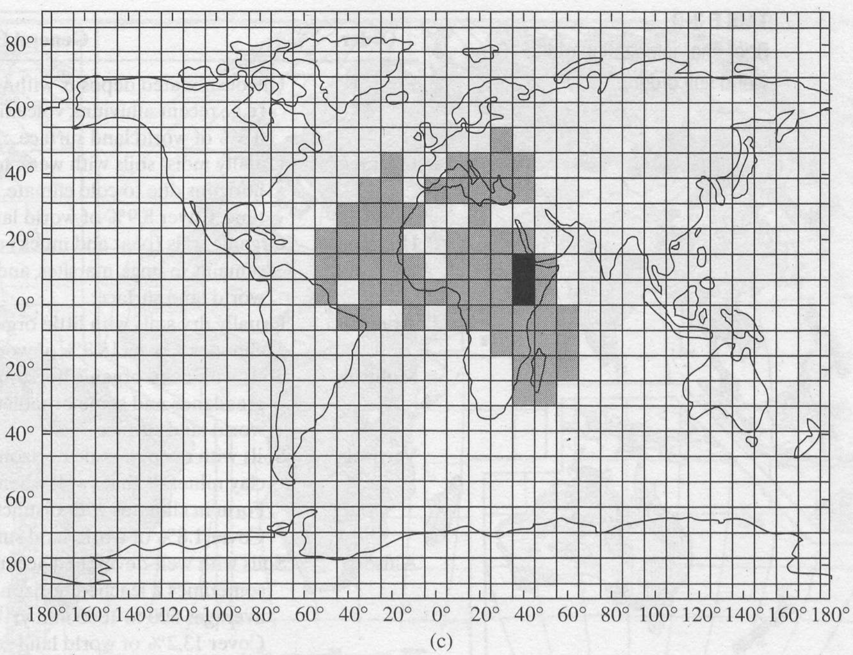

FIGURE 3-39
General features of typical horizons resulting from soil-forming processes. These horizons vary in thickness in various soils (and may be absent in some). Transition zones between horizons can often be identified. [See, for example, Donahue et al. (1983).]

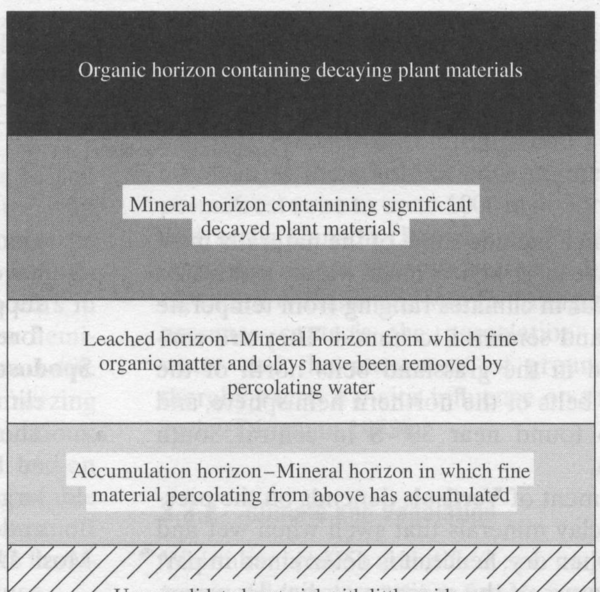

TABLE 3-9
Brief characterization of the 10 world soil orders.

Order	General Features
Entisols	Unconsolidated deposits with virtually no soil development (e.g., recent alluvium, volcanic ash, desert sands). Cover 8.3% of world land surface.
Inceptisols	Usually moist soils with weak to moderate development of horizons due to cold climate, waterlogging, and/or lack of time. Cover 8.9% of world land surface.
Histosols	Organic soils (peat and muck) consisting largely of plant remains in bogs, marshes, and swamps. Cover 0.9% of world land surface.
Aridisols	Usually dry soils with little organic matter; form in dry climates. Cover 18.8% of world land surface.
Mollisols	Soils with deep organic horizon; usually associated with grasslands and some broadleaf forests. Cover 8.6% of world land surface.
Vertisols	Soils with deep organic horizon and high concentrations of clay minerals that swell when wet and shrink when dried. Form in climates with distinct wet and dry seasons. Cover 1.8% of world land surface.
Alfisols	Soils with well-developed accumulation horizon and sometimes a leached horizon. Form where precipitation averages 500 to 1300 mm yr^{-1}, usually under forests. Cover 13.2% of world land surface.
Spodosols	Soils with well-developed organic, leached, and accumulation horizons. Usually form in cool, wet climates under forests. Cover 4.3% of world land surface.
Ultisols	Usually moist, extensively weathered soils with well-developed leached and accumulation layers. Form in humid tropical or subtropical climates under forest or savanna. Cover 5.6% of world land surface.
Oxisols	Usually moist, excessively weathered soils consisting mostly of clay minerals containing few mineral nutrients. Form in humid tropical or subtropical areas, usually under hardwood forests. Cover 8.5% of world land surface.

Largely from Donahue et al. (1983).

Mollisols, which include some of the naturally most productive and hence most widely cultivated soils, occur in climates ranging from temperate to cool and semiarid to humid. They are concentrated in the grassland belts north of the Aridisol belts of the northern hemisphere, and are also found near 30° S in central South America.

The development of **Vertisols** depends on the presence of clay minerals that swell when wet and shrink when dry; hence, it is determined in part by the nature of the parent material. However, these soils are most commonly associated with climates that experience a pronounced alternation of wet and dry seasons.

Alfisols are naturally fertile soils that occur in large regions to the north of the Mollisols in the northern hemisphere, as well as in several regions between about 35° N and S. These areas have subhumid to humid climates and typically support grassland, savanna, or hardwood forests.

Spodosols develop in well-drained sites in cool, wet climates under hardwood and conifer forests. They are widespread in the northeastern United States and southeastern Canada and in a large belt north of 60° latitude in Scandinavia and the former Soviet Union.

Most **Ultisols** are confined to within 20° of the equator, where climates are humid and subtropical or tropical and soil-forming processes are intense. There are also large areas of these soils in the southeastern United States and in southeastern China.

The extensively-weathered **Oxisols** are confined to the tropical and subtropical rain forests on ei-

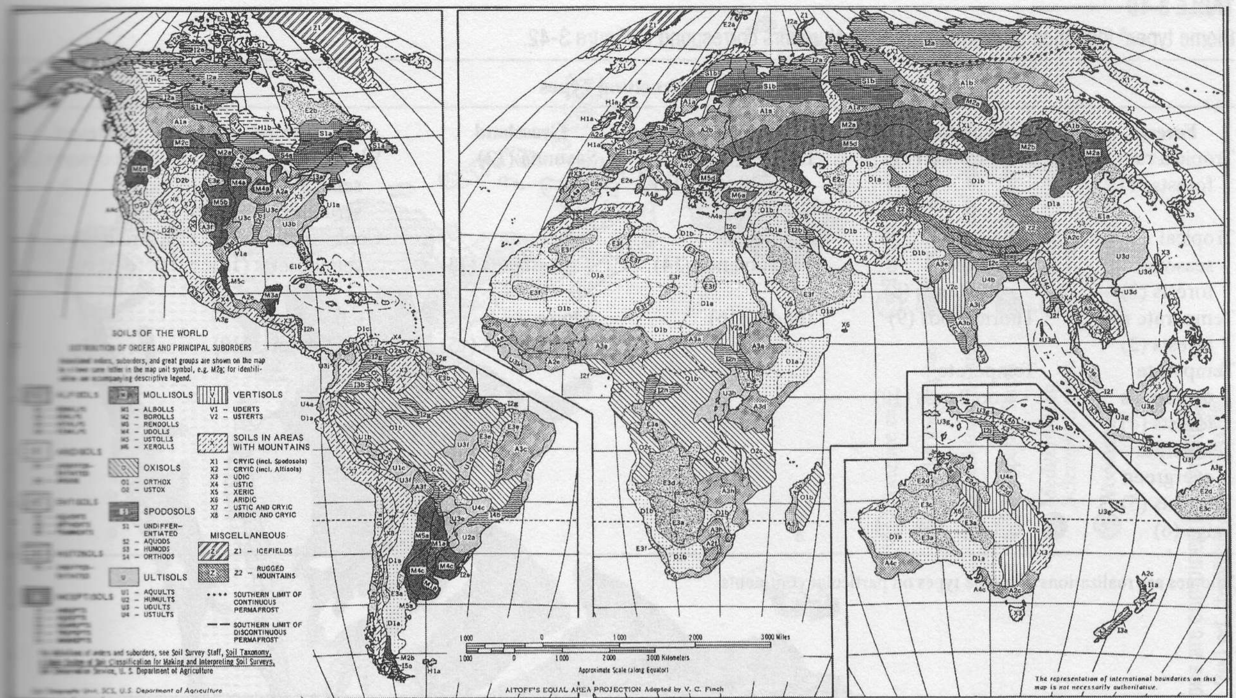

FIGURE 3-40
Global distribution of soil orders. Map prepared by U.S. Department of Agriculture.

ther side of the equator, where intense leaching has been occurring for long periods of geologic history.

The seasonal or continuous occurrence of soil temperatures below 0 °C is a climatic factor with important hydrologic implications, because water in the solid state is essentially immobile. Hydrologically significant seasonal freezing of soil occurs in many winters over much of the northern hemisphere land areas above 40° latitude (Figure 3-40). However, the depth and extent of seasonal freezing are highly dependent on local surface conditions, especially vegetative cover and snow depth, and on the severity of winter temperatures. Impermeable frozen ground can significantly accelerate runoff from rain or snowmelt, and hence exacerbate flooding (Dingman 1975).

Permafrost is the condition in which soils and/or their underlying parent materials remain at temperatures below 0 °C throughout the year, with only a thin surface layer thawing in the summer. Figure 3-40 delineates areas in which this condition is spatially continuous and those in which it is discontinuous; in the latter areas, permafrost is typically present under north-facing slopes and absent under south-facing slopes (in the northern hemisphere). Permafrost bottom depths range from 60–90 m at the southern edge of the continuous-permafrost zone to up to 1000 m in northern Alaska and arctic Canada (Brown and Péwé 1973). Permafrost is almost always a barrier to the movement of water (Williams and van Everdingen 1973), so its presence controls the percolation of infiltrated water and the movement of ground water and thereby exerts a major influence on the hydrologic cycle (Dingman 1973).

3.3.2 Climate and Vegetation

Whittaker (1975) identified six major structural types of land vegetation: forest; woodland (dominated by small trees, generally widely spaced and with well developed undergrowth); shrubland (dominated by shrubs, with total plant coverage exceeding 50% of the land area); grassland; scrubland (dominated by shrubs, with plant coverage between 10 and 50%); and desert (plant coverage below

TABLE 3-10
Biome types[a] identified by Whittaker (1975). Numbers correspond to Figure 3-42.

Structural Types					
Forest	**Woodland**	**Shrubland**	**Grassland**	**Scrubland**	**Desert**
Tropical rain forests (1)	Elfin woods (7)	Temperate shrublands (11)	Savanna (12)	Warm semidesert scrublands (17)	True deserts (20)
Tropical seasonal forests (2)	Tropical broadleaf woodlands (8)	Alpine shrublands (14)	Temperate grasslands (13)	Cool semideserts (18)	Arctic-alpine deserts (21)
Temperate rain forests (3)	Thornwoods (9)	Tundra (16)	Alpine grasslands (15)	Arctic-alpine semideserts (19)	
Temperate deciduous forests (4)	Temperate woodlands (10)				
Temperate evergreen forests (5)					
Taiga (6)					

[a]Biomes are realizations of biome types on particular continents.

10%). The occurrence of these structural types in various climatic zones produces 21 major terrestrial biological communities, called **biome-types** (Table 3-10). The global distribution of these biome-types is summarized in Figure 3-41.

Climate is the dominant control on the geographical distribution of plants (Woodward 1987), and each biome-type is associated with a particular range of mean annual temperature and mean annual precipitation (Figure 3-42). The exact mechanism by which climate affects vegetation type is the object of current research. Eagleson (1982) has developed a theory in which climate, soil, and vegetative type evolve synergistically: In drier climates, where the availability of water is limiting, the character of the vegetative cover adjusts to maximize soil moisture; in moist climates, where available radiant energy is limiting, there is an ecological pressure toward maximization of biomass productivity. Recent studies using hydrometeorologic models suggest that vegetation type may be determined by the balance between precipitation and evapotranspiration, along with thermal controls on growth (Woodward 1987). In North America, Currie and Paquin (1987) found a high correlation between the numbers of tree species and average annual evapotranspiration, and Wilf et al. (1998) documented a close relation between average leaf area and mean annual precipitation across a range of climates.

EXERCISES

Exercises marked with ** have been programmed in EXCEL on the CD that accompanies this text. Exercises marked with * can advantageously be executed on a spreadsheet, but you will have to construct your own.

***3-1.** Use the model described in Box 3-1 to explore and compare the sensitivity of planetary temperature (T_p) to changes in (a) planetary albedo (a_p) and (b) the solar flux (S). For comparisons, it is most meaningful to express sensitivity in relative terms, as the fractional change in T_p in response to a given fractional change in a_p and S.

3-2. Following the steps described in Box 3-2, derive Equation (5B2-4); then derive the expressions for T_l and T_u in terms of T_s and parameters.

****3-3.** In the model described in Box 3-2, the greenhouse effect can be modeled by increasing the fraction f of longwave radiation from the surface that is absorbed in the atmosphere. Use the EXCEL program `SURFTEMP.XLS` to explore the sensitivity of T_s to increases in f. Graph T_s as a function of f ($f < 1.00$).

3-4. For the region in which you live, obtain information from the U.S. Geological Survey, the U.S. Weather Service, or other appropriate federal or state agencies (see Appendix G for Internet information sources) to establish (a) the long-term average precipitation, runoff, and

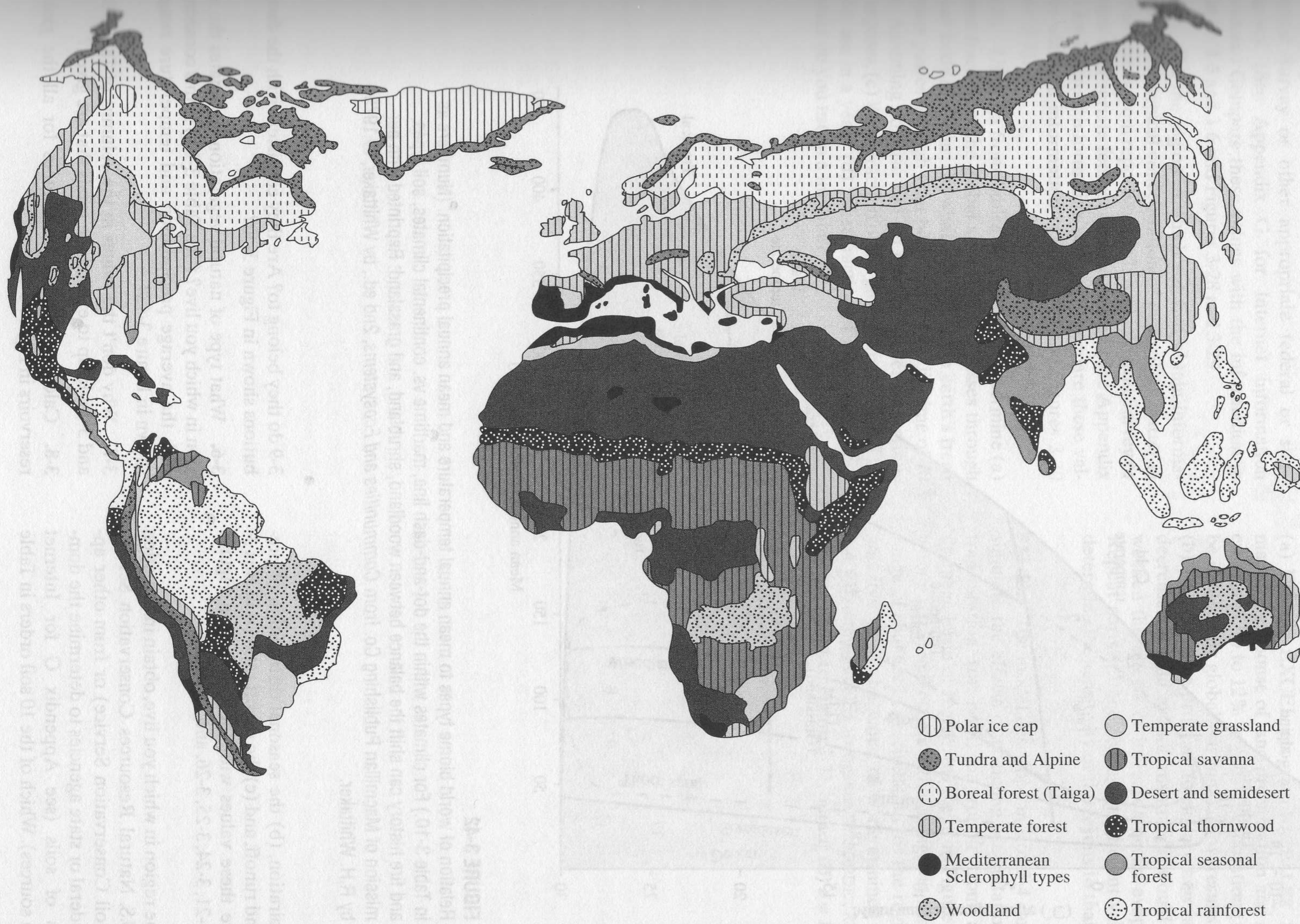

FIGURE 3-41
Global distribution of biome types identified by Whittaker (1975). (See Table 3-10; some biome types are combined for simplification.) Reprinted with permission of Macmillan Publishing Co. from *Communities and Ecosystems*, 2nd ed., by Whittaker, © 1975 by R.H. Whittaker

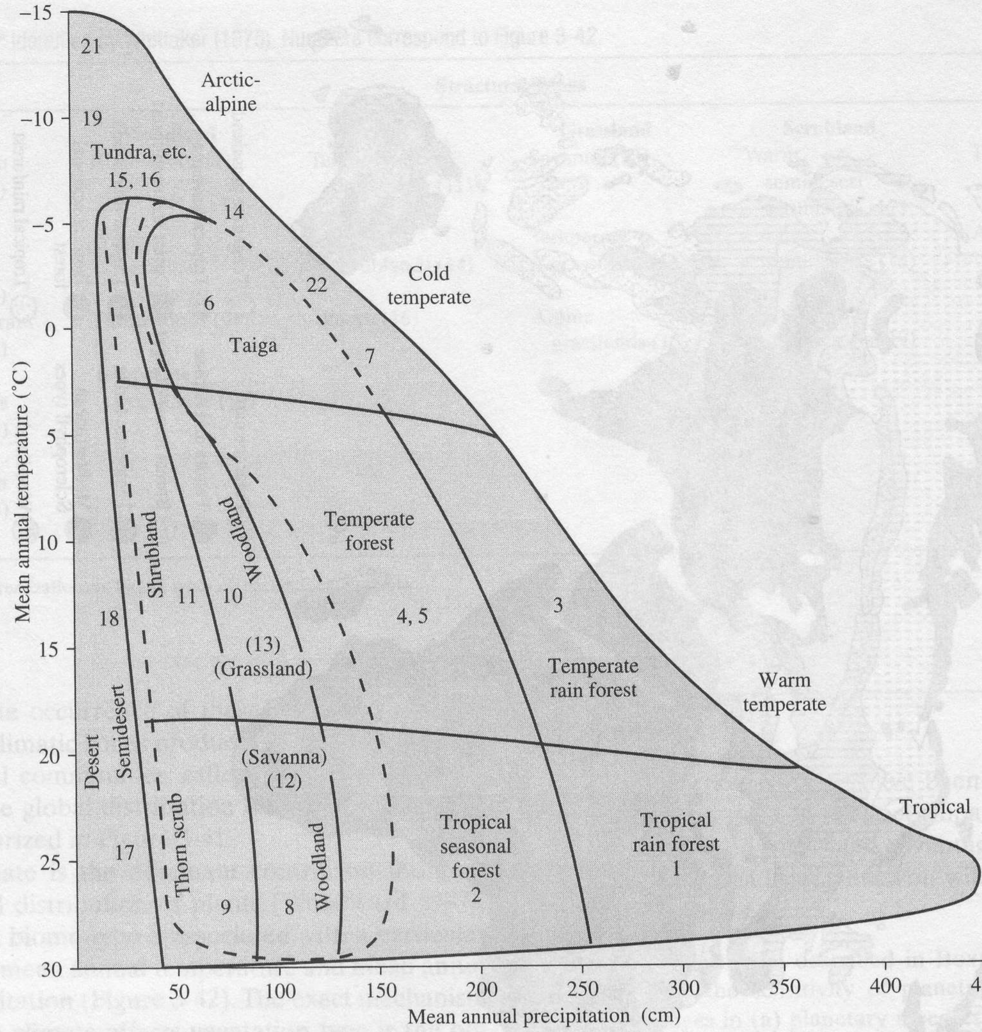

FIGURE 3-42
Relation of world biome types to mean annual temperature and mean annual precipitation. (Numbers as in Table 3-10.) For climates within the dot-and-dash line, maritime vs. continental climates, soil types, and fire history can shift the balance between woodland, shrubland, and grassland. Reprinted with permission of Macmillan Publishing Co. from *Communities and Ecosystems*, 2nd ed., by Whittaker, © 1975 by R.H. Whittaker.

evapotranspiration, (b) the seasonal distribution of precipitation and runoff, and (c) the runoff ratio (w in Box 3-4). Compare these values with those shown in Figures 3-19, 3-20, 3-21, 3-24, 3-25, 3-26, and Table 3-2.

3-5. For the region in which you live, obtain information from the U.S. Natural Resources Conservation Service (formerly Soil Conservation Service) or from other appropriate federal or state agencies to determine the dominant types of soils (see Appendix G for Internet information sources). Which of the 10 soil orders in Table 3-9 do they belong to? Are they consistent with the distributions shown in Figure 3-40?

3-6. What type of natural vegetation dominates the region in which you live? (See Table 3-10.) Is this consistent with the average precipitation and temperature ranges shown in Figure 3-42?

3-7. Why don't the values in the columns of Tables 3-1 and 3-2 add up to exactly the totals that are given?

3-8. Calculate the residence times for all the global reservoirs in Figure 3-16.

3-9. For the region in which you live, obtain information on the typical concentration and composition of dissolved solids in river waters from reports of the U.S. Geological Survey or other appropriate federal or state agency. (See Appendix G for Internet information sources.) Compare these values with the information in Tables 3-5 and 3-6 and Figures 3-28 and 3-29.

3-10. For the region in which you live, obtain information on the typical concentration of particulate matter in river waters from reports of the U.S. Geological Survey or other appropriate federal or state agency. (See Appendix G for Internet information sources.) Compare these values with the information in Table 3-7 and Figures 3-30 and 3-31.

3-11. Use data from Tables 3-1 and 3-7 to determine (a) what fraction of the global annual runoff passes through your body in a year; (b) what fraction of the earth's fresh water passes through your body in a typical lifetime of 70 yr. Assuming you use 100 gal day^{-1} of water for various purposes, (c) What fraction of the global annual runoff do you use in a year? (d) What fraction of the earth's fresh water do you use in a lifetime?

**3-12. The model described in Box 3-5 can be used to simulate the effects of changes in land evapotranspiration and/or ocean evaporation on the global water balance. (a) Use the EXCEL program WATBALEX.XLS to estimate the response of land precipitation and runoff to increases of up to 12% in ocean evaporation (which might be induced by global warming); show results on a graph. (b) Use the same program to explore how increases and decreases in land evapotranspiration would enhance or weaken the effects of increased ocean evaporation. (c) Repeat parts (a) and (b), using different values of k, to determine the sensitivity of the results to that parameter.

**3-13. The model described in Box 3-4 can be used to simulate the effects of changing precipitation or evapotranspiration (or both) on runoff from a particular drainage basin or region. (a) Refer to Figure 3-37 (which is for $e = 0.7$) and estimate the changes in runoff due to a range of changes in precipitation for the region in which you live. (Use the value of w determined in Exercise 3-4.) Use the EXCEL program DRODPDE.XLS to create graphs similar to Figure 3-37, but for (b) $e = 1$; (c) $e = 1.1$.